Author:
Jia, Simeng

Title:
GaN Distributed Bragg Reflector Cavities for Sensing Applications

University of BRISTOL

GaN Distributed Bragg Reflector Cavities for Sensing Applications

Simeng Jia

Department of Electrical and Electronic Engineering

A dissertation submitted to the University of Bristol in accordance with the requirements for award of the degree of Doctor of Philosophy in the Faculty of Engineering

March 2020

Author’s declaration

I declare that the work in this dissertation was carried out in accordance with the requirements of the University's Regulations and Code of Practice for Research Degree Programmes and that it has not been submitted for any other academic award. Except where indicated by specific reference in the text, the work is the candidate's own work. Work done in collaboration with, or with the assistance of, others, is indicated as such. Any views expressed in the dissertation are those of the author.

SIGNED: ..... DATE: .....

Abstract

The purpose of this thesis is to design Distributed Bragg Reflector cavities with integrated grating couplers connected by integrated waveguides. These structures can be used as sensors based on changes in resonance wavelengths when analytes are present in the cavity. The theory of grating couplers is introduced, and this is followed by detailed Finite Difference Time Domain modelling of the structures. Distributed Bragg Reflector cavities are then studied and the effect of using multi-mode waveguides on their performance is investigated.

This thesis studies two GaN based platforms, the first is a multi-moded GaN on sapphire platform. Based on the results of simulation optimisation, a chip is fabricated using a low-cost nanofabrication technique known as Displacement Talbot Lithography technology. This is a novel fabrication method that can perform wafer scale nanofabrication, but with the restriction that all periodic structures must have the same period and etch depth. Simulation and experimental results are compared and good agreement is shown. The structure also shows good potential for sensor applications. The second is a thinner GaN-AlN on sapphire platform. The devices are fabricated by Electron Beam Lithography technology, which allows more flexible and precise selection of structural parameters. Since a thinner gallium nitride layer is used and waveguides in this structure can realise single-mode transmission, and the results show will improve the performance of the sensor.

Acknowledgements

I cannot express enough thanks to my supervisor Professor Martin Cryan for his continued support and help on this project. He was a great inspiration to me. My completion of this project could not have been accomplished without him. I would also like to thank Professor Siyuan Yu for his guidance over my annual reviews.

The contributions of many people to the support of this project cannot be ignored. Frist of all, I would like to thank Osram for supplying the GaN-on-sapphire wafers. A special thanks to Emmanuel Le Boulbar who was from University of Bath and Geraint Gough from Cardiff University for providing chips. Furthermore, I would like to thank Philip Shields, Duncan Allsopp, Tao Wang and the rest of ManuGaN group for their support and feedback. It was a pleasure to work with them.

I thank my colleagues in the Photonics and Quantum group for being extremely supportive and helpful. Here, I would like to thank Jon Pugh in particular. I thank him for all his contributions and sacrifices during my PhD study. From the simulation guidance, equipment purchase, measurement set up to result discussion, he gave me great support. I also thanks to Neciah Dorh, Michael Wan, Martín López García, Joseph Smith, Krishna Balram, Hanyu Cen, Weiran Pang, etc. and each of them for their help in my project.

Last but not the least, I would like to thank my family who have been incredibly supportive throughout my life. My most sincere gratitude goes to my beloved grandma. Although she has passed away, her love for me has always supported me to complete the PhD project and continue on the road of my future life.

Content

List of figures

List of tables

List of abbreviations

PIC	Photonic Integrated Circuit
PhC	Photonic Crystal
GaN	Gallium Nitride
LD	Laser Diode
RIU	Silicon on Insulator
SOI	Refractive Index Unit
AC-DC	Alternating Current-Direct Current
DUV	Deep Ultraviolet
FIR	Far Infrared
LED	Light Emitting Diode
InGaN	Indium Gallium Nitride
AlGaN	Aluminium Gallium Nitride
VCSEL	Vertical Cavity Surface Emitting Laser
FDTD	Finite-Difference Time-Domain mothed
DBR	Distributed Bragg Reflector
DTL	Displacement Talbot Lithography

TE	Transverse Electric
TM	Transverse Magnetic
FSR	Free Spectral Range
FWHM	Full Width at Half Maximum
DLW	Direct Laser Writing
PML	Perfect Match Layer
SEM	Scanning Electron Microscopy
AlN	Aluminium Nitride

List of publications

Journal publications

[1] S. Jia, E. D. Le Boulbar, K. C. Balram, J. R. Pugh, T. Wang, D. W. E. Allsopp, P. A. Shields, and M. J. Cryan, "Waveguide integrated GaN distributed Bragg reflector cavity using low-cost nanolithography," Micro & Nano Letters, vol. 14, no. 13, pp. 1322-1327, 2019.

Conference contributions

[1] S. Jia, J. R. Pugh, D. W. E. Allsopp, P. A. Shields, and M. J. Cryan, "Gallium Nitride Grating Coupler Design," presented at the in SIOE: Semiconductor and Integrated OptoElectronics (SIOE) Conference 2016, 2016.

[2] S. Jia, J. R. Pugh, D. W. E. Allsopp, P. A. Shields, and M. J. Cryan, "Gallium Nitride Grating Coupler Design," presented at the PECX-XII: The 12th International Symposium on Photonic and Electromagnetic Crycal structures, 2016.

[3] S. Jia, J. R. Pugh, D. W. E. Allsopp, P. A. Shields, and M. J. Cryan, "Gallium Nitride Grating Coupler Fabrication Using Displacement Talbot Lithography," presented at the NanoMeta2017: The 6th International Topical Meeting on Nanophotonics and Metamaterials, 2016.

[4] S. Jia, E. D. Le Boulbar, K. C. Balram, J. R. Pugh, T. Wang, D. W. E. Allsopp, P. A. Shields, and M. J. Cryan, "GaN Distributed Bragg Reflector Cavity for Sensing Applications," in Frontiers in Optics / Laser Science, Washington, DC, 2018/09/16 2018: Optical Society of America, in OSA Technical Digest, p. JTu3A.86, doi: 10.1364/FIO.2018.JTu3A.86. [Online]. Available: http://www.osapublishing.org/abstract.cfm?URI=FiO-2018-JTu3A.86

1 Introduction

1.1 Background and motivation

Over the past 70 years, electronic technology has entered almost all aspects of our lives. The rapid developments of the information age have put forward new requirements for the miniaturization, efficiency and stability. However, electronic technologies have limitations in terms of signal propagation and switching speed and they can no longer meet the development needs of high-end cutting-edge technology. Therefore, it is expected that photons will be used instead of electrons to acquire, transmit, store and process information. Compared with electrons, photons have many advantages such as fast response, good interconnectivity, and high information capacity. Thus, photonic technology has become the focus of extensive research [1, 2].

In the early 1960s, the development of the laser provided a stable coherent light source for the transmission of light and information processing. This enabled signal transmission and processing possible through light. However, traditional optical circuits are composed of optical components of a certain geometric size fixed on a large optical platform or optical bench. The size of the system is on the order of a few square meters.

The beam is typically transmitted between the various optics through the air. Due to the influence of the absorption, dispersion and scattering of light on the medium, the loss of light energy of the system is large, and assembly and adjustment are also difficult. In 1969, the concept of integrated optics was first proposed by Stewart E. Miller of Bell Labs [3]. Integrated photonics is an emerging branch of optics based on optoelectronics, optical waveguide theory, laser technology and microelectronics. Inspired by microelectronic integrated circuit technology in 1972, Somekh and Yariv proposed the idea of integrating all of the optical components required on the same semiconductor substrate [4]. Since then, integrated optics has made considerable progress both in theory and practical applications. As with the development goal of the electronic age which was the "integrated circuit", the goal of the photonic era is the "photonic integrated circuit" to achieve miniaturization, and integration of optical systems.

A photonic integrated circuit (PIC) is a micro-optical system in which multiple photonic functions, such as light-emitting components, couplers, transmitters, modulators and receivers, are interconnected by optical waveguides inside or on the surface of the wafer. The integrated optical device has the advantages of small size, stable, reliable, high efficiency and low power consumption, etc. In the 1980s, the development of nanotechnology made a significant impact on the area of photonics. Nanotechnology combined with photonics to create devices with the capability of confinement, control and manipulation of light at nano scale. Such optical structures are known as photonic crystals (PhCs).

As a new type of structural material, PhCs have important research significance due to their wide application prospects. They can precisely control and manipulate the behaviour of electromagnetic waves and this results in PhCs being widely studied in the field of communications. In addition, their good reflectance and transmittance and

high sensitivity also provided new detection principles and means for chemical and biological sensors [5].

This thesis aims to investigate a PhC based PIC which could be used as a sensor. It will use the interesting and novel material of gallium nitride (GaN) on sapphire. It can be used to identify and measure the chemical composition of analytes, which is beneficial in the chemical and biosensing fields. The unique properties of GaN also provide impetus for further research on PICs.

1.2 Photonic crystals introduction

1.2.1 Origin and progress

More than half a century ago, physicists knew that electrons in crystals, such as semiconductors, are scattered by the periodic potential of the crystal lattice, and some bands formed energy gaps due to destructive interference. The dispersion relation of electrons is distributed in a band shape, which is the well-known electronic band structure [6-8]. However, it was not until 1987 that Eli Yablonovitch and Sajeev John pointed out in their respective papers that similar phenomena exist for photons. When Eli Yablonovitch studied the suppression of spontaneous emission in solid state physics and electronics, it was proposed that the propagation of light at certain frequencies in a periodic structure was strictly prohibited in a band gap [9]. Almost at the same time, Sajeev John's paper discussed the locality of photons in certain disordered superlattices. He pointed out that introducing certain defects into the regularly arranged superlattice, photons might be confined to defects and could not propagate in other directions [10].

Therefore, the concept of PhC was proposed and the photonic band gap and photon localization are important features of PhCs.

PhCs are the structural material formed by periodically arranging two or more materials having different refractive indices. When an electromagnetic wave propagates in the structure, it follows the principles of refraction, reflection and transmission. The periodic Bragg scattering of photons modulates the electromagnetic wave and forms an energy band structure similar to that of electrons [11, 12]. An electromagnetic wave in the pass band propagates almost without loss and electromagnetic waves whose frequency falls in the forbidden band is strictly prohibited from propagating, and its reflectivity can reach 100%. The disallowed bands of frequency are called photonic band gaps.

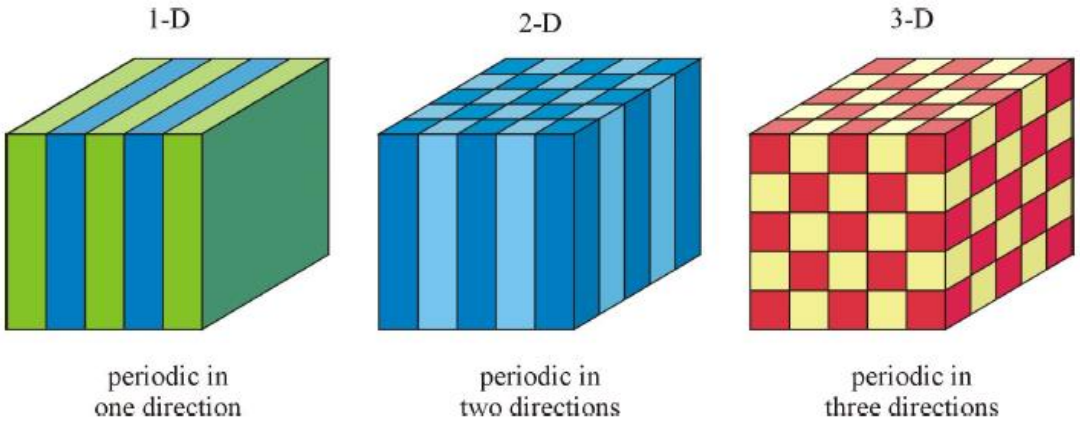

Figure 1.1 One-, two- and three-dimensional PhCs. The materials with different dielectric constants are shown in different colours. [11]

As shown in Figure 1.1, PhCs can be defined as one-dimensional, two-dimensional and three-dimensional PhCs according to the distribution of dielectric constants. One-dimensional PhCs, also known as multilayer structures, are composed of periodic alternating stacks of two materials whose refractive indices differ only in one orthogonal direction but uniform in the other two orthogonal directions [5]. In fact,

Lord Rayleigh conducted experiments on this structure as early as 1887, and it was found that this structure had a relatively high reflectivity to waves within a certain wavelength range. Since then it has been extensively studied and applied [13-19], such as Fabry-Perot multilayer structures [20-22]. Two-dimensional PhCs are periodic permittivity arrays in two-dimensional space. The typical two-dimensional PhCs structures are composed of some circular or square dielectric rods arranged in the air into such as triangular lattices, tetragonal lattices or hexagonal lattices [23-27], or by air holes arranged regularly in the medium [28-31]. Three-dimensional PhCs are periodic in the *x*-*y*-*z* plane. When light of a specific frequency enters a PhC, it is forbidden to travel in all directions, that is, they have frequency cut-off bands in all three directions, so it is called a complete photonic bandgap [32-35].

1.2.2 Applications

PhCs already exist in nature [36]. Opal, a gem abundant in Australia, is a mineral formed by deposition of silica nano-spheres as shown in Figure 1.2 (a). Its colourful appearance has nothing to do with pigment, but is due to its periodicity in its geometric structure, which makes it have photonic band structure [37]. In a similar fashion, the multicolour of certain butterfly wings is actually the result of selective reflection of sunlight from the submicron structures on their wing scales [38, 39] as shown in Figure 1.2 (b).

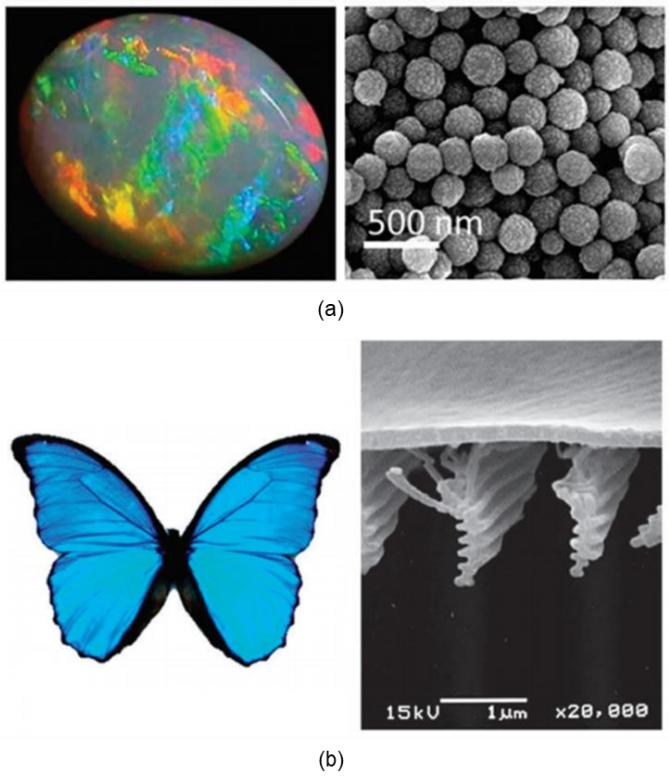

Figure 1.2 Natural PhCs: (a) Natural opal gemstone and SEM image of the silica sphere structure within; (b) the blue iridescence and SEM image of the 1D structure of the Morpho butterfly. [37]

In 1991, E. Yablonovitch and his team first successfully produced three-dimensional PhCs by drilling a series of holes the transparent material layer to create a face-cantered-cubic structure [40]. After that, a lot of achievements have been made in PhCs experiments and theoretical studies.

PhC related devices have been widely used in optical fields, such as PhC waveguides. Conventional dielectric waveguides rely on total internal reflection to support light propagation, but there will be energy loss at corners. By introducing a line defect into a two-dimensional PhC, it can be made into an optical waveguide. Wavelengths of light in the band gaps cannot enter the surrounding PhC space, but can only propagate along the line defect direction. Therefore, the PhC waveguide has high efficiency not only for the straight path but also for the bends [41]. In terms of optical fibre, PhC fibres have

been successfully commercialised [42-44]. The light propagates in the hollow enclosed by the periodic stomatal structure, which is guided by band gap effect rather than total internal reflection. It has excellent performance in low loss, and single mode guiding in large wavelength ranges [45, 46].

In addition, the more attractive application of PhCs lies in their control of atomic spontaneous emission. By introducing defects into PhCs, defect cavity with high quality factor can be realised which can control the emission from an emitter with the cavity. PhC laser diodes (LDs) [47] and low threshold lasers [29, 48] are proposed based on this theory. Due to the unique properties of PhCs, more PhC devices have been fabricated in many systems with different materials, such as optical switches [49, 50], and mirrors [51]. Moreover, PhC technologies also benefit the area of chemical and biological sensing which identify and measure the chemical constituents of an analyte [52].

1.3 Biosensors

Biosensors are devices that are sensitive to biological elements and convert their concentrations into readable signals for detection [53, 54]. In recent years, the research and application of biosensors have gone far beyond the scope of chemistry [53] and penetrated into the fields of clinical medicine [53, 55, 56], biological science [53], military science [57], food detection [58], drug analysis [59] and environmental monitoring [60]. Depending on the detection mechanism, biosensors can be classified into five types: electrochemical, electrical, optical, thermal and piezoelectric systems. Electrochemical sensors usually use methods of amperometry and potentiometry; Electrical sensors detect conductivity; while the optical sensors determine analytes by

testing luminescence, fluorescence or change of refractive index; Calorimetry is commonly used by thermal sensors and piezoelectric sensors detect based on mass [61]. Among them, the optical biosensor is widely used because of its anti-electromagnetic interference ability and high signal generation and reading speed [62]. In recent years, it has gained enormous attention because of the development of optical fibres and PhCs field.

Optical biosensors can be divided into two categories according to whether to use labels. One is the labelled biosensors. In the detection process of this type of sensors, except for a very few analytes with autofluorescence, most fluorescence-based sensors need to be labelled. It uses fluorescent dyes, radioisotope or enzyme to mark analytes and detect the signal of the marker and obtain information of the analyte. Because these labelled methods display high sensitivity and can realise the detection of single molecule [63], most of the current immunosensors belong to this category. However, labelling a biomolecule is likely to change its intrinsic properties and the preparation process is time-consuming and high cost [64]. The other is the label-free biosensors. These sensors do not require marking of analytes, but usually directly detect base on intrinsic physical properties of targets to provide information. Compared to many labelled sensors with toxic and destructive markers, label-free methods greatly simplify the operation process with inexpensive equipment [64]. Moreover, this type of sensors is suitable to be integrated into the chip and monitor the concentration of the target analyte in real time. Therefore, label-free biosensors have become an important research direction in many fields such as chemistry, pharmacy and biology.

Currently, index of refraction is the most used method of label-free optical biosensors. It uses reflected or scattered light to achieve direct and real-time detection. The target's refractive index is normally greater than that of water and the electromagnetic field passes through it slower. The sensor works by measuring this change in light speed [65].

There are many label-free sensor platforms based on direct detection of refractive index changes. Table 1.1 introduces some types of optical sensor. nm/refractive index unit (RIU) is the most common unit of optical sensor definition sensitivity. It represents the ratio of the measured wavelength change to the ambient refractive index change.

Operating principle	**Sensor structure**	**Analytes**	**Performance**	**Ref**
Surface plasmon resonance	Silica tapered optical fibre	Aqueous solutions	1600-2000 nm/RIU	[66]
	Based on the gold-coated hollow fibre	Organic chemical analytes	5653 nm/RIU	[67]
Interferometer	Fibre Mach-Zehnder interferometer	Dimethyl sulfoxide solutions	171 nm/RIU	[68]
	Sandwiched taper Mach-Zehnder interferometer	Glycerine solution	286 nm/RIU	[69]
Ring resonator	A silicon-on-insulator (SOI) slot-waveguide ring resonator	NaCl solution	298 nm/RIU	[70]
	A Si_3N_4 on SiO_2 slot-waveguide ring resonator	Bovine serum albumin	212 nm/RIU	[71]
PhC	Multi-slot PhC cavity in silicon	NaCl solution	586 nm/RIU	[72]
	A suspended slotted 1D PhC cavity based on SOI	NaCl solution	656 nm/RIU	[73]
	A cavity type InGaAsP PhC slot nanobeam slow light waveguide	sugar/water solution	900 nm/RIU	[74]

Table 1.1 Examples of optical label-free biosensors.

The various sensors mentioned above can be summarised as surface plasmon resonance, interferometers, ring resonators, and PhCs, etc according to their different structures [75]. Each sensor structure has its own advantages and the appropriate structure can be selected according to the application situation. Currently, the most mature label free biosensors are based on surface plasmon resonance. It has been widely used in the detection of protein [76, 77] and DNA molecules [78], and can even provide cancer biomarkers detection [79]. It has high sensitivity, but it also has problems such as difficulty in fabrication and high sensitivity to noise signals [5, 80]. Interference-based biosensors were the simplest structures in early biosensor manufacturing and have been widely used in medical diagnostic applications. The Mach-Zehnder interferometer based on Si_3N_4 was proposed, which can be used for rapid multiplex detection of microRNA in human urine samples [81]. However, the sensing area of such sensors is almost always in the order of square millimetre, and the sensitivity of such sensors is usually insufficient [82]. Ring oscillation can limit the light to a small area and enhance the interaction between target and light, which can be applied to a variety of biomolecular sensing. A cascaded double-microring resonator is proposed to be combined with a microfluidic channel, which can detect the binding capacity of the antibody [83]. PhC based sensors are a new type of label-free biosensor platform, which has been extensively studied in theory and experiment. Currently, it has been proven to detect the changes of concentrations of calcium cation [84], sensitive to protein binding and measure protein diameter [85]. The ultimate goal of optical biosensors is to integrate light sources, sensor area and detectors into the same chip. Although the number of miniaturised sensors is growing, the light source and detector parts are still large [75]. The sensor based on the PhC platform has excellent sensitivity and can easily integrate microcavities and waveguides with new materials into a single chip. Thus, it shows great potential in realising micro-size biosensors [82].

1.4 Gallium nitride

GaN, as a direct bandgap semiconductor material, has gained enormous attention in electronic device markets [86-90]. Although silicon technology is very mature and it is cheaper to manufacture than GaN, the 3.4 eV wide band gap of the GaN is significantly higher than the 1.2 eV band gap of silicon. A wider band gap means a higher temperature threshold. The wide band gap also allows GaN to survive higher voltage and has faster current flow through the device. These characteristics make GaN inherently more efficient than silicon [91], which can reduce system size and material cost [92]. Currently, the world's first smallest high speed charger [93] and AC-DC power supply [94] using GaN instead of silicon have been successfully commercialised. Compared with gallium arsenide transistors, GaN transistors can be adapted to higher operating temperatures and voltages, which is gradually gained acceptance for power amplifier in the industry of radio frequency [95, 96], microwave [97], and even for terahertz devices [98].

GaN is optically transparent over most of the visible spectrum, down to deep ultraviolet (DUV) and up to far infrared (FIR) wavelengths (~400 nm to ~13.6 μm). Furthermore, it has a relatively high index of refraction which is approximately 2.4. Based on these unique properties, GaN has been an ideal short wavelength light-emitting device (LED) and LD materials [99-101]. Since the fabrication of GaN blue LED with P-N junction in 1991 [102], high-brightness InGaN/AlGaN double-heterostructure LEDs [103] and InGaN single-quantum-well LED [104] have been successively commoditised. This has filled the gap of blue LED in the market for many years and also promoted the production of white LED in the general lighting market [105]. In 1995, the first InGaN-based blue-violet LD (410 nm wavelength) was introduced [106]. After that, GaN-

based Broadband blue superluminescent LEDs with a smooth continuous output spectrum and Vertical Cavity Surface Emitting Lasers (VCSELs) have also been published [107, 108]. These open up more possibilities in the application market of GaN. In addition to solid-state lighting, laser printer, blu-ray disc reading [109] to pico projector and fibre optic gyroscope [110].

In integrated design, the optical waveguide structure is the most basic and important transmission channel. In the field of traditional laser communication, the research mainly focuses on the communication wavelength range of 1550 nm, 1330 nm and 850 nm. Therefore, materials suitable for communication wavelength, such as SiO_2, Si and $LiNbO_3$, have been widely studied in optical communication. In recent years, with the rapid development of visible light wireless communication, GaN material-based visible light communication devices have been greatly promoted, such as the GaN material-based LED, visible light laser, etc. SOI is a mature technology for waveguide propagation [111-113], but conventional Si materials have a strong absorption of visible light. SiO_2 materials also have a small refractive index and light confinement is not ideal. GaN materials not only meet the non-absorption conditions, but also have a large refractive index. Thus, GaN platforms have great potential for design of visible waveguides and PIC [114-117]. Currently, many examples of GaN-based waveguide studies have achieved low-loss waveguides [118-122]. In the visible band, the GaN waveguide structure proposed by Hong Chen et al. has lower waveguide coupling loss. They fabricated the waveguide using GaN material on sapphire, which measured ~2 dB/cm for high performance waveguides at wavelengths less than 700 nm [119]. For the 1550 nm wavelength, Takuji Sekiya et al. designed a freestanding GaN waveguide on Si structure and obtained a waveguide loss of 2.2 dB/mm [122]. Moreover, the studies of GaN PhC cavity with high Q factor make it a candidate for biological or chemical sensors [123, 124]. An optimised 2D GaN on Si L3 PhC cavity achieved a Q

factor of 44000 in measurement and a Q factor of 80000 in theory [125]. Although there have been many studies on the waveguide propagation of silicon nitride in the visible wavelengths [126, 127] and it is a promising material of biosensor platform [128, 129], GaN offers the possibility of integrating light sources, sensors and detectors onto a single chip [130, 131] for a real handheld device in the future.

1.5 Summary and outline of thesis

This chapter briefly introduces the concepts of PIC and PhC. PhCs can be widely used in the field of optics by taking advantage of their characteristics. Chemical and biosensor platforms are one of applications. PhC-based label-free sensors have ultra-compact size and excellent sensitivity. Finally, the research results of GaN materials in PIC are introduced. Biosensors based on the GaN platform provide feasibility for integrating handheld sensor devices.

One structural form of a one-dimensional PhC is a linear grating. Chapter 2 will give a detailed introduction to waveguides, grating couplers and Fabry-Perot cavities. This provides a theoretical basis for proposing a sensor in the form of a grating coupler that integrates a resonant cavity in the centre of the waveguide.

Chapter 3 will introduce the methods needed to design and optimise a sensor. Firstly, an introduction of simulation software based on Finite-Difference Time-Domain (FDTD) method is given. Then the theoretical results will be compared with the simulation results using some simple GaN-based structure examples. This is followed by an introduction to the measurement set up. Finally, a brief introduction to the two

methods of fabrication is given. The University of Bath and Cardiff University carried out the fabrication using the designs supplied by us.

The target sensor can be divided into two parts: grating couplers and a Fabry-Perot cavity. Chapter 4 will focus on the design of the grating coupler. We use simulation software to optimise the coupling efficiency of the GaN-based grating structure and obtain in-out transmittance results. Then the in-out coupling measurement of the samples will be described and the measurement results of the coupling efficiency and waveguide loss will be obtained.

Chapter 5 will design the resonant cavity. We analysed the simulation results through the band diagrams and electric field distributions, and then tested the coupling power of the grating coupler with an integrated optical cavity.

Chapter 6 will present a new GaN-based platform design based on the simulation and experimental results of the previous two chapters. We show the results of grating coupler optimization and chips based on this new platform. The experimental part will be carried out in the future.

Chapter 7 will give conclusions and will introduce future work.

1.6 Contributions

The main contributions of the project are as follows:

1. Completed the parameters design of grating coupler and Fabry-Perot cavity based on 1.5-um thick GaN platform. For the coupler part, based on the basic theory of

grating couplers and one-dimensional FDTD method modelling, the parameters of GaN grating coupler were designed and optimised to achieve maximum coupling at 15 ° incident angle and 400 nm grating period by changing the fill factor and etch depth. For the cavity part, a waveguide integrated Fabry-Perot cavity structure is designed and analysed by 1D FDTD simulation. Here, the selection of 15° incident angle is based on the angle limitation of input and output fibre in the initial measurement set up, and the selection of 400nm grating period is based on the available DTL masks.

2. Completed the measurement and obtained the good results. GaN Distributed Bragg Reflectors (DBR) cavities with grating couplers are fabricated using Displacement Talbot Lithography (DTL). A good consistency was obtained between the modelling and measurement for the coupling results and Q factors of >200 have been measured. These result which show the potential for DTL fabrication to low-cost commercial sensor applications.
3. Completed the parameters design of a thinner GaN-AlN on sapphire platform. Through simulation optimisation, the single mode waveguiding was obtained, which provides the possibility for improved cavity design in the future.

2 Integrated waveguide and 1D photonic crystals

2.1 Introduction

This chapter provides an overview of some 1D PhC structures. These concepts provide the theoretical basis for the simulation and experimental results in the following chapters.

In this chapter, a design concept of sensor structure is proposed. Detailed theoretical concepts are provided for each part of the sensor, including grating couplers, Bragg gratings and Fabry-Perot cavity. In addition, the concept of 1D photon band diagram is introduced.

The theory of grating coupling can be used to study the parameter setting of single mode grating coupling efficiency, which will be used for reference in the design of the grating couplers in subsequent chapters.

The study of Bragg grating and Fabry-Perot cavity provide the possibility of adding resonance sensor in waveguide. The band structure shows the frequency range of bandgap, which is more helpful to the design of resonator.

Finally, this chapter also introduces some current research results of GaN as the PhC platform structure, which provides the possibility for the realisation of GaN sensor in the following chapters.

2.2 Waveguide coupler

Photonic integrated chips are widely used in many significant fields such as high-capacity communication, optical signal processing and avionics due to their advantages of large bandwidth, high stability and low cost. Waveguide couplers play an important role in PICs, they are used to couple optical signals in and out of photonic circuit. The coupling efficiency and bandwidth will directly determine the performance of photonic integrated chips.

Low loss GaN waveguides will be the most critical step in integrating GaN photonic chips. The relatively mature techniques to improve the fibre to waveguide coupling efficiency by reducing mode field mismatch can be classified into four types: butt coupling, end-fire coupling, prism coupling and grating coupling [132, 133]. Figure 2.1 shows the schematic diagram of the four principle methods. A butt coupler couples the beam directly onto the waveguide cross section. End-fire coupling is similar to butt coupling except that a lens is added between the fibre and the waveguide to focus light into the waveguide. Based on the working principle of these two methods, all the guided modes can be excited. These two techniques can be classified as transverse coupling.

However, these two methods require the diameter of the left optical fibre to perfect match the thickness of the waveguide on the right to achieve the best coupling. The actual coupling efficiency is only about 60% [134, 135]. Furthermore, when the waveguide is embedded in the integrated optical circuit, the realisation of transverse coupling becomes extremely difficult. Prismatic coupling and grating coupling are two vertical coupling techniques. They can achieve coupling by focusing light onto the waveguide surface at a specific angle and the modes that meet the conditions of phase matching are coupled. Zhaolin Lu et al. proposed prism couplers provide great flexibility for planar integration of devices and yield experimental results of 70% coupling efficiency [136]. However, on the material selection of prism, it needs to satisfy not only the requirement that the prism refractive index is larger than the refractive index of waveguide layer, but it also needs to be transparent to the light wavelength used. In addition, it is very sensitive to angle of incidence and slight changes will result in the increased coupling loss [133].

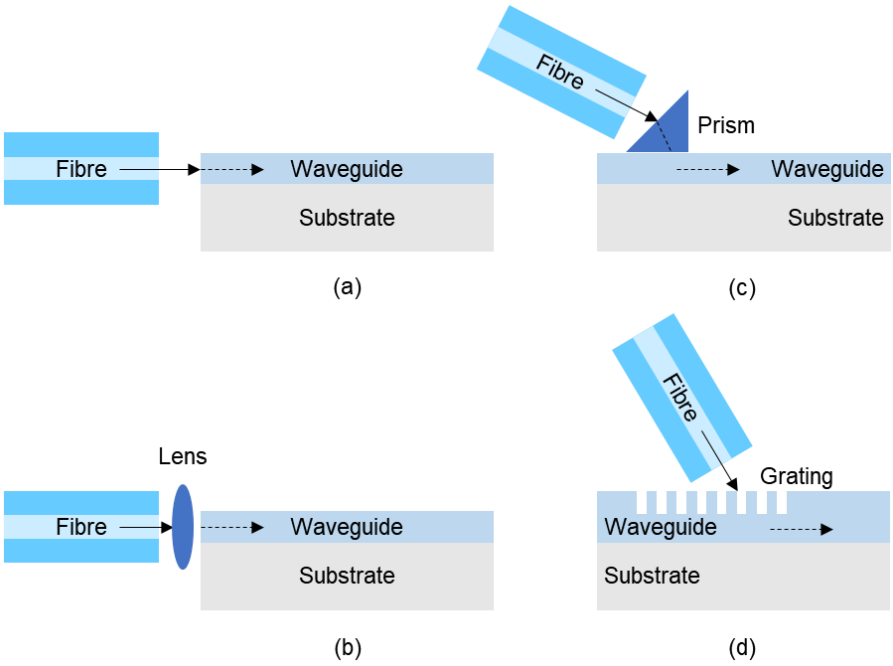

Figure 2.1 Coupler between fibre to waveguide: (a) butt coupler; (b) end-fire coupler; (c) prism coupler; (d) grating coupler. [132]

The grating coupler effectively couples incident light into the waveguide based on the diffraction action of the grating. Grating couplers are mainly used for the input and output of light, which can be placed in any position in the integrated circuit. At the beginning of the development of integrated photonics, people began to study the waveguide grating coupler. In the early stage, it was fabricated by photolithography, which was limited by the lithography process, and its structure was simple and its performance was insufficient. Driven by the new technologies such as micro-nano processing, a variety of new grating couplers are emerging and performance continues to increase [113, 137]. The high-efficiency grating couplers designed by Riccardo Marchetti et al. can achieve 81% of the coupling efficiency at 1550nm in the measurement [138]. Compared with other coupling methods, grating coupling has the following advantages:

1. Reduce process difficulty. There is no need to cleave and polish the end face, which reduces the process steps and avoids the end face wear caused by the complicated production process;
2. Large alignment tolerance. The length and width of the coupling region are equal to the diameter of the fibre core and have great advantages in alignment tolerance;
3. Diverse placement. Grating coupler alignment is relatively easy, can be placed in any position of the chip, allows chip real-time test;
4. Mature technology. The grating coupler structures based on SOI have been widely reported.

A number of publications discussing GaN waveguides have been listed in the Table 2.1 in Chapter 2.2.4. These papers used the above different coupling methods to couple the light beam from the fibre into the waveguide and calculated the loss of the waveguide.

2.2.1 Grating coupling theory

A grating coupler is an optical device which evolved from the principle of grating diffraction, as a method of coupling optical fibres with nanoscale dielectric waveguides. A basic in-out grating coupler setup is shown in Figure 2.2. A laser beam is transmitted by a single mode optical fibre which is placed above the input coupling side. It is diffracted into a waveguide and then coupled out into the free space and collected by a single mode optical fibre placed above the output coupling side.

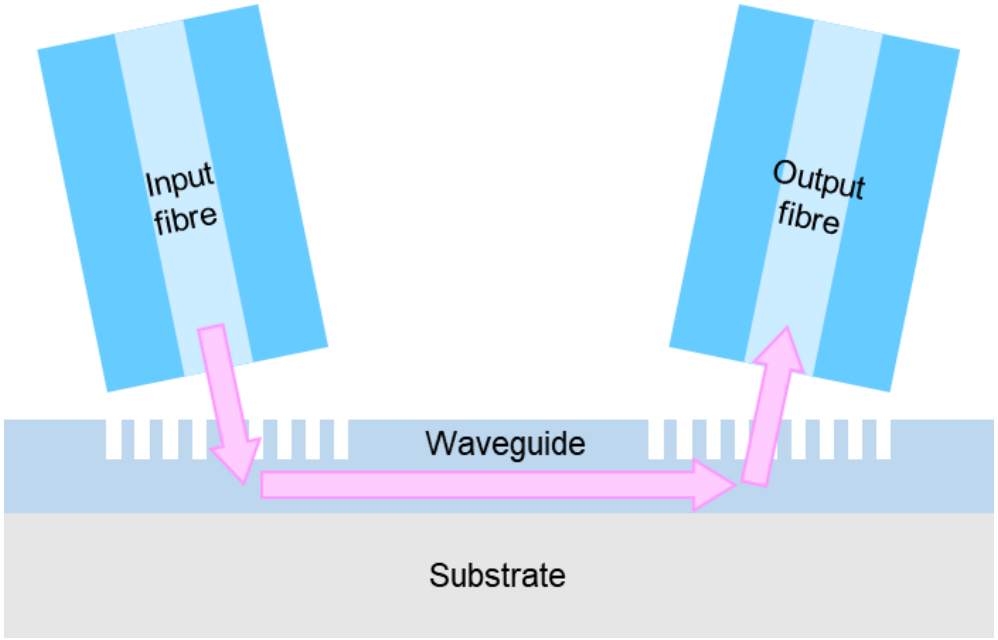

Figure 2.2 Schematic representation of the basic 2D in-out grating couplers setup.

In a basic in-out grating coupler, there are two identical gratings at the input and output. The grating is an optical component with a periodic structure and the light incident light on its surface can be diffracted into many beams in different propagation directions. The gratings used in the integrated optical path have various shapes, such as binary gratings, stepped gratings, blazed gratings, chirped gratings, etc. There is schematic representation of light diffraction by 2D binary relief grating in Figure 2.3.

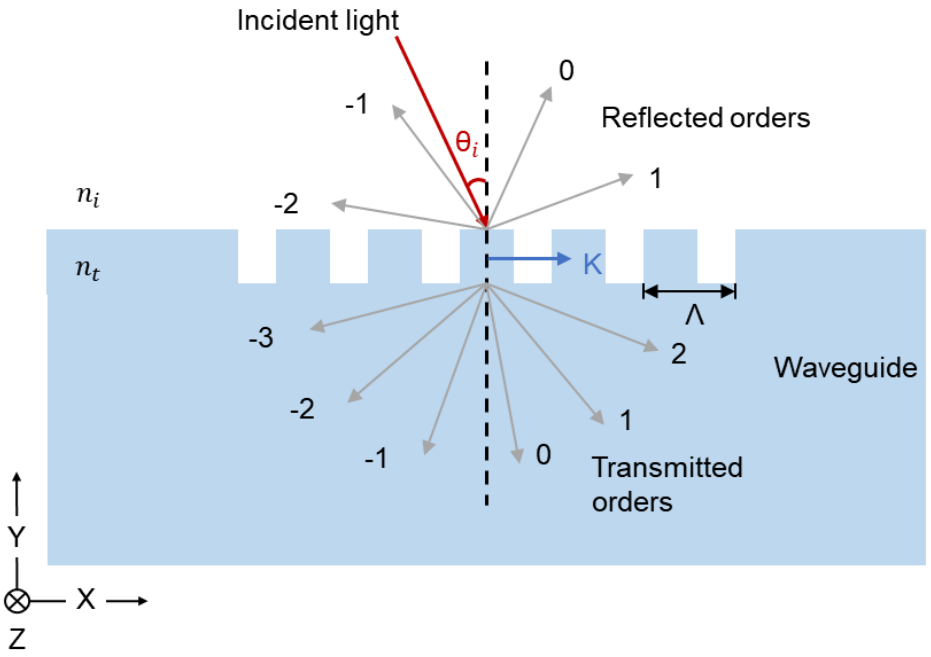

Figure 2.3 Schematic representation of light diffraction by 2D binary relief grating. n_t is the refractive index of the transmission region, n_i is the refractive index of the reflection region and θ_i is the angle of incidence.

Corresponding to the coupling diagram of general grating in Figure 2.3, we define:

x-axis: The direction of the waveguide;

y-axis: The direction of waveguide thickness;

z-axis: The direction of perpendicular to the plane of *x* and *y*.

Regardless of the shape of the grating, according to the Floquet's theorem, the diffracted wavevector is equal to the wavevector of zero order adding or subtracting an integer number of grating vector $\boldsymbol{K}$ [139, 140]

$$\boldsymbol{k_q} = \boldsymbol{k_0} + q\boldsymbol{K} \qquad 2.1$$

Where $\boldsymbol{k_q}$ is the wave vector of the q^{th} space harmonic, $q = 0, \pm1, \pm2, \cdots$, is the diffracted order, $\boldsymbol{k_0}$ is the wave vector of zero order (undiffracted) space harmonic, the magnitude of grating vector has the following relationship to grating period Λ

$$|\boldsymbol{K}| = \frac{2\pi}{\Lambda} \tag{2.2}$$

Since the width of the waveguide is much larger than the wavelength of incident light, the width of the waveguide can be regarded as infinite. The 3D waveguide model is simplified to 2D [141]. Using the coordinates in Figure 2.3, equation 2.1 can also be expressed as

Transmission Region

$$\frac{2\pi n_t}{\lambda}\left(\sin\theta_{tq}\hat{x} + \cos\theta_{tq}\hat{y}\right) = \frac{2\pi n_t}{\lambda}\left(\sin\theta_{\mathrm{t0}}\hat{x} + \cos\theta_{\mathrm{t0}}\hat{y}\right) + \frac{2\pi q}{\Lambda}\hat{x} \tag{2.3}$$

Reflection Region

$$\frac{2\pi n_i}{\lambda}\left(\sin\theta_{rq}\hat{x} + \cos\theta_{rq}\hat{y}\right) = \frac{2\pi n_i}{\lambda}\left(\sin\theta_{\mathrm{r0}}\hat{x} + \cos\theta_{\mathrm{r0}}\hat{y}\right) + \frac{2\pi q}{\Lambda}\hat{x} \tag{2.4}$$

Where θ_q and θ_0 are the angle of q^{th} order and zero order wave, respectively. In the transmission region, counter-clockwise direction is positive order, while in the reflection region it is the opposite order. λ is the incident wavelength.

In the *x* component, the equations 2.3 and 2.4 can be simplified to

Transmission Region $$n_t \sin\theta_{tq} = n_t \sin\theta_{\mathrm{t0}} + q\frac{\lambda}{\Lambda} \tag{2.5}$$

Reflection Region $$n_i \sin\theta_{rq} = n_i \sin\theta_{\mathrm{r0}} + q\frac{\lambda}{\Lambda} \tag{2.6}$$

In the transmission region, based on Snell's law, the refractive index of the incident region n_i and angle of incidence θ_i have the relationship with the refractive index of the transmitted region n_t and the angle of zero order wave θ_{t0}

$$n_i \sin\theta_i = n_{\mathrm{t}} \sin\theta_{\mathrm{t0}} \tag{2.7}$$

In the reflection region, the angle of incidence θ_i have the relationship with the angle of zero order wave θ_{t0} by the law of reflection

$$\theta_i = \theta_{r0} \tag{2.8}$$

So that the diffraction equation can be obtained [140, 142, 143]

Transmission Region $$n_t \sin\theta_{tq} = n_i \sin\theta_i + q\frac{\lambda}{\Lambda} \tag{2.9}$$

Reflection Region $$n_i \sin\theta_{rq} = n_i \sin\theta_i + q\frac{\lambda}{\Lambda} \tag{2.10}$$

This set of diffraction formulas will be used in the parameter design of grating coupler, and the theory of Bragg grating can be derived from the diffraction formula of transmission region.

2.3 Waveguide theory

A waveguide is the most basic optical element of a PIC. Light propagating in a waveguide is confined within the waveguide based on the principle of total internal reflection. Therefore, in the case of three layers slab waveguide, the refractive indices

of the upper and lower dielectrics must be lower than that of the middle waveguide layer. Here, the asymmetric slab waveguide is solved and analysed.

2.3.1 Wave equation in a dielectric media

According to the Maxwell's equations [144]

$$\nabla \cdot \boldsymbol{D}(\boldsymbol{r}, t) = \boldsymbol{\rho}(\boldsymbol{r}, t) \tag{2.11}$$

$$\nabla \cdot \boldsymbol{B}(\boldsymbol{r}, t) = 0 \tag{2.12}$$

$$\nabla \times \boldsymbol{E}(\boldsymbol{r}, t) = -\frac{\partial}{\partial t}\boldsymbol{B}(\boldsymbol{r}, t) \tag{2.13}$$

$$\nabla \times \boldsymbol{H}(\boldsymbol{r}, t) = \frac{\partial}{\partial t}\boldsymbol{D}(\boldsymbol{r}, t) + \boldsymbol{J}(\boldsymbol{r}, t) \tag{2.14}$$

Where $\boldsymbol{D}$ is the electric displacement, $\boldsymbol{B}$ is the magnetic displacement, $\boldsymbol{E}$ is the electric field and $\boldsymbol{H}$ is the magnetic field, $\boldsymbol{r}$ is the position vector at the measured location. That is to say, $\boldsymbol{E}(x, y, z, t) \equiv \boldsymbol{E}(\boldsymbol{r}, t)$, the electric charge density $\boldsymbol{\rho}(\boldsymbol{r}, t)$ and the electric current density $\boldsymbol{J}(\boldsymbol{r}, t)$ are the field sources.

Assuming a region is isotropic and linear medium with no charges and no currents, we have

$$\boldsymbol{D}(\mathbf{r}, \mathrm{t}) = \varepsilon \boldsymbol{E}(\mathbf{r}, \mathrm{t}) \tag{2.15}$$

$$\boldsymbol{B}(\mathbf{r}, \mathrm{t}) = \mu \boldsymbol{H}(\mathbf{r}, \mathrm{t}) \tag{2.16}$$

$$\boldsymbol{\rho}(\boldsymbol{r}, t) = 0 \tag{2.17}$$

$$\boldsymbol{J}(\mathbf{r},\mathrm{t}) = \sigma \boldsymbol{E}(\mathbf{r},\mathrm{t}) = 0 \tag{2.18}$$

where ε, μ and σ denote the permittivity, permeability and conductivity of the medium, respectively.

Maxwell's equations 2.11 -2.14 reduce to

$$\nabla \cdot \boldsymbol{E}(\boldsymbol{r},t) = 0 \tag{2.19}$$

$$\nabla \cdot \boldsymbol{H}(\boldsymbol{r},t) = 0 \tag{2.20}$$

$$\nabla \times \boldsymbol{E}(\boldsymbol{r},t) = -\frac{\partial}{\partial t}\boldsymbol{B}(\boldsymbol{r},t) \tag{2.21}$$

$$\nabla \times \boldsymbol{H}(\boldsymbol{r},t) = \frac{\partial}{\partial t}\boldsymbol{D}(\boldsymbol{r},t) \tag{2.22}$$

So far, the Maxwell's equations 2.19-2.22 go from being in terms of four variables to being in terms of only two variables ($\boldsymbol{E}$ and $\boldsymbol{H}$). Then the equations for time harmonic fields can be found by assuming the time variation as $e^{j\omega t}$, where the fields form become [144]

$$\boldsymbol{E}(\mathbf{r},\mathrm{t}) = Re\left[e^{j\omega t}\boldsymbol{E}(\boldsymbol{r})\right] = \frac{1}{2}\boldsymbol{E}(\boldsymbol{r})\left(e^{j\omega t} + e^{-j\omega t}\right) \tag{2.23}$$

$$\boldsymbol{H}(\mathbf{r},\mathrm{t}) = \mathrm{Re}\left[e^{j\omega t}\boldsymbol{H}(\boldsymbol{r})\right] = \frac{1}{2}\boldsymbol{H}(\boldsymbol{r})\left(e^{j\omega t} + e^{-j\omega t}\right) \tag{2.24}$$

Maxwell's equations can be rewritten as

$$\nabla \cdot \boldsymbol{E}(\boldsymbol{r}) = 0 \tag{2.25}$$

$$\nabla \cdot \boldsymbol{H}(\boldsymbol{r}) = 0 \tag{2.26}$$

$$\nabla \times \boldsymbol{E}(\boldsymbol{r}) = -j\omega\mu\boldsymbol{H}(\boldsymbol{r}) \quad 2.27$$

$$\nabla \times \boldsymbol{H}(\boldsymbol{r}) = j\omega\varepsilon\boldsymbol{E}(\boldsymbol{r}) \quad 2.28$$

By taking the curl of the equation 2.27, for the right side we get

$$\nabla \times (-j\omega\mu\boldsymbol{H}(\boldsymbol{r})) = -j\omega\mu\nabla \times \boldsymbol{H}(\boldsymbol{r}) = \omega^2\varepsilon\mu\boldsymbol{E}(\boldsymbol{r}) \quad 2.29$$

Using the vector identity for the left side, according to the equation 2.25, we get

$$\nabla \times \nabla \times \boldsymbol{E}(\boldsymbol{r}) = \nabla(\nabla \cdot \boldsymbol{E}(\boldsymbol{r})) - \nabla^2\boldsymbol{E}(\boldsymbol{r}) = -\nabla^2\boldsymbol{E}(\boldsymbol{r}) \quad 2.30$$

Hence, we can obtain the wave equation for the $\boldsymbol{E}$ field [144, 145]

$$\nabla^2\boldsymbol{E}(\boldsymbol{r}) + \omega^2\varepsilon\mu\boldsymbol{E}(\boldsymbol{r}) = 0 \quad 2.31$$

Here $\nabla^2\boldsymbol{E}(\boldsymbol{r})$ can be written as

$$\nabla^2\boldsymbol{E}(\boldsymbol{r}) = \hat{x}\nabla^2E_x + \hat{y}\nabla^2E_y + \hat{z}\nabla^2E_z \quad 2.32$$

Where the Laplacian operator in the coordinates is [146]

$$\nabla^2 = \frac{\partial^2}{\partial x^2} + \frac{\partial^2}{\partial y^2} + \frac{\partial^2}{\partial z^2} \quad 2.33$$

Thus, equation 2.32 represents three equations in coordinate system

$$(\frac{\partial^2}{\partial x^2} + \frac{\partial^2}{\partial y^2} + \frac{\partial^2}{\partial z^2})E_x(\boldsymbol{r}) + \omega^2\varepsilon\mu E_x(\boldsymbol{r}) = 0 \quad 2.34$$

$$(\frac{\partial^2}{\partial x^2} + \frac{\partial^2}{\partial y^2} + \frac{\partial^2}{\partial z^2})E_y(\boldsymbol{r}) + \omega^2\varepsilon\mu E_y(\boldsymbol{r}) = 0 \quad 2.35$$

$$(\frac{\partial^2}{\partial x^2} + \frac{\partial^2}{\partial y^2} + \frac{\partial^2}{\partial z^2})E_z(\boldsymbol{r}) + \omega^2\varepsilon\mu E_z(\boldsymbol{r}) = 0 \quad 2.36$$

Where, $k \equiv |\boldsymbol{k}|$ is defined as wavenumber, it satisfies the relation $k^2 = k_x^2 + k_y^2 + k_z^2 = \omega^2 \varepsilon \mu$. $\boldsymbol{k} \equiv \hat{x}k_x + \hat{y}k_y + \hat{z}k_z$ is the wave vector and gives the propagation direction of the electromagnetic wave.

Similarly, we can get the magnetic field equations

$$(\frac{\partial^2}{\partial x^2} + \frac{\partial^2}{\partial y^2} + \frac{\partial^2}{\partial z^2})H_x(\boldsymbol{r}) + \omega^2 \varepsilon \mu H_x(\boldsymbol{r}) = 0 \quad 2.37$$

$$(\frac{\partial^2}{\partial x^2} + \frac{\partial^2}{\partial y^2} + \frac{\partial^2}{\partial z^2})H_y(\boldsymbol{r}) + \omega^2 \varepsilon \mu H_y(\boldsymbol{r}) = 0 \quad 2.38$$

$$(\frac{\partial^2}{\partial x^2} + \frac{\partial^2}{\partial y^2} + \frac{\partial^2}{\partial z^2})H_z(\boldsymbol{r}) + \omega^2 \varepsilon \mu H_z(\boldsymbol{r}) = 0 \quad 2.39$$

2.3.2 TE and TM wave in an asymmetric slab waveguide

Figure 2.4 shows an assumed dielectric waveguide region ($\varepsilon = \varepsilon_0 n^2, \mu = \mu_0$). A wave propagates in the *x*-direction in a 2D asymmetric slab waveguide ($n_1 < n_3 < n_2$). An angle θ is between its propagation of direction and *y*-axis.

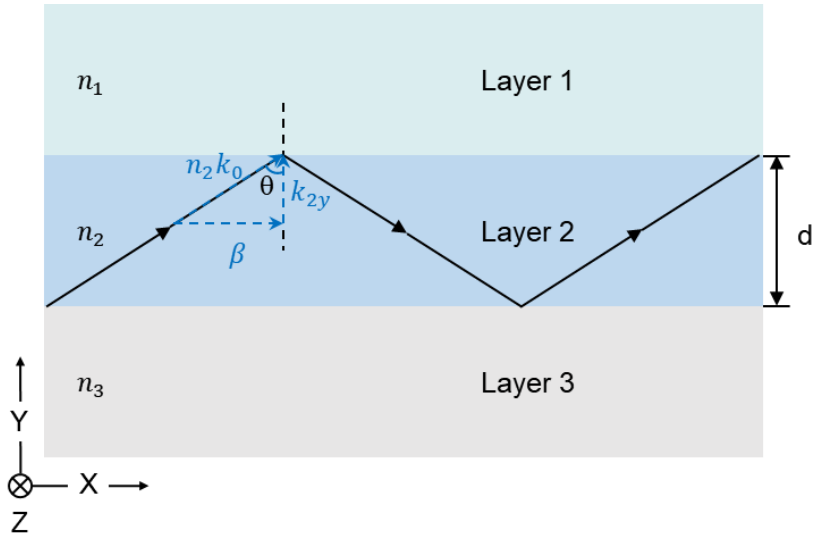

Figure 2.4 An E_z polarised mode source (TE) propagates in an asymmetric 2D slab waveguide. n_1, n_2 and n_3 are the refraction index of material in etch layer, respectively.

In the waveguide wave, the electromagnetic field is transverse spatial distribution along the *x*-direction [144], and the *y*-*z* dependence of the mode can be separated from the *x* dependence, so the propagation form of the plane wave can be defined [146]

$$\boldsymbol{E}(x,y,z,t) = \boldsymbol{E}(x,y)e^{j\omega t-\gamma x} \tag{2.40}$$

$$\boldsymbol{H}(x,y,z,t) = \boldsymbol{H}(x,y)e^{j\omega t-\gamma x} \tag{2.41}$$

Where $\gamma = \alpha + j\beta$ is called the propagation constant of the mode, α is the wave attenuation constant and β is the propagation constant [146]. Here, we consider the wave propagates with no losses, so $\alpha = 0$ and the propagation constant $\gamma = j\beta$ is purely imaginary. Equations 2.40 and 2.41 can be simplified to

$$\boldsymbol{E}(x,y,z,t) = \boldsymbol{E}(x,y)e^{j(\omega t-\beta x)} \tag{2.42}$$

$$\boldsymbol{H}(x,y,z,t) = \boldsymbol{H}(x,y)e^{j(\omega t-\beta x)} \tag{2.43}$$

Based on the model shown in the Figure 2.4, assume that the slab is infinite in the *z*-axis direction, so the refractive index depends only on the *y*-axis, that is, $n = n(x)$. Thus, the equations 2.42 and 2.43 are in the form of

$$\boldsymbol{E}(x, y, z, t) = \boldsymbol{E}(x)e^{j(\omega t - \beta x)} \quad 2.44$$

$$\boldsymbol{H}(x, y, z, t) = \boldsymbol{H}(x)e^{j(\omega t - \beta x)} \quad 2.45$$

Transverse electric (TE) and Transverse magnetic (TM) modes are two types of mode that can occur in a waveguide. For a TE wave, there is no electric field in the direction of propagation, and it only has magnetic field in the direction of propagation. For a TM wave, there is no magnetic field in the direction of propagation, and it only has electric field in the direction of propagation.

When the mode is TE mode with electric field polarised in *z* direction, it means that $E_x = E_y = 0, H_x \neq 0$.

There is no variation in *z* direction. Therefore, we know that

$$E_z(x, y, z, t) = E_z(x)e^{j(\omega t - \beta x)} \quad 2.46$$

$$\frac{\partial}{\partial z}E_z = 0, \frac{\partial^2}{\partial z^2}E_z = 0 \quad 2.47$$

When the mode is TM mode with magnetic field polarised in *z* direction, it means that $H_x = H_y = 0, E_x \neq 0$.

Similarly, we get

$$H_z(x, y, z, t) = H_z(x)e^{j(\omega t - \beta x)} \quad 2.48$$

$$\frac{\partial}{\partial z}H_z = 0, \frac{\partial^2}{\partial z^2}H_z = 0 \quad 2.49$$

According to equations 2.36 and 2.39, the wave equations can be expressed as

TE mode $$\frac{\partial^2}{\partial y^2}E_z(x) + (\omega^2\varepsilon\mu - \beta^2)E_z(x) = 0 \quad 2.50$$

TM mode $$\frac{\partial^2}{\partial y^2}H_z(x) + (\omega^2\varepsilon\mu - \beta^2)H_z(x) = 0 \quad 2.51$$

Where $k^2 = \omega^2\varepsilon\mu = \omega^2\varepsilon_0\mu_0 n^2(x) = k_0^2 n^2(x)$, k_0 is the wavenumber for the free space, $k_0 = \omega\sqrt{\varepsilon_0\mu_0} = \frac{\omega}{c} = \frac{2\pi}{\lambda_0}$

In these three layers, equations of TE mode can be expressed as

Layer 1 $$\frac{\partial^2}{\partial y^2}E_z(x) + (k_0^2 n_1^2 - \beta^2)E_z(x) = 0 \quad 2.52$$

Layer 2 $$\frac{\partial^2}{\partial y^2}E_z(x) + (k_0^2 n_2^2 - \beta^2)E_z(x) = 0 \quad 2.53$$

Layer 3 $$\frac{\partial^2}{\partial y^2}E_z(x) + (k_0^2 n_3^2 - \beta^2)E_z(x) = 0 \quad 2.54$$

Hence, we can obtain the general solution for each layer [1]

$$E_z(\mathrm{x}) = A_j e^{jk_{iy}x} + B_j e^{-jk_{iy}x},\ i = 1, 2, 3 \quad 2.55$$

Where A_j and B_j are two complex conditions. Since the $k_0 n_i$ is fixed and it with β and k_{iy} satisfy the Pythagorean Theorem which confirms what we have derived from Figure 2.4, we obtain the equation in three layers.

$$k_{\mathrm{iy}}^2 = k_0^2 n_i^2 - \beta^2,\ i = 1, 2, 3 \quad 2.56$$

And also get the relationship in layer 2

$$\beta = n_2 k_0 \sin\theta \tag{2.57}$$

Where k_{iy} is the propagation constant in the *y*-direction in each layer.

When we vary β [1]:

1. If $\beta > n_i k_0$, $i = 1, 2, 3$, then $\sqrt{k_0^2 n_1^2 - \beta^2}$, $\sqrt{k_0^2 n_2^2 - \beta^2}$and $\sqrt{k_0^2 n_3^2 - \beta^2}$ will be imaginary and the general solutions 2.55 of each layer will be a function of exponential.
2. If $\beta < n_i k_0$, $i = 1, 2, 3$, then $\sqrt{k_0^2 n_2^2 - \beta^2}$ and $\sqrt{k_0^2 n_1^2 - \beta^2}$ or $\sqrt{k_0^2 n_3^2 - \beta^2}$ will be all be real and the general solutions 2.55 of each layer will be a function of sinusoidal.

The two cases above are not what we are interested in, the guided modes should satisfy $\beta < n_2 k_0$ but $> n_1 k_0$ and $> n_3 k_0$, then $\sqrt{k_0^2 n_2^2 - \beta^2}$ will be real and the solutions in layer 2 will be a function of sinusoidal but $\sqrt{k_0^2 n_1^2 - \beta^2}$ and $\sqrt{k_0^2 n_3^2 - \beta^2}$ will be imaginary leading to exponential solution in those layers.

In addition, we also know that the propagation constant of the waveguide is the effective index times the vacuum wavenumber [1]

$$\beta \equiv n_{eff} k_0 \tag{2.58}$$

Thus, the guided modes need to satisfy the following conditions

$$n_3 < n_{eff} < n_2 \tag{2.59}$$

$$n_{eff} = n_2 \sin\theta \tag{2.60}$$

In a similar process, it is easy to get the same conditions of TM mode, which is ignored here.

2.3.3 Slab waveguide dispersion relation

The theory of waveguide propagation has been described in the previous section. Here waveguide dispersion is analysed starting from a symmetrical and uniform slab. As shown in Figure 2.5, the thickness of the plane is *d*, and the material is GaN. The upper and bottom layer is air. It is assumed that the plane is infinite in the *x* and *z* directions. Therefore, the change of dielectric constant ε is independent of the *x* and *z* directions and only related to the *y*-axis, that is, it is a function of *y* [147].

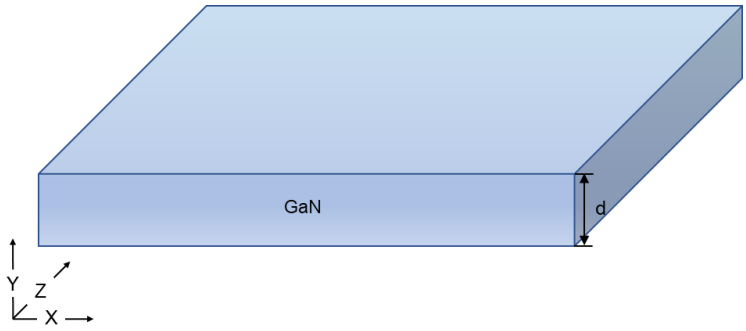

Figure 2.5 Schematic of a slab GaN waveguide.

The dispersion relation relates the wavenumber to its frequency. When the wave guided along the *x*-axis, its dispersion relation can be expressed as ω vs k_x, which is given by expression 2.56

$$k_x = \beta = \sqrt{k_0^2 n_{slab}^2 - k_y^2} = \sqrt{\omega^2 \varepsilon_0 \mu_0 n_{slab}^2 - k_y^2} \qquad 2.61$$

The symmetric slab dispersion diagram is shown in Figure 2.20. There are two straight line in the diagram. Top one is the free space light line, which satisfies equation $\omega = ck_x$. When the mode in the blue area which is above the free space line, that is, $\omega > ck_x$, the angle between propagation direction and *x*-axis is less than critical angle. This spectrum of states is the continuum. It will lead to radiation modes, and the energy will radiate out into free space. This blue area is called the light core. Only modes between two lines can be guided in the waveguide. The figure only shows the dispersion curves of the first five low-order TE modes. The intersection of each guided mode with the free space light line is the cutoff frequency of the mode. The bottom line is the material light line, which satisfies equation $\omega = \frac{ck_x}{n_{slab}}$. With the increase of wavenumber k_x, the larger order of the existing guided modes m, the smaller angle between the propagation direction and the *x*-axis, but always larger than the critical angle [144, 147].

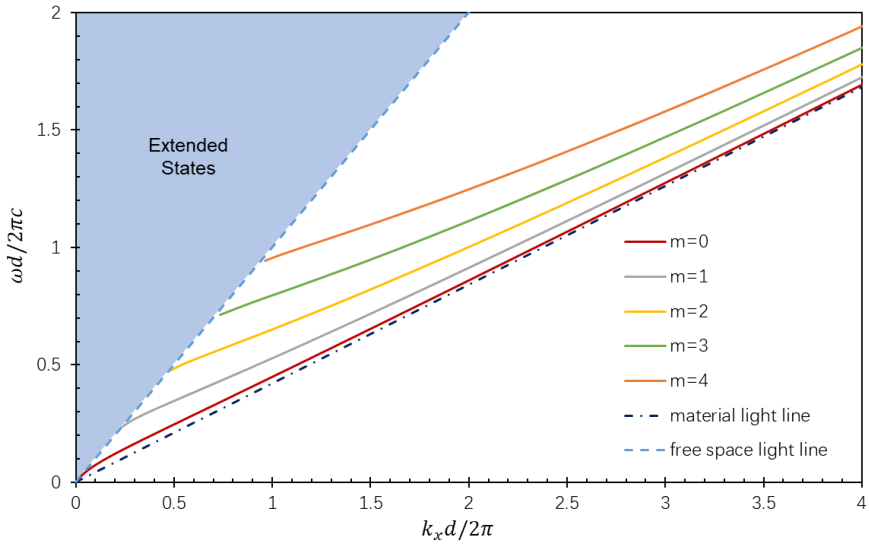

Figure 2.6 Dispersion relation diagram for the first five TE modes in a slab GaN waveguide with thickness d (n_{slab} = 2.38 [148]).

Now change the substrate from the free space to sapphire, the schematic representation of structure is illustrated in Figure 2.7. Based on the above theory, the dispersion

diagram of GaN on sapphire waveguide structure can be obtained in Figure 2.8. The guides modes are confined between the light lines of sapphire and GaN.

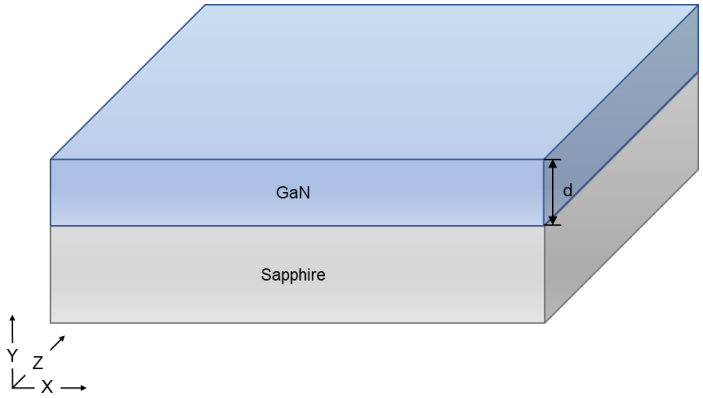

Figure 2.7 Schematic of a GaN on sapphire waveguide.

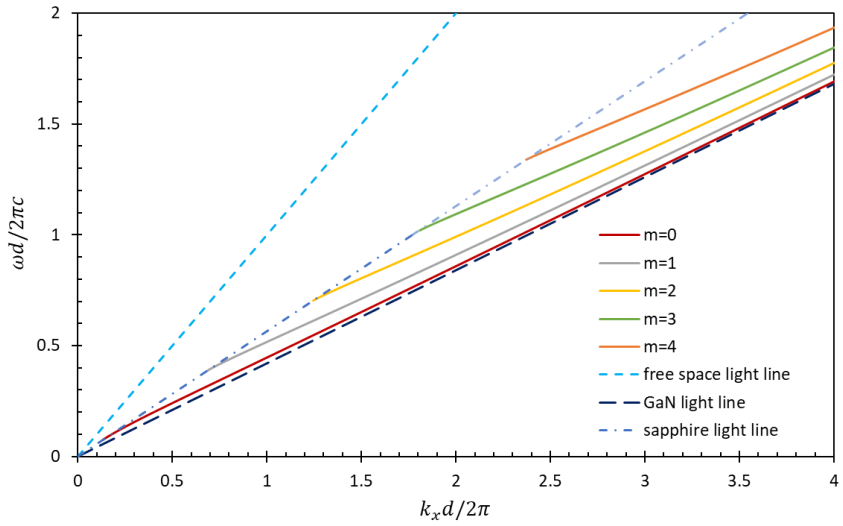

Figure 2.8 Dispersion relation diagram for the first five TE modes in a GaN on sapphire waveguide with thickness d (n_{GaN} = 2.38 [148], $n_{sapphire}$ = 1.77 [149]).

2.3.4 Examples of GaN waveguide

As mentioned in section 1.4, GaN platforms have great potential in visible waveguides. However, the research on GaN waveguides is not very extensive at present. The results of some different structures of GaN waveguides are listed in the Table 2.1.

Waveguide structure	Coupling method	Wavelength	Optical loss	Ref
AlN/GaN short period-superlattice cladding layer to the GaN waveguide	prism	TE wave at 632.8 nm	1 dB/cm	[118]
GaN-AlN-Si waveguide	prism	TE wave at 632.8 nm TM wave at 632.8 nm	1.9 dB/cm 3.4 dB/cm	[150]
GaN on sapphire	grating	TE+TM wave at 639 nm	3.9 dB/mm	[151]
GaN on sapphire stripe waveguide	end-fire	TE wave at 700 nm	2 dB/cm	[119]
GaN on sapphire ridge waveguide	inverse tapers	TE wave at 1330 nm	10 dB/cm	[115]
GaN-AlN/AlGaN-Si free-standing grating coupler with waveguide	grating	TE wave at 1455 nm	5 dB coupling and waveguide loss	[152]
GaN waveguide with AlN/GaN short period-superlattice	prism	TE wave at 1550 nm	0.65 dB/cm	[153]
GaN/AlGaN ridge waveguides	end-fire	TE wave at 1560 nm TM wave at 1560 nm	best 0.9 dB/cm, average 1.6 dB/cm best 1.5 dB/cm, average 2.3 dB/cm	[154]

Table 2.1 Examples of GaN-based waveguide.

Currently, based on different fabrication conditions and different coupling techniques, Henk Schenk et al. and Maksym Gromovyi et al. measured the lowest waveguide loss

in the visible range is 1-2 dB/cm [118, 150]. At the wavelength near 1550 nm, the GaN waveguide structure proposed by Arnaud Stolz et al. has the lowest waveguide coupling loss. They used transmission electron microscopy and waveguide prism to couple the light into the waveguide and reduced the plane loss to 0.65 dB/cm through the AlN/GaN short-period superlattice structure [153].

2.4 Cavities theory

PhC is a new type of artificial optical structure formed by the periodic distribution of dielectric materials with different dielectric constants. The periodic distribution of dielectric materials makes this structure have many excellent optical characteristics and can affect the propagation of electromagnetic waves. The most important characteristic is the existence of a photonic band gap. Electromagnetic waves of any frequency located in the stop band region are forbidden to propagate. Through theoretical research on the band structure of PhCs, it can be used to make a variety of optical devices. In general, the wider the band gap, the better the performance of the PhC. Therefore, exploring the PhC structure with a wider band gap has become one of the main research directions in this field.

Another feature of PhCs is that they have the characteristics of localised control. Introducing impurities or defects, the periodicity of the PhC dielectric properties is destroyed and corresponding defect states are generated in the PhC. Such defect states can be point defects, line defects, etc. The stronger the local capacity, the smaller the energy loss, and the higher the quality factor Q of a PhC with a defect state. This localisation property is the important metrics for sensing performance of a PhC defect state sensor.

Figure 3.11 shows the spontaneous emission in free space, in photonic band gap crystal (suppressed), and in defective PhC (enhanced).

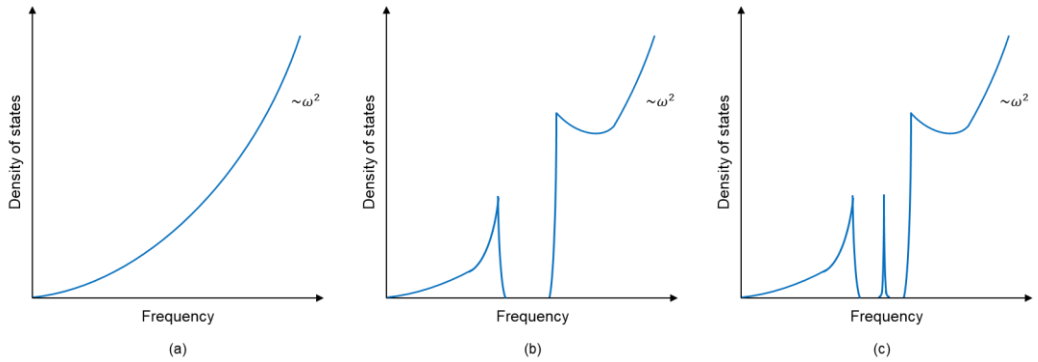

Figure 2.9 A density of optical states for (a) free space; (b) PhC band gap; (c) introducing defect in PhC.

The stopband produced by the Bragg grating described in this section is a band gap of 1D PhC structure. When a waveguide cavity is introduced as a line defect between two Bragg gratings, resonance peaks are generated in the stopband.

2.4.1 Distributed Bragg Reflectors

When a periodic grating structure is introduced into the waveguide, the refractive index of the waveguide changes periodically. The guided light will be diffracted into the waveguide, the substrate and the upper medium. There is a special case: When this grating is a Bragg grating, energy coupling occurs between the guide modes transmitted forward and the guide modes transmitted backward. Finally, a specific wavelength of light is reflected back in the waveguide, and the central wavelength of the reflected light is related to the period of the grating structure. The Bragg grating reflector used in waveguide structures is called Distributed Bragg Reflectors (DBR). The reflected band

is defined as a stopband. The working principle of a 2D Bragg waveguide grating is shown in Figure 2.10.

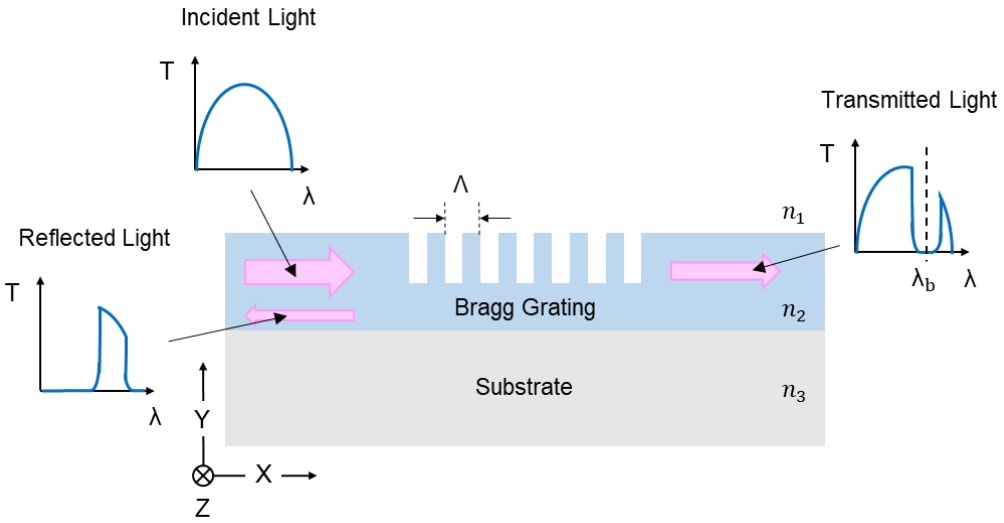

Figure 2.10 Schematic representation of a 2D Bragg waveguide grating. Λ is the period of Bragg grating and n_1, n_2 and n_3 are the refraction index of material in etch layer, respectively.

Based on the equation 2.10, the diffraction equation at the output coupling can be written as

Reflection Region $$n_2 \sin\theta_{rm} = n_{eff} + m\frac{\lambda}{\Lambda} \quad (2.62)$$

Where $m = 0, \pm1, \pm2, \cdots$, is the diffracted order for output part.

According to the equation 2.58, the phase matching condition of output grating can be obtained

$$\beta_{rm} = \beta_i + m\frac{2\pi}{\Lambda} \quad (2.63)$$

Where β_i and β_{rm} are waveguide propagation constants of incident and m^{th} diffracted order light in the transmission direction, respectively.

For the Bragg waveguide gratings, β_i and β_{rm} satisfy the following relationship [155]

$$\beta_{rm} = -\beta_i = \frac{2\pi}{\lambda} n_{eff} \quad 2.64$$

Thus, substituting equation 2.64 into equation 2.63, phase matching condition is simplified to

$$\frac{2}{\lambda_b} n_{eff} = m \frac{1}{\Lambda} \quad 2.65$$

Where the central wavelength of the reflected light λ_b that satisfies the above relationship is defined as the Bragg wavelength

$$m\lambda_b = 2n_{eff}\Lambda \quad 2.66$$

Here, m represents the m^{th} order Bragg grating.

2.4.2 Fabry-Perot cavity

The schematic representation of an Fabry-Perot cavity is shown in Figure 2.11. It consists of two same DBRs and an isolated cavity. Because the transmittance of Bragg grating is very small in the stopband, the light propagates back and forth between the two reflectors multiple times. After the frequency selection of resonant cavity, the specific wavelengths of light corresponding to the cavity mode accumulates energy in the resonant cavity and is emitted through the second DBR grating. Thus, some small high transmittance windows appear in the stopband. The fully etched DBRs cavity is an ideal resonance spectrum with a series of extremely narrow resonance windows. Figure 2.12 shows the transmittance of an Fabry-Perot cavity.

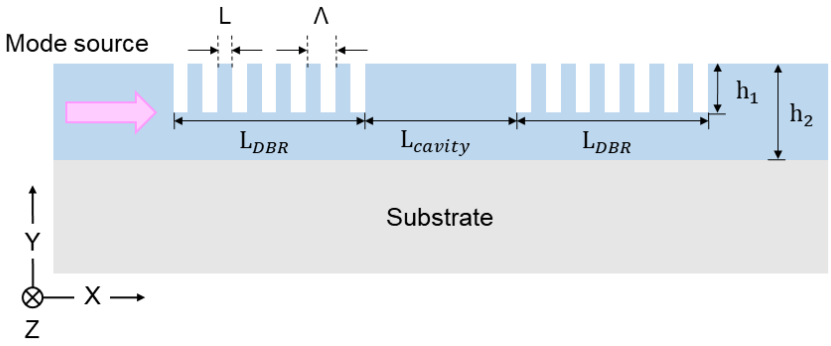

Figure 2.11 Fabry-Perot cavity formed by two DBRs and a cavity. Λ is the period of Bragg grating, $a = L/\Lambda$ is filling factor of Bragg grating, h_1 is the etch depth of Bragg grating, h_2 is the height of waveguide, L_{DBR} and L_{cavity} are the physical lengths of DBR and cavity, respectively.

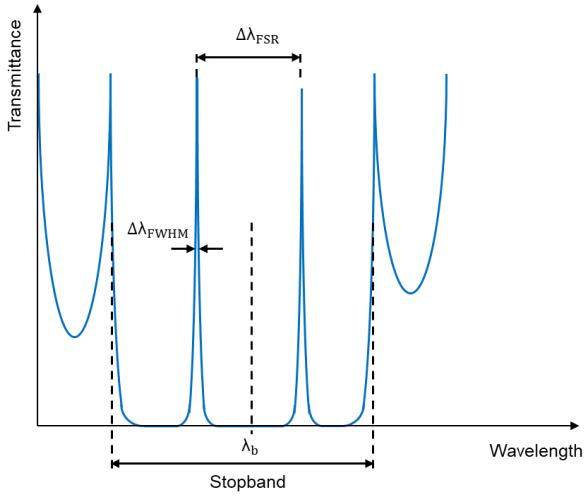

Figure 2.12 Transmittance spectrum of Fabry-Perot cavity. Λ is the period of Bragg grating, L/Λ is filling factor of Bragg grating, h_1 is the etch depth of Bragg grating, h_2 is the height of waveguide, L_{DBR} and L_{cavity} are the length of DBR and cavity, respectively.

The particular wavelengths of light that satisfies the resonance condition can be emitted. In general, it can be expressed as

$$\beta = \frac{2q\pi}{L}, q = 0, 1, 2, \ldots \qquad 2.67$$

Where L in the Fabry-Perot cavity case is the distance of light round trip in the cavity structure.

Therefore, propagation constant difference between any two adjacent resonance peaks can be written as

$$\Delta\beta = \frac{2\pi}{L} \tag{2.68}$$

According to the 2.58, propagation constant is a function of the wavelength

$$\beta(\lambda) = \frac{2\pi}{\lambda} n_{eff(\lambda)} \tag{2.69}$$

Then expanding the equation 2.69 in first order Taylor series

$$\beta(\lambda) \approx \beta(\lambda_0) + \frac{\partial\beta}{\partial\lambda}(\lambda - \lambda_0) = \beta(\lambda_0) + \frac{\partial\beta}{\partial\lambda}\Delta\lambda \tag{2.70}$$

Further rewrite as

$$\Delta\beta = \beta(\lambda) - \beta(\lambda_0) = \frac{\partial\beta}{\partial\lambda}\Delta\lambda \tag{2.71}$$

Where we consider λ and λ_0 to be two wavelength peaks.

Combining equations 2.68 and 2.71, the wavelength spacing between two resonance peaks, which is defined as the free spectral range (FSR), can be expressed as [156]

$$|\Delta\lambda_{FSR}| = \frac{2\pi}{L}\left|\left(\frac{\partial\beta}{\partial\lambda}\right)^{-1}\right| \tag{2.72}$$

The $\left|\left(\frac{\partial\beta}{\partial\lambda}\right)\right|$ part can be derived as

$$\left|\left(\frac{\partial\beta}{\partial\lambda}\right)\right| = \frac{2\pi}{\lambda^2}\left[n_{eff(\lambda)} - \lambda\frac{\partial n_{eff(\lambda)}}{\partial\lambda}\right] = \frac{2\pi}{\lambda^2} n_{eff_g} \tag{2.73}$$

Where n_{eff_g} is the group effective refractive index of waveguide in the cavity. It has the following expression for refractive index and wavelength in vacuum [157]

$$n_{eff_g} = n_{eff} - \lambda \frac{dn}{d\lambda} \tag{2.74}$$

So that the FSR can be obtained

$$\Delta\lambda_{FSR} = \frac{\lambda^2}{n_{eff_g} L} \tag{2.75}$$

Where L in the Fabry-Perot cavity case is expressed as the twice sum of the cavity length L_{Cavity} and the effective lengths of the two DBRs $L_{eff-DBR}$ [158].

$$L = 2(L_{eff-DBR} + L_{Cavity} + L_{eff-DBR}) \tag{2.76}$$

Equation 2.76 can be calculated by the DBR effective length $L_{eff-DBR}$ formula [158, 159]

$$L_{eff-DBR} = L_{DBR} \frac{\sqrt{R}}{2\,\mathrm{atanh}(\sqrt{R})} \tag{2.77}$$

Where R is the reflectance of a single DBR.

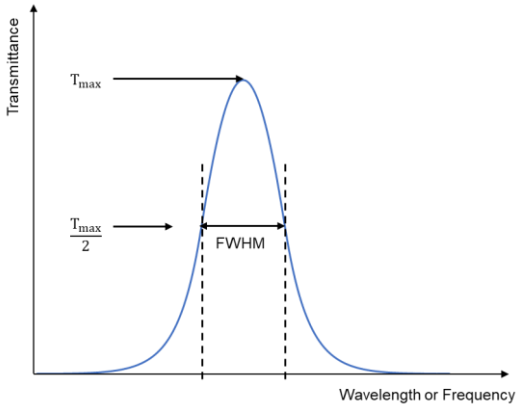

Figure 2.13 FWHM in a transmittance spectrum.

The concept of quality factor Q is a dimensionless parameter in physics and engineering. It is physical quantity representing the damping property of the oscillator [160], and it can also represent the ratio of the resonance peak of frequency f_0 or wavelength λ_0 to its full-width at half-maximum (FWHM) bandwidth in a resonator [161]. FWHM is the spectral width between two points equal to half the maximum transmittance. An expression for FWHM can be found in Figure 2.13.

For resonance systems, the Q factor can also be calculated by the following formula [162]

$$Q = \frac{f_0}{\Delta f_{FWHM}} = \frac{\lambda_0}{\Delta \lambda_{FWHM}} \qquad 2.78$$

Grating coupler allows to couple an outside light source in and out of a waveguide and DBRs cavity can generate a resonant peak within the stopband. Based on these performances, a sensor design is proposed in Figure 2.14. A DBRs cavity which is the Fabry-Perot resonator formed by two further gratings form is integrated in the waveguide. Figure 2.15 shows the light couples into the slab waveguide and the Fabry-Perot resonator creates a multitude of resonance peaks in the stop band. The effective refractive index n_{eff} will be changed when the analyte is present at the sensor surface. It will lead to a $\Delta\lambda_{shift}$ shift of the resonance curve [163]. This could be detected using a low cost tunable laser and a detector.

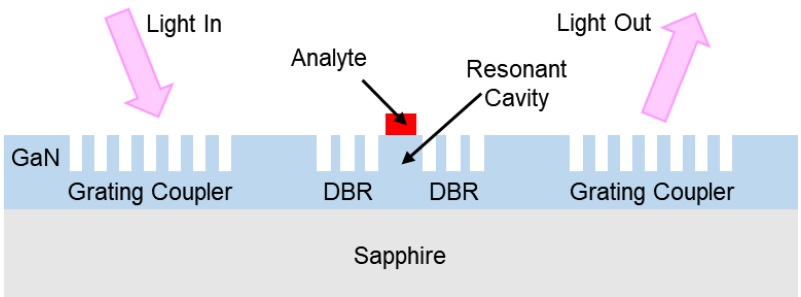

Figure 2.14 Schematic representation of 2D proposed grating sensor with analyte.

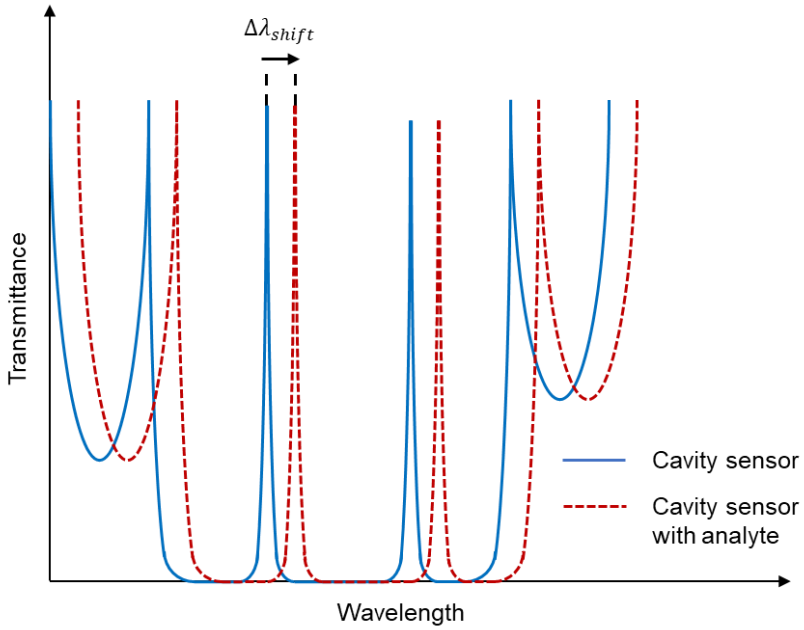

Figure 2.15 Transmittance spectra of cavity sensor with and without analyte.

Sensitivity *S* is a quantity used to describe the property of a sensor. For the optical sensor based on the refractive index method introduced in this chapter, the sensitivity *S* can be expressed as

$$S = \frac{\Delta\lambda_{shift}}{\Delta n} \tag{2.79}$$

Where, the unit of sensitivity is nm/RIU.

2.4.3 Examples of GaN cavity

Currently, the research on the PhC cavities of GaN with high Q factor has made great progress. Some microcavity examples based on GaN platform are given in the Table 2.2, which make GaN an attractive candidate for biological or chemical sensors.

Cavity structure	Wavelength	Performance	Ref
GaN grating coupler with DBRs cavity	640 nm	200 Q factor	[151]
GaN DBRs cavity	720 nm	175 Q factor	[164]
GaN suspended nanobeam cavity	411.7 nm	740 Q factor	[165]
GaN-AlN-sapphire H1 cavity	486 nm	2200 Q factor	[166]
GaN PhC L7 cavity with two embedded InGaN/GaN quantum wells	420 nm	5200 Q factor	[167]
GaN on Si L3 PhC cavity	1300 nm	16900 Q factor	[124]
GaN on Si L3 PhC cavity	1300 nm	44000 Q factor	[125]
GaN-AlN-sapphire L3 cavity	462 nm	65975 Q factors	[162]
GaN-AlN-sapphire H1 cavity	459 nm	65700 Q factors	
GaN grating coupler with DBRs cavity	640 nm	200 Q factor	[151]

Table 2.2 Examples of GaN-based PhC cavity.

Mohamed Sabry Mohamed et al. obtained the highest quality factor with a theoretical maximum of 80,000 and a measurement of up to 44,000 by optimising the cavity 2D GaN on Si L3 PhC cavity [125].

2.5 Summary

This chapter introduces the principles of coupling grating, waveguide, Bragg grating, resonator and band diagram. By using these theories, the parameters and properties of

simple single-mode structures can be calculated. However, when complex problems need to be solved, such as multi-mode waveguide transmission and complex structure, etc., the theoretical calculation method is not applicable. After elaborating the theory, the next chapter will introduce the calculation method of software simulation structure.

3 Methods

3.1 Introduction

There are many methods for numerical calculation of electromagnetic fields. Currently, the three methods are widely used, which are Finite-Difference Time-Domain (FDTD) method, Finite-Integration Time-Domain method and Finite-Element method. This thesis uses the FDTD method. In this chapter, the core theory of the algorithm is firstly introduced, and then several examples structures mentioned in the previous chapter are simulated. The comparison between the theoretical results of the simple GaN structure and the simulation results are discussed.

The second part of the chapter will briefly introduce the measurement set up. This is a set up that contains the input and output fibre for the measurement of the sample grating coupling. During the measurement of many chips, we gradually improved some parts of the set up to obtain more accurate experimental results.

The final part of this chapter will briefly introduce the sample fabrication. The samples to be measured in the following chapter were manufactured by University of Bath using Displacement Talbot Lithography (DTL) + Direct Laser Writing (DLW) technology.

3.2 Finite difference time domain method

In Chapter 2, grating coupler and cavity theories were introduced. Although theoretical calculations can clearly illustrate the physical principles of simple structures, actual structures can be very complex and contain multiple patterns. Therefore, we often need to use some numerical simulation methods. Here, we use the FDTD method to simulate our realistic structures.

After more than 50 years of development, the FDTD method has become the most classical method in the time domain and has been applied more and more widely in many fields of electromagnetic research. It is mainly applied in the following aspects:

1. Analysis of antenna radiation characteristics, such as microstrip antennas and antenna arrays.
2. Applications in guided wave and microwave devices, such as dielectric waveguides, waveguide coupling, resonator devices, etc.
3. Periodic structure analysis, such as grating propagation characteristics, periodic antenna arrays and photonic band gap structures.
4. Calculation of radar cross section, such as the radar cross section of complex objects.
5. Application in electromagnetic compatibility, such as the simulation of nuclear electromagnetic pulse, etc.
6. Time-domain analysis of optical path in micro-optics components.

7. Applications in biological electromagnetism.

3.2.1 The FDTD algorithm

In 1966, Kane S. Yee put forward a new method of numerical calculation of electromagnetic fields for the first time, called the FDTD method [168]. Its principle is to use the central difference approximation to replace Maxwell's curl equations. A 3D Yee's cell is shown in Figure 3.1, Yee proposed that every electric field or magnetic field component is surrounded by four magnetic field components or electric field components. Furthermore, the electric and magnetic field components are staggered in time where the electric field updates are processed at half time step between successive magnetic field updates and vice versa.

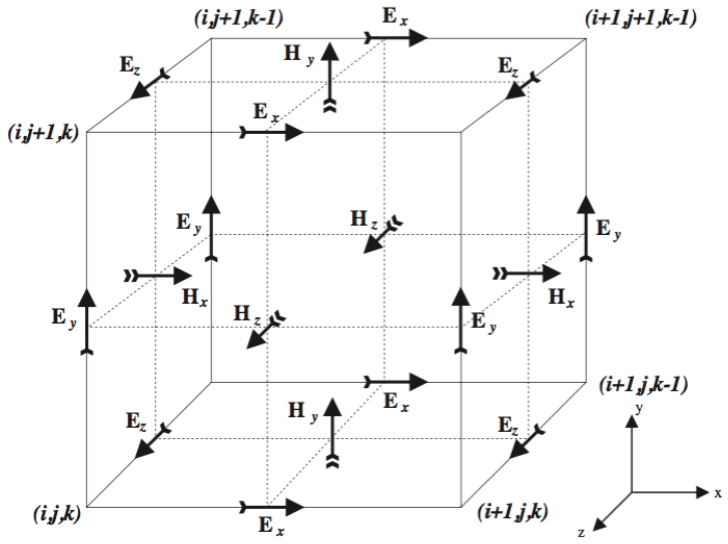

Figure 3.1 A Yee's cell for three-dimensional implementation of the FDTD [168]

The equations 3.1 and 3.2 can be used to explain that the equations 2.21 and 2.22 can be transformed to finite difference formulation in time.

$$\nabla \times \boldsymbol{E}(r)|_t = -\mu \frac{\boldsymbol{H}(r)|_{t+\Delta t/2} - \boldsymbol{H}(r)|_{t-\Delta t/2}}{\Delta t} \quad 3.1$$

$$\nabla \times \boldsymbol{H}(r)|_{t+\Delta t/2} = \varepsilon \frac{\boldsymbol{E}(r)|_{t+\Delta t} - \boldsymbol{E}(r)|_t}{\Delta t} \quad 3.2$$

And the equations 2.21 and 2.22 also can be expanded in coordinates [169]

$$\frac{\partial H_x}{\partial t} = \frac{1}{\mu}\left(\frac{\partial E_y}{\partial z} - \frac{\partial E_z}{\partial y}\right) \quad 3.3$$

$$\frac{\partial H_y}{\partial t} = \frac{1}{\mu}\left(\frac{\partial E_z}{\partial x} - \frac{\partial E_x}{\partial z}\right) \quad 3.4$$

$$\frac{\partial H_z}{\partial t} = \frac{1}{\mu}\left(\frac{\partial E_x}{\partial y} - \frac{\partial E_y}{\partial x}\right) \quad 3.5$$

$$\frac{\partial E_x}{\partial t} = \frac{1}{\varepsilon}\left(\frac{\partial H_z}{\partial y} - \frac{\partial H_y}{\partial z}\right) \quad 3.6$$

$$\frac{\partial E_y}{\partial t} = \frac{1}{\varepsilon}\left(\frac{\partial H_x}{\partial z} - \frac{\partial H_z}{\partial x}\right) \quad 3.7$$

$$\frac{\partial E_z}{\partial t} = \frac{1}{\varepsilon}\left(\frac{\partial H_y}{\partial x} - \frac{\partial H_x}{\partial y}\right) \quad 3.8$$

Combining equations 3.3-3.8 with equations 3.1 and 3.2 can obtain the finite difference equations in space and time. For example, the finite difference equation for E_x is explained as

$$\frac{H_z^{i,j,k}|_{t+\Delta t/2} - H_z^{i,j-1,k}|_{t+\Delta t/2}}{\Delta y} - \frac{H_y^{i,j,k}|_{t+\Delta t/2} - H_y^{i,j,k-1}|_{t+\Delta t/2}}{\Delta z} = \varepsilon \frac{E_x^{i,j,k}|_{t+\Delta t} - E_x^{i,j,k}|_t}{\Delta t} \quad 3.9$$

Where *i*, *j* and *k* are the position of Yee's cell in the 3D grid.

According those equations, the core FDTD algorithm can be shown in Figure 3.2.

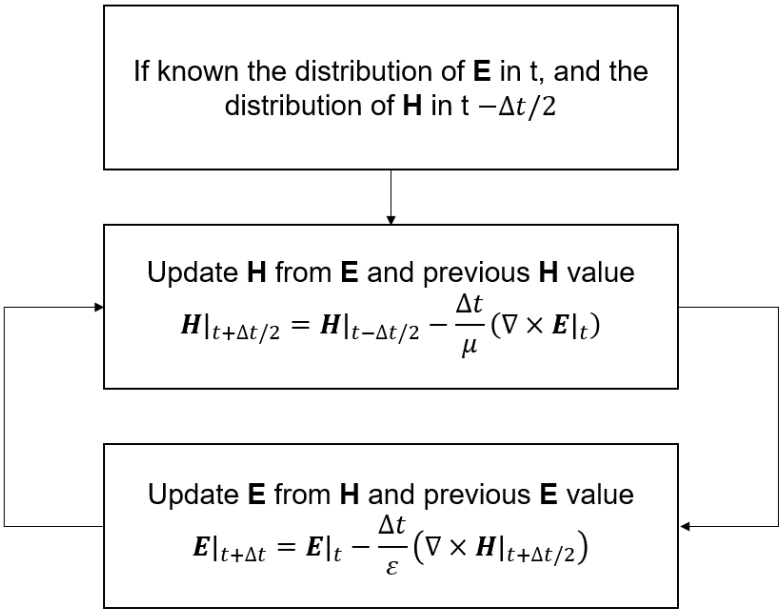

Figure 3.2 Flow chart of FDTD iteration

3.2.2 Mode source

Lumerical FDTD package [170] offers a number of options for sources types, but for the design of the DBRs cavity sensor, we are only interested in mode sources. The mode source is used to inject a guided mode into the simulated waveguide structure. According to the dimensions of the simulation (2D or 3D), the light source is calculated as a line or plane. The thickness of the waveguide and the size of the source are used to calculate how many guided modes can be supported. According to the mode selection function, we can select the mode to inject.

3.2.3 Boundary conditions

Boundary setting is an important step in electromagnetic field numerical calculation. Common boundaries are Perfect Match Layer (PML), metal, periodic, symmetric, anti-symmetric, Bloch and Perfect Magnetic Conductor. PML is the main boundary condition used in this thesis. This boundary is suitable for the case where light is transmitted completely on the boundary, the ideal PML boundary can absorb light waves and produce zero reflection. When PML boundary conditions are applied, the whole structure needs to be built within the simulation area, which makes the simulation computation time increased. Symmetric/anti-symmetric or periodic boundary conditions can be selected to reduce the memory and time required. When the simulated structure is symmetric and the electromagnetic field of the light source has a symmetric plane in the middle of the simulated region, symmetric/anti-symmetric boundaries can be used in the symmetric direction to reduce the simulation volume and time. Here, the symmetric and antisymmetric boundaries are magnetic and electrical symmetric boundaries, respectively. When studying periodic systems, it is possible to calculate only one unit by using periodic boundary, which greatly reduces the size of the structure. A Bloch boundary is also a periodic boundary, but there is a phase difference between adjacent boundaries, which is used to simulate and calculate the band structure of PhCs.

3.2.4 Mesh size

FDTD is a time-domain spatial discretisation algorithm. Therefore, both time signals and spatial fields need to be discretised. The time step of general software is limited by the size of the spatial grid. When the mesh size is smaller, the time step will be smaller, so the time length (the light travel time) and the modelling time is longer.

Under the condition of the other settings are correct, the finer mesh leads to smaller numerical dispersion and higher result accuracy.

Mesh accuracy is an index of mesh size used by FDTD to set the auto non-uniform mesh size. It has a total of 8 accuracies, which is listed in Table 3.1 [171].

Mesh accuracy	**Mesh Size**
Mesh accuracy = 1	minimum wavelength/6
Mesh accuracy = 2	minimum wavelength/10
Mesh accuracy = 3	minimum wavelength/14
Mesh accuracy = 4	minimum wavelength/18
Mesh accuracy = 5	minimum wavelength/22
Mesh accuracy = 6	minimum wavelength/26
Mesh accuracy = 7	minimum wavelength/30
Mesh accuracy = 8	minimum wavelength/34

Table 3.1 Mesh accuracy corresponding to mesh size.

3.3 Simulation examples

This section will simulate some simple GaN structures and compare the simulation results with the theoretical values calculated based on the principles of the previous chapter.

For the simulation of 2D grating coupler, we choose the PML boundary condition to simulate the input part of the grating. In the simulation structure, the fibre structure with an angle is added, and the mode light source is placed in the fibre at the same angle to simulate the input fibre.

For 2D Bragg gratings and DBRs cavity modelling, PML boundary conditions and mode light sources are still used. Here the mode light source is placed in the waveguide and incident horizontally.

For band structure diagram, we chose Bloch boundary conditions in the direction of refractive index change, and PML boundary conditions in the other directions, and only simulated single-period injection mode source.

3.3.1 Grating couplers

The basic structure of the light propagation in the grating couplers is shown in Figure 3.3. The incident light goes into the input grating, then it will diffract into reflected orders and transmitted orders. Some beams of transmitted orders which satisfy the guided modes conditions can propagate in waveguide and diffract at the output grating. Therefore, the beams can be received from the output grating.

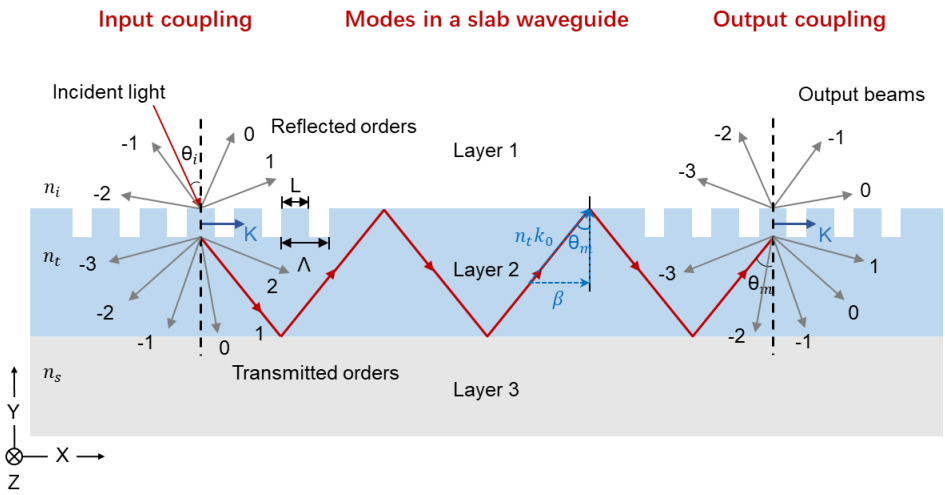

Figure 3.3 Schematic representation of an E_z polarised mode source (TE) diffracts by 2D binary relief grating, then propagate in a 2D slab waveguide and diffract by the same grating.

In an in-out grating coupler system, if the input grating and the output grating are the same and the input fibre and output fibre are the same angle, the mode angle in the waveguide is the incident angle to the output grating. The optical path of the output grating part can be regarded as the reverse input grating part. Therefore, we only discuss the input coupling part in this example. The structure is shown in the Figure 3.4. Here, the incident light in the fibre is set to fundamental TE mode (E_z polarised) and fundamental TM mode (H_z polarised) at 640nm wavelength. GaN-on-sapphire was used as an input grating structure. The refractive index of GaN gratings and waveguide is 2.38 [148]. The refractive index of sapphire substrate is 1.77 [149], and the cover region is air. According to the one-dimensional mode solver [172], the waveguide thickness supporting a single TE or TM mode at 640 nm wavelength can be found in the Figure 3.5. The range of waveguide thickness is from 48 nm to 248 nm, which are definitely no higher orders modes. To verify the theoretical formula, we use 200 nm thick GaN-on-sapphire input grating to ensure the fundamental TE or TM mode transmission.

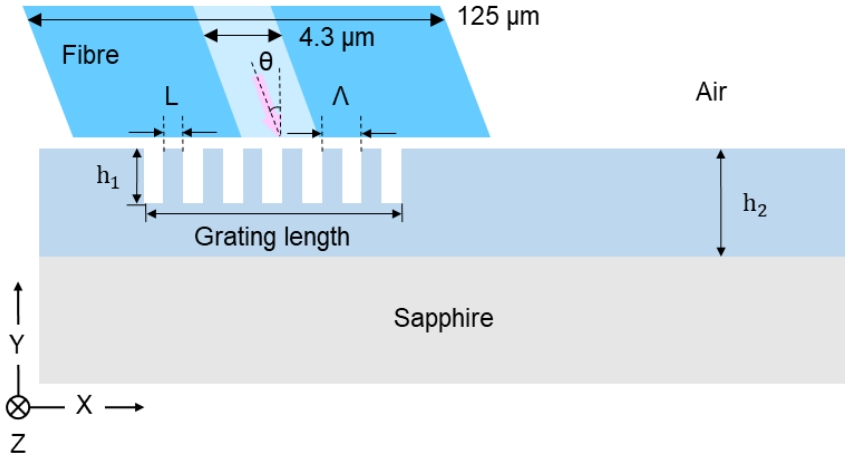

Figure 3.4 GaN on sapphire 2D binary input grating with single mode fibre. Device parameters: n_{GaN} *= 2.38,* $n_{sapphire}$ *= 1.77, waveguide height* h_2 *= 200 nm, filling factor = a =* L/Λ *= 0.5, grating length = 18 μm, incident wavelength = 640 nm, fundamental TE or TM modes with varying the etch depth* h_1 *and grating period* Λ*.*

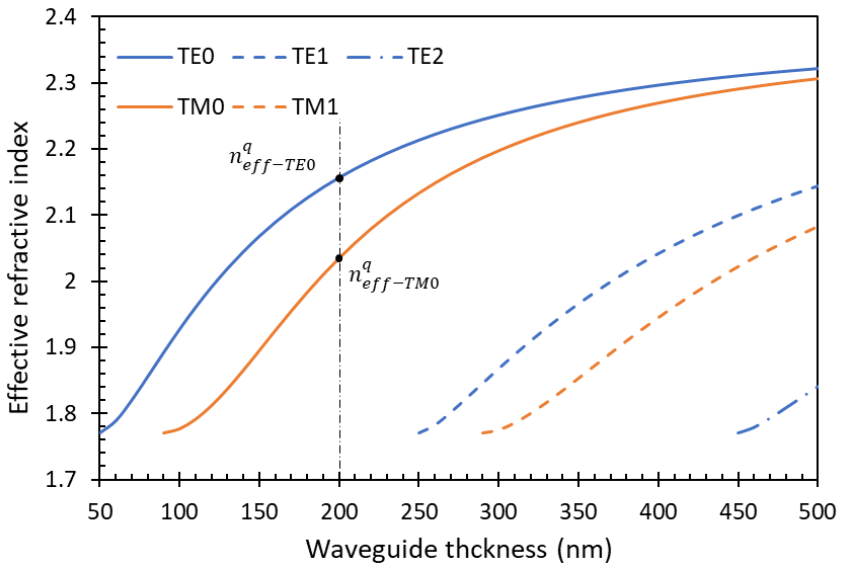

Figure 3.5 1D mode solver-effective index vs. thickness of waveguide at 640 nm wavelength.

As shown in Figure 3.4, there are four design parameters for gratings: grating length, grating period, filling factor and etch depth, where grating period is the length of unit grating Λ; filling factor $a = L/\Lambda$. In addition, there are also two design parameters for

the incident light: wavelength and angle of incident light. we set grating length = 18 μm, filling factor = 0.5 to find the grating period at 15 ° angle of incidence in 640 nm.

According the equations 2.9, 2.59 and 2.60, we have the diffraction equation for input coupling

$$n_{eff}^{q} = n_{GaN}\, sin\, \theta_q = n_{air}\, sin\, \theta_i + q\frac{\lambda}{\Lambda} \tag{3.10}$$

The equation 3.10 can be simplified to

$$\Lambda = \frac{q\lambda}{n_{eff}^{q} - sin\, \theta_i} \tag{3.11}$$

Where n_{eff}^{q} = 2.1573 for TE_0 mode, n_{eff}^{q} = 2.0352 for TM_0 mode which be calculated analytically by the one-dimensional mode solver [172].

Thus, for fundamental TE incident mode, when q = 1, the grating period should be 337 nm; when q = 2, the grating period should be 674 nm. For fundamental TM incident mode, when q = 1, the grating period should be 360 nm; when q = 2, the grating period should be 720 nm.

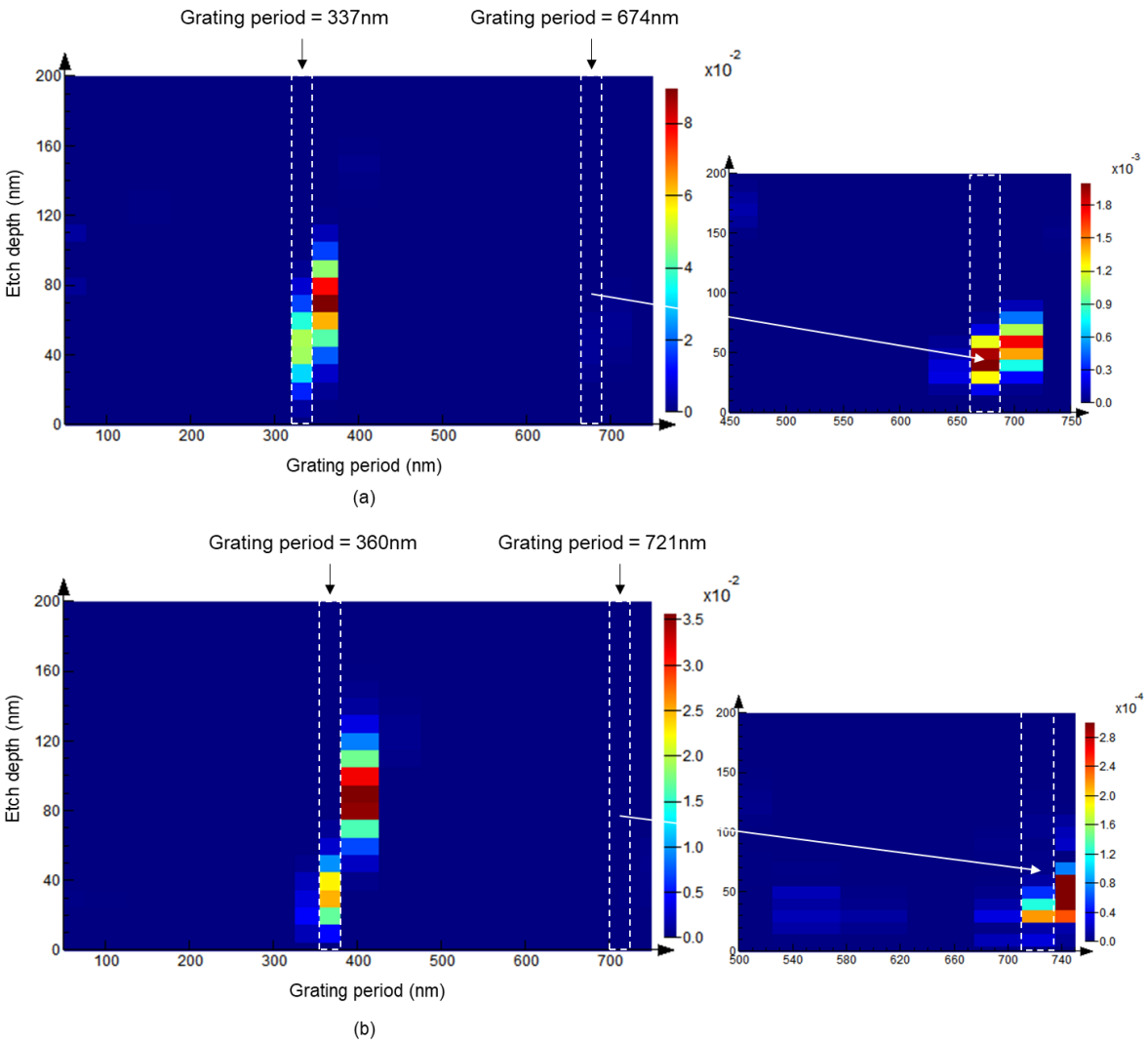

Figure 3.6 Input coupling transmission at 640 nm wavelength: (a) fundamental TE mode incident; (b) fundamental TM mode incident.

Figure 3.6 is the transmittance result at 640 nm wavelength with varying the etch depth and grating period by using Lumerical FDTD. It can be seen that most of the best transmittances are mostly around 337.11 nm grating period and 360 nm grating period for TE mode and TM mode, respectively. There is also some transmittance at 674 nm and 720 nm grating period for TE mode and TM mode, respectively. That means the transmittance of first diffracted order is better than that of the second diffraction order. However, due to difference between FDTD software and theoretical calculation, there will be some slight deviations. Some of the best transmittances correspond to grating

periods in the modelling results that are not exactly at 337 nm and 674 nm for TE mode and 360 nm and 720 nm for TM mode, but fall near the theoretical results. The simulation results show that the coupling efficiency can be optimised by adjusting the etching depth and filling factor.

3.3.2 Bragg grating and DBRs cavity

Based on the structure diagram in Figure 3.7, we discuss the structure of 500 nm thick GaN on sapphire as an example. Figure 3.7 (a) is the schematic representation of a single Bragg grating structure and Figure 3.7 (b) is the schematic representation of Fabry-Perot cavity. Here, the mode source set as the E_z polarised fundamental TE mode; Bragg grating period Λ is 400 nm, filling factor a is 0.5; etch depth h_1 is 250 nm; the height of waveguide h_2 is 500 nm, number of a single Bragg grating period is 15; physical length of cavity L_{cavity} is 13 μm.

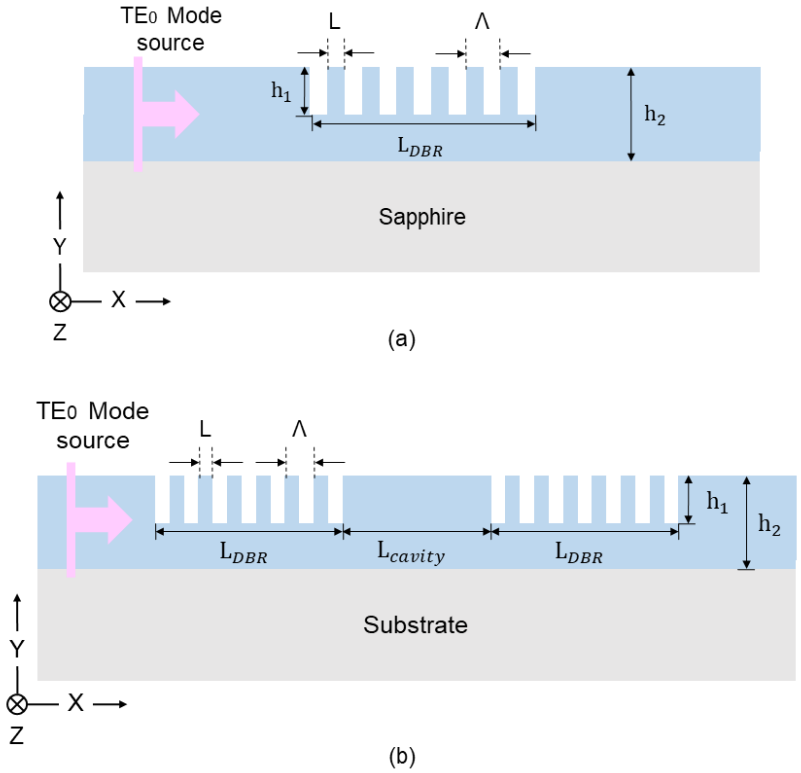

Figure 3.7 (a) Geometry of GaN on sapphire single Bragg grating; (b) Geometry of GaN on sapphire DBRs cavity. Device parameters: n_{GaN} = 2.38, $n_{sapphire}$ = 1.77, waveguide height h_2 = 500 nm, grating period Λ = 400 nm, etch depth h_1 = 250 nm, filling factor = $a = L/\Lambda$ = 0.5, number of single Bragg grating period = 15.

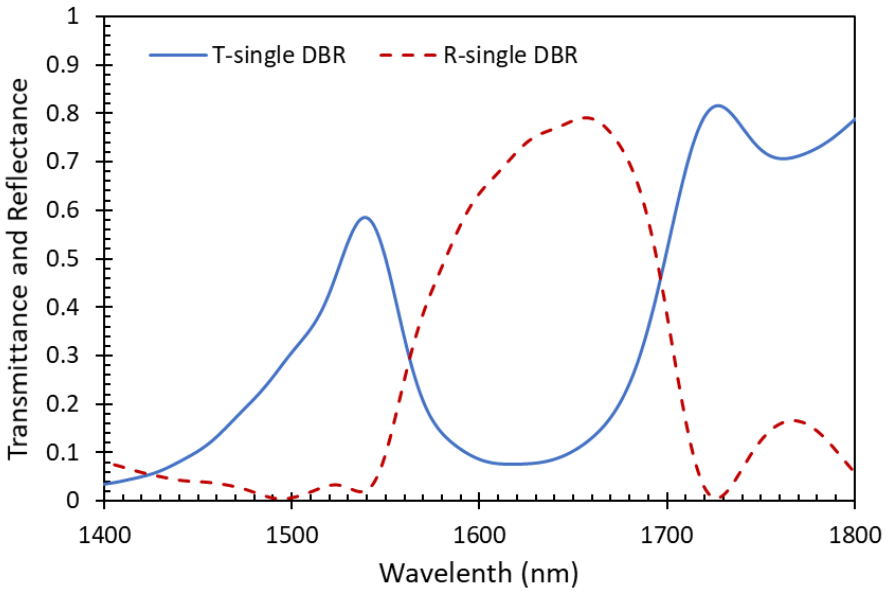

Figure 3.8 Simulated TE_0 mode source transmittance and reflectance spectra of a single DBR.

The simulation results of single DBR described in Figure 3.7 (a) by Lumerical FDTD are shown in Figure 3.8. The red curve indicates the reflectance of a single Bragg grating and the blue curve representing the transmittance. They show a significant band gap centred at a wavelength of 1625 nm.

The Bragg grating can be seen as a structure consisted of two alternating dielectric layers with same thickness. The refractive index in the tooth area is the effective refractive index of the fundamental TE mode of the slab waveguide of thickness h_2. Similarly, the refractive index in the groove area is the effective refractive index of the fundamental TE mode of the slab waveguide of thickness h_1. Therefore, the effective refractive index of this grating can be expressed as [173]

$$n_{eff}^{grating} = \mathrm{a}n_{eff}^{tooth} + (1-a)n_{eff}^{groove} \qquad 3.12$$

Where, through the one-dimensional mode solver [172], n_{eff}^{tooth} and n_{eff}^{groove} are 2.1530 and 1.9228 respectively.

Therefore, the theoretical value of the Bragg wavelength λ_b calculated by the equation 2.66 is 1630 nm (m = 1), which is close to the simulation result.

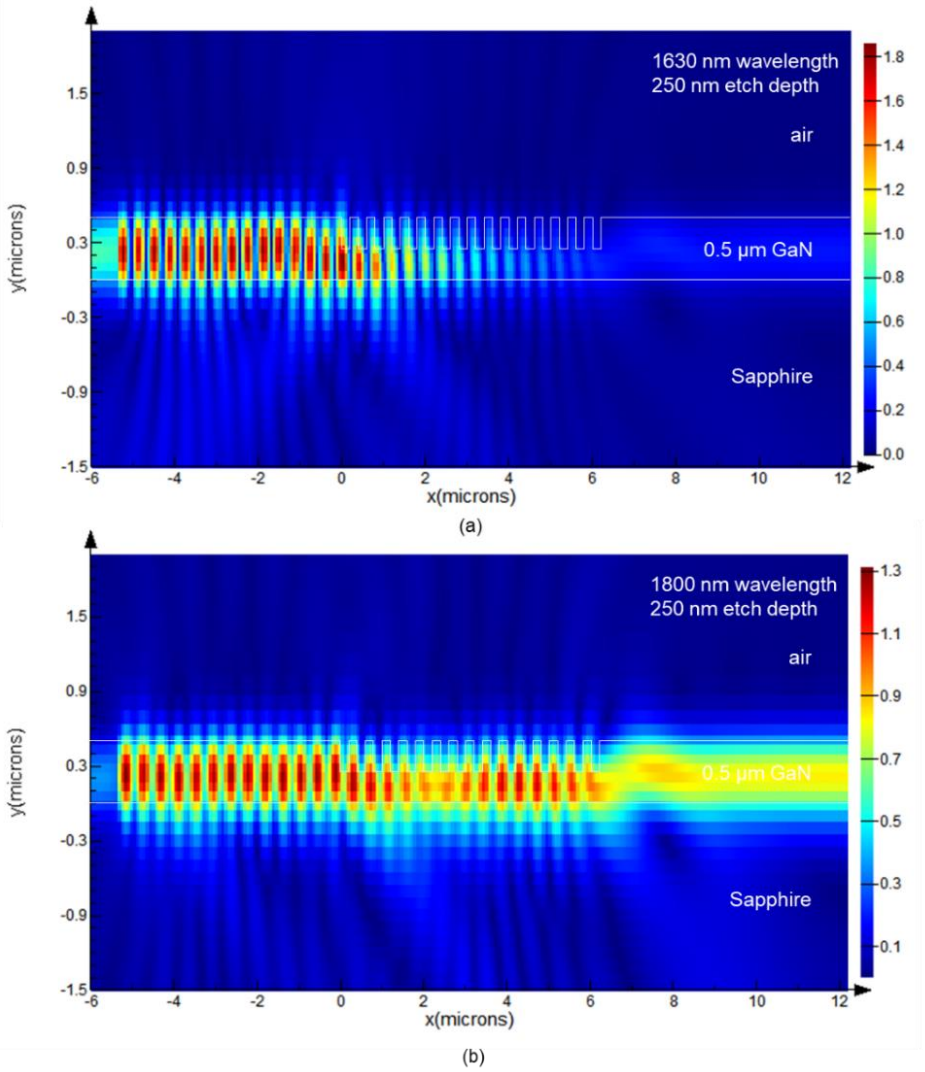

Figure 3.9 E_z field distribution in cross-section, TE_0 mode propagating from left to right. Grating parameters: filling factor = 0.5, grating period = 400 nm, etch depth = 250 nm, number of periods = 15. (Vertical and horizontal axes not to scale). (a) wavelength = 1630 nm; (b) wavelength = 1800 nm.

Figure 3.9 is the cross-section E_z field distributions at 1650 nm and 1800 nm wavelength. Figure 3.9 (a) shows the light in the stopband which cannot travel through the grating and is almost completely reflected. Figure 3.9 (b) shows only the light that is not in the stopband can continue to propagate.

Figure 3.10 is the modelling transmittance result of the Fabry-Perot cavity described in Figure 3.7 (b). Some obvious resonance peaks can be seen in the stopband. Their

wavelength are 1554.94 nm, 1579.52 nm, 1610.92 nm, 1643.6 nm, 1677.63 nm and 1708.22 nm. Here, $\Delta\lambda_{FSR}$ between 1610.92 nm and 1643.6 nm is 32.68 nm.

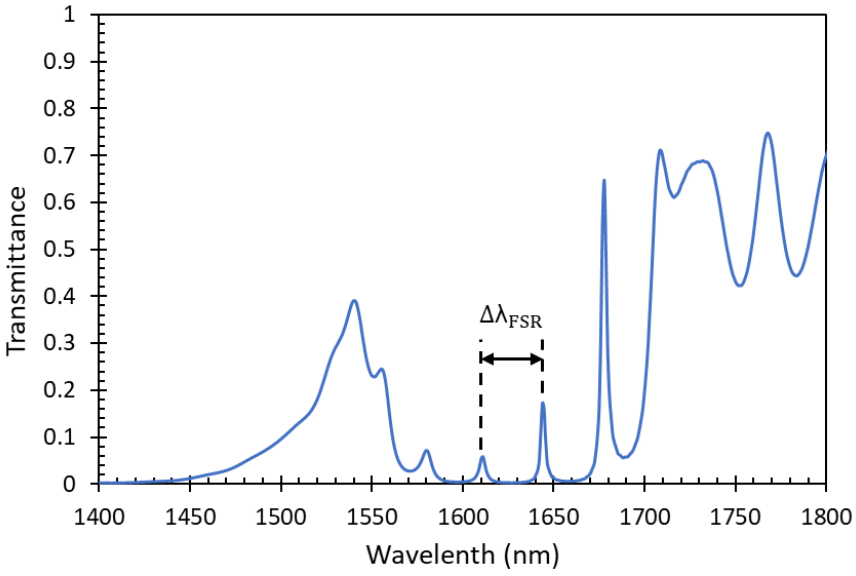

Figure 3.10 Simulated TE_0 mode source transmittance spectrum of a Fabry-Perot cavity.

The maximum reflectance *R* of single DBR is 0.7915 in Figure 3.8. From the equations 2.77, the theoretical value $L_{eff-DBR}$ can be found as

$$L_{eff-DBR} = (15 \times 400 + 200)\frac{\sqrt{0.7915}}{2\,\mathrm{atanh}(\sqrt{0.7915})} = 1941.844\ nm$$

This effective Bragg grating length can also be seen in the Figure 3.9 (a) above.

Figure 3.11 shows the effective index in the cavity vs. wavelength. $\frac{dn}{d\lambda}$ = -0.1738 is the slope of the trend line formula. the n_{eff} = 2.1497 for TE_0 mode at 1643.6 nm wavelength. Thus, we know the n_{eff_g} from equations 2.74 is

$$n_{eff_g} = 2.1497 - 1.6436 \times (-0.1738) = 2.4354$$

Finally, the $\Delta\lambda_{FSR}$ can be calculated by equation 2.75 as

$$\Delta\lambda_{FSR} = \frac{1643.6^2}{2.4354\times2\times(1941.844+13000+1941.844)} = 32.85\ nm$$

The $\Delta\lambda_{FSR}$ = 32.85 nm is consistent with the simulation results 32.68 nm.

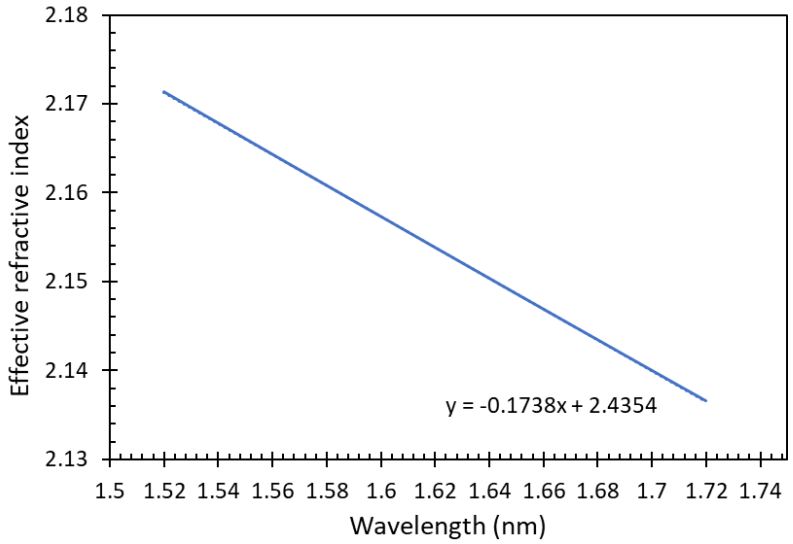

Figure 3.11 1D mode solver-effective index vs. wavelength.

3.3.3 Band structure

The previous chapter introduced the Bragg grating structure. The effective refractive index of the groove of grating is n_{eff_L}, and the effective refractive index of the tooth part is n_{eff_H}, so the Bragg grating structure can be regarded as a 1D PhC composed of materials with two alternating refractive indices periods (n_L and n_H) in the propagation direction. Figure 3.12 introduces this multilayer film.

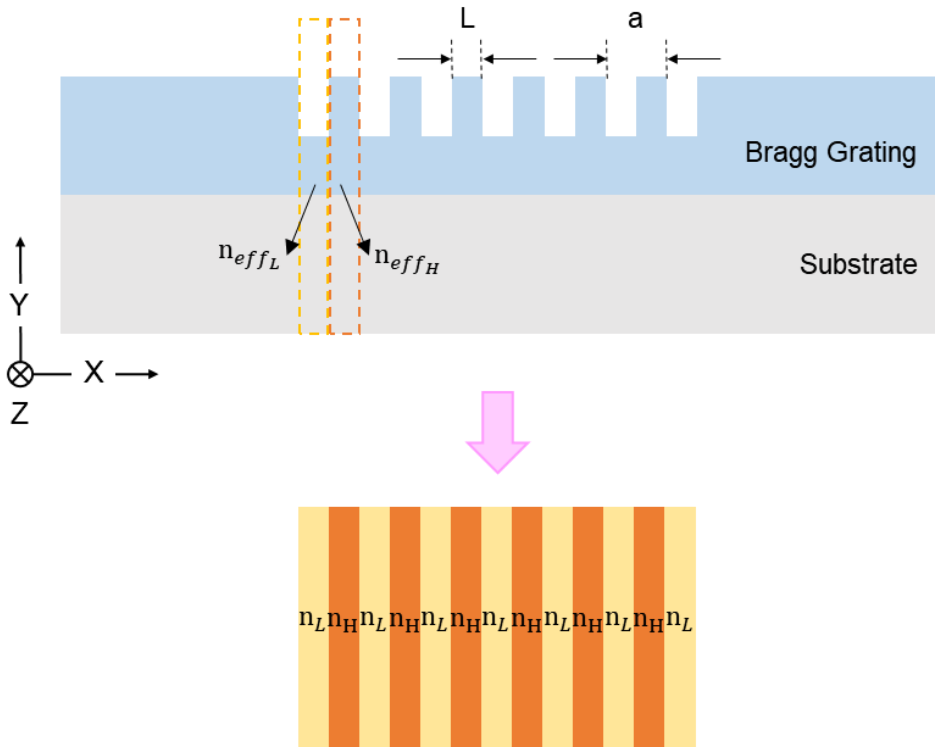

Figure 3.12 From Bragg grating to multilayer film.

According to the Bragg grating parameters in section 3.3.2, the effective refractive indices n_L and n_H are 1.9228 and 2.1530, respectively [172].

Figure 3.13 (a) is the result of a 2D FDTD Bragg grating simulation, which is the expression of converting wavelength vs. transmittance and reflectance in Figure 3.7 to transmittance and reflectance vs. frequency. Figure 3.13 (b) is the band gap diagram of multilayer film with alternating refractive indices simulated by plane wave expansion method on MATLAB [174]. In the figure, there is a significant band gap between 177 THz and 190 THz frequency, which is consistent with the stopband obtained by the FDTD simulation in Figure 3.13 (a).

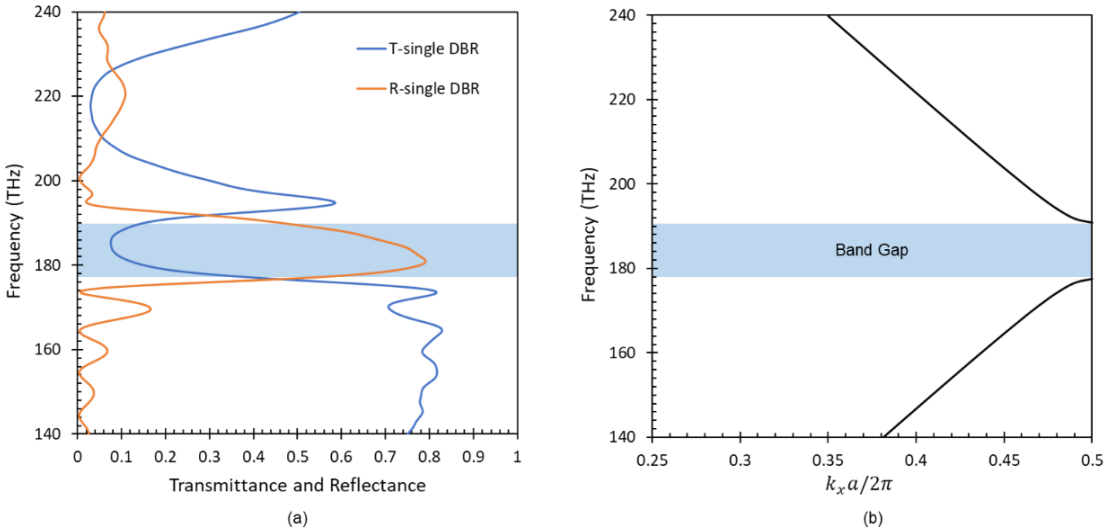

Figure 3.13 (a) FDTD modelling transmittance and reflectance spectrum of a single DBR for TE_0 mode source. (b) Band structure diagram for 1D multilayer film, refractive indices alternate between 1.9228 and 2.1530, grating period a = 400 nm.

Band gap diagrams can also be obtained using FDTD software. In the software, we select the E_z polarised fundamental mode source which propagates in *x*-axis, set the boundary condition in the *x* direction as Bloch and the boundary condition in the *y* direction as PML, run the 2D simulation of the grating structure within a period, and band structure diagram obtained is shown in Figure 3.14. The band gap is the same as in Figure 3.13. The Free space light line and substrate light lines are marked with arrows. It can also be seen that a "leaky mode" exists in the upper band of the bandgap. The frequency of that mode will gradually leaks out of the waveguide in to the substrate [175, 176].

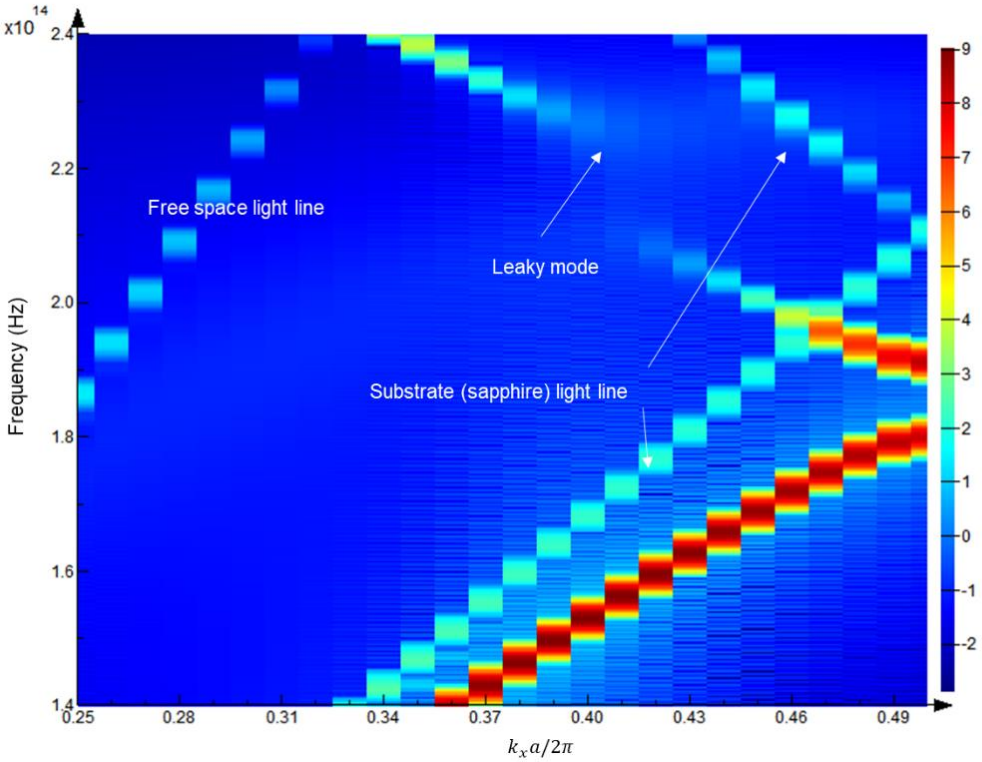

Figure 3.14 FDTD modelling Band structure of a single DBR for TE_0 mode source.

3.4 Measurement set up

The initial in-out coupling test set up is described in Figure 3.15 and Figure 3.16. Two flat cleaved single mode fibres (SMF600) are used along with a 635 nm handheld laser source and a spectrometer to make a 15 ° angle with chip respectively. Two cameras are used to find the location of two optical fibres. One is on the top of two fibres and vertical to them to observe the location of fibres on sample, and another is located at a horizontal direction to observe the distance between fibres and sample.

This initial set up was used to test the first sample from University of Bath described in section 4.3. There are many gratings with different distances on this sample, and there

is no waveguide between the gratings. This measurement was used to observe the feasibility of grating coupling at wavelength near 635 nm.

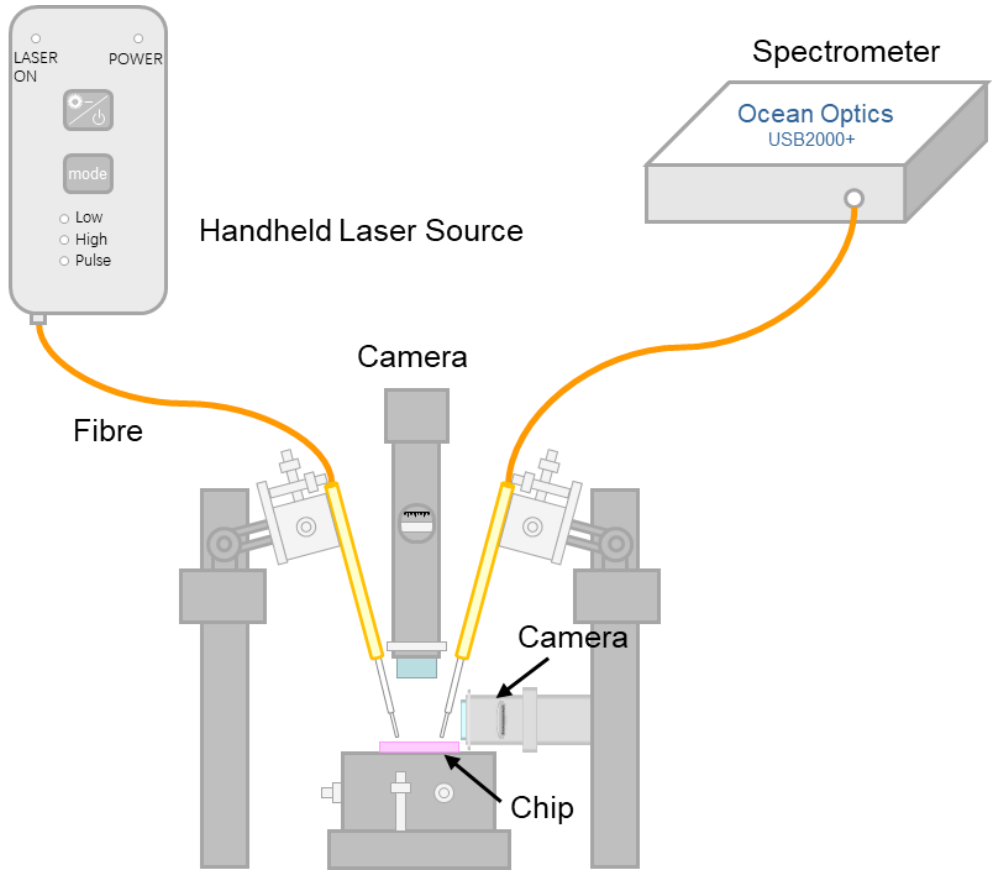

Figure 3.15 Schematic drawing of initial measurement set up constitution.

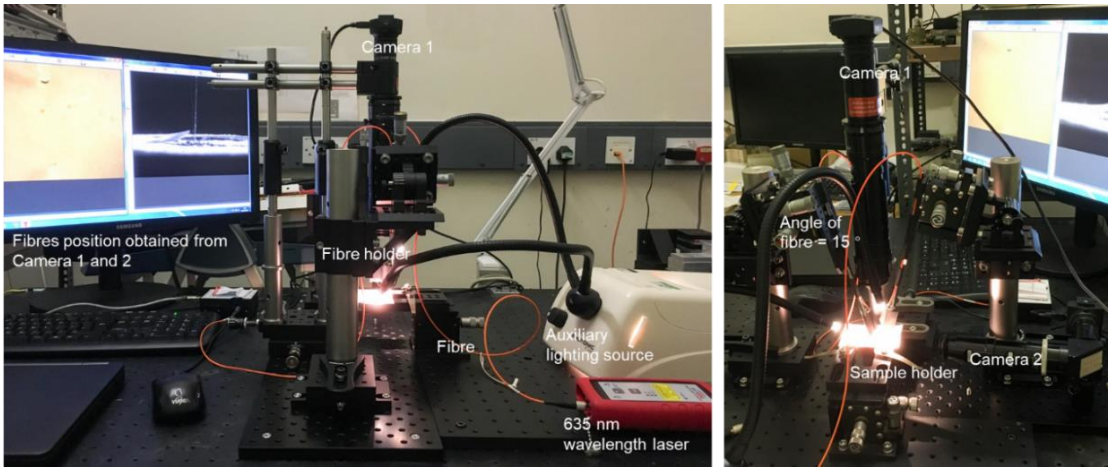

Figure 3.16 Initial measurement set up pictures.

After getting some coupling results, we gradually upgraded the set up to measure subsequent samples. The improvement includes:

1. Light source. The original laser emitted a narrow-band light source with a typical central wavelength of 635 nm. This light source did not satisfy our need to observe a wider spectrum, so we upgraded the light source to a supercontinuum laser.
2. Free-space. Two XYZ translation mounts were added to couple the source from laser into free-space, then into the single mode input fibre. This prevents possible fibre facet damage through using direct couplers.
3. Fibre holders. There was too much weight and flex in the initial fibre holders causing instability. The adjustment on the X, Y and Z micrometre drivers on the fibre holder was too coarse, so could not easily position the fibre to find the best result. We redesigned the fibre holders and fabricated more stable solid aluminium blocks with angles faces to replace the original pillars. In the new fibre holders, we use the fibre chucks fixed optical fibres, and update the XYZ translation mounts.

The final optical testing was performed using the measurement setup shown in Figure 3.17 and Figure 3.18. The chip is placed on a XYZ translation stage. Two single mode optical fibres (SMF600) are mounted at an angle of 15 ° which couple light into and out of the chip. A SuperK COMPACT supercontinuum laser delivers the unpolarised light to the input fibre. To avoid the possibility that direct coupling damages the fibre facet, two achromatic objectives are added to couple from laser into free-space, then into the fibre. An Ocean Optics spectrometer (USB 2000+) is used to collect in-out coupling intensity data. A high-magnification camera is used to show a plan-view and the location of fibres on the sample. The second camera shows a side-view to check the vertical distance between the fibre facets and sample.

This device is used to measure other samples which are introduced in section 4.3, and It will obtain coupling results in TE or TM mode by adding a linear polariser to the free-space in the future.

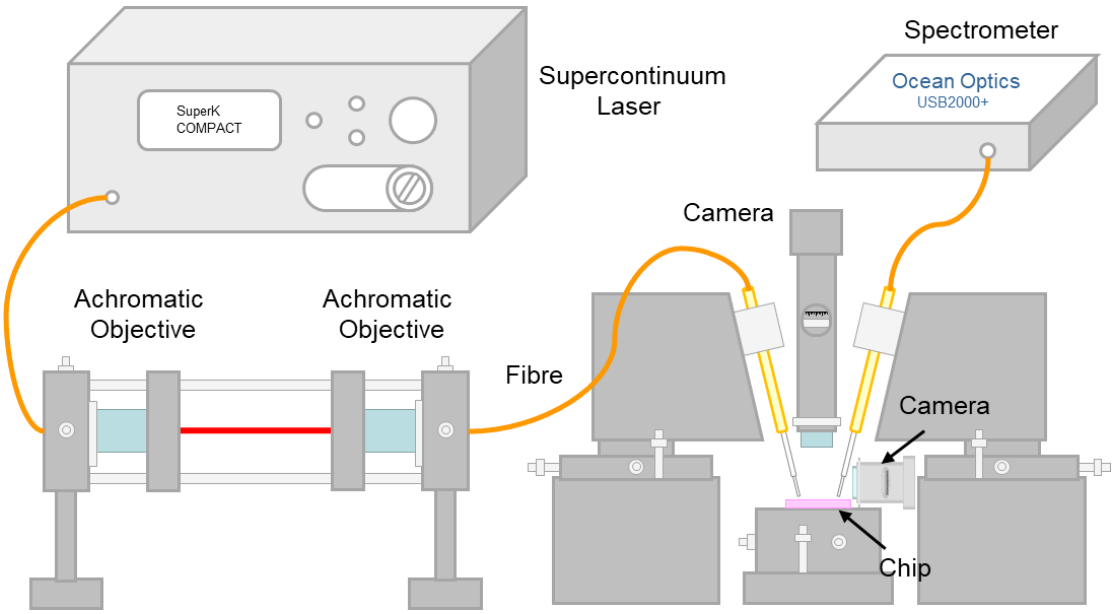

Figure 3.17 Final fibre based measurement set up which includes a supercontinuum laser, two achromatic objectives, two single mode fibres, chip, detector and two cameras.

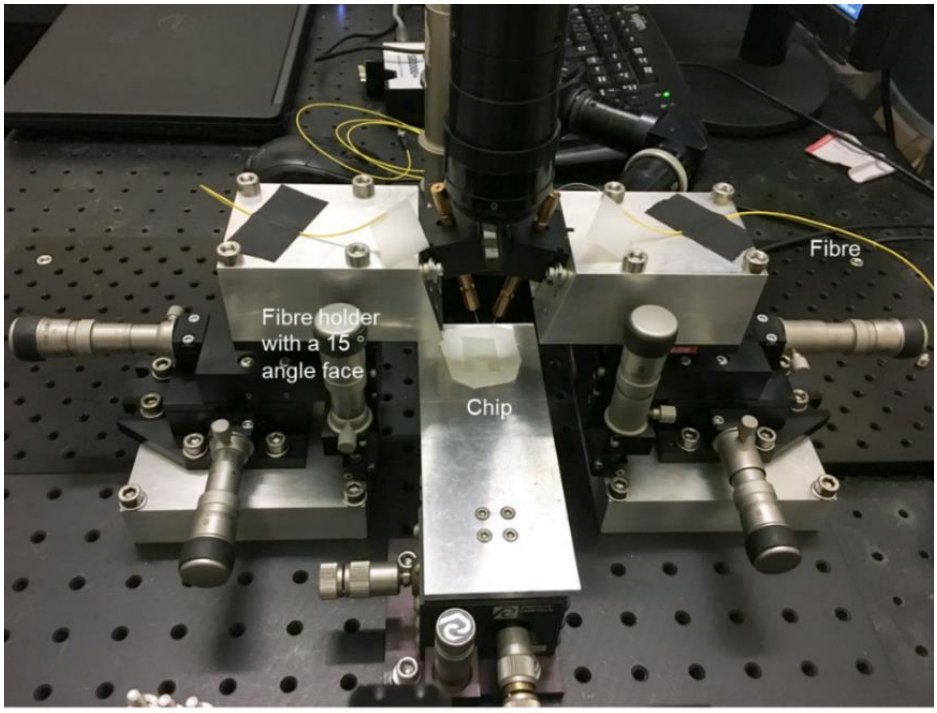

(a)

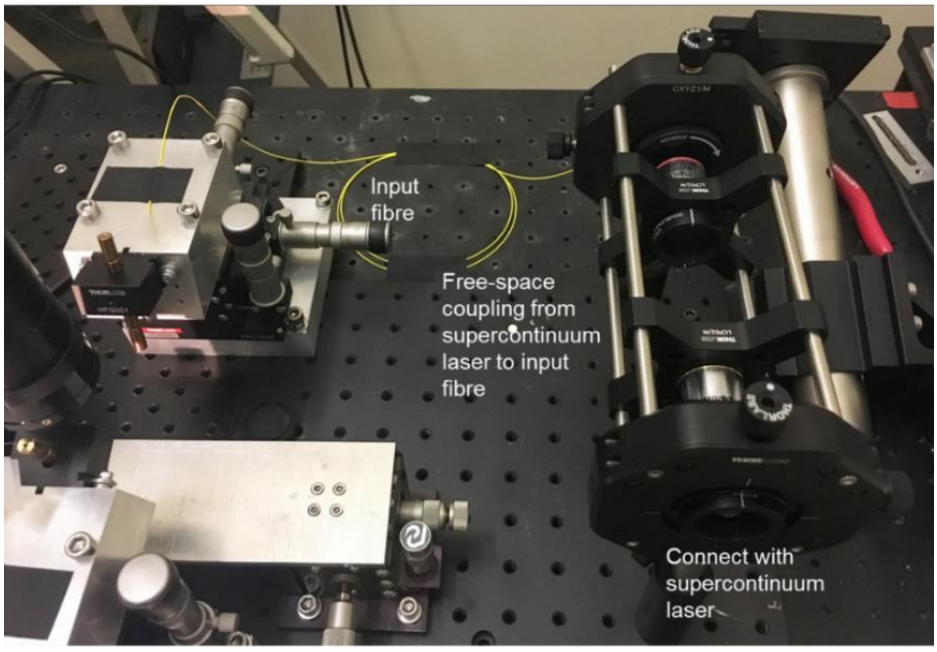

(b)

Figure 3.18 Final fibre based measurement set up pictures: (a) in-out coupling part; (b) free space coupling part.

3.5 Fabrication

There are many lithography techniques used to fabricate periodic micro-nanostructures, such as Electron beam lithography and DTL. Electron beam lithography is a technique that uses electron beams to directly produce patterns in a photoresist. DTL is a new photolithography technique. The Talbot effect mainly occurs on periodic objects (masks) illuminated by monochromatic collimated light. For the linear structure, the self-image is generated with $\frac{2p^2}{\lambda}$ as the period, where p is the mask period and λ is the wavelength of the incident light. When the mask is irradiated by uniform plane wave, it can accurately present a pattern whose frequency is twice that of the mask periodic frequency on the surface, so as to achieve high resolution periodic pattern lithography. Figure 3.19 shows the principle diagram of Talbot self-imaging lithography [177].

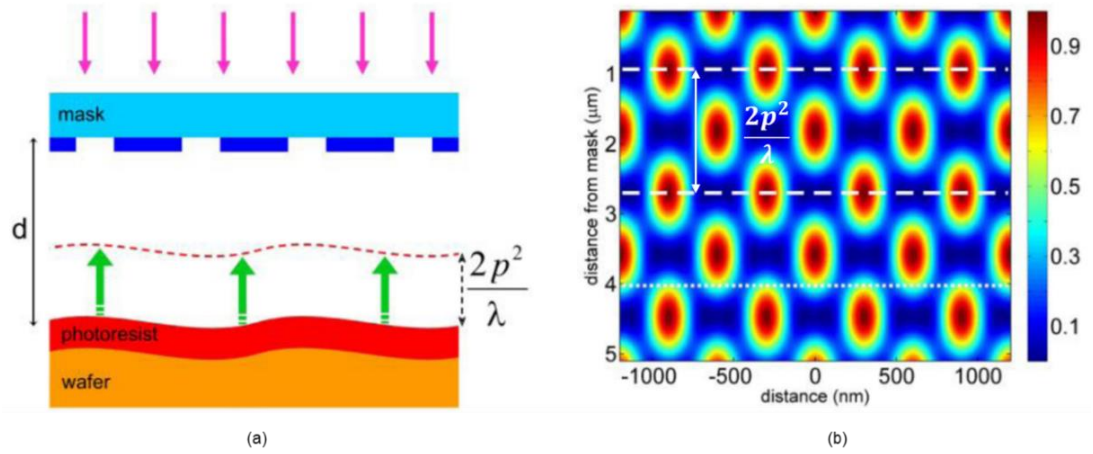

Figure 3.19 (a) The photoresist moves towards the mask during exposure, within one Talbot period; (b) After the linear grating mask, a pattern whose frequency is twice that of the mask periodic frequency is shown in Intensity distribution [177].

The fabrication of GaN waveguides and PhC cavities is almost always based on electron beam lithography. Although the accuracy of this method is very high, the manufacturing process is slow and is very expensive. This work aims to design a waveguide integrated

GaN DBR cavity using the DTL technique, which can produce large area, nanoscale periodic structures with low-cost and high-throughput [178, 179]. The chips using the DTL technique introduced in chapters 4 and 5 are fabricated by University of Bath.

3.6 Summary

This chapter introduces the various methods required in the following chapters. Here the Lumerical FDTD as simulation software will be used to optimise the parameters of the sensor design, and the experimental set up will be used to measure the in-out coupling intensity of the sample, and the lithography techniques will be used for the fabrication of the chips.

In addition, I described some simple simulation examples. Through those examples, the simulation results are compared with the theoretical calculation, and a good agreement is obtained. This guarantees the correctness of the simulation of complex structures in chapters 4 and 5.

4 Grating couplers design and results

4.1 Introduction

The chapters 2 and 3 introduce the principle of grating coupler, the FDTD software used for simulation, the similarity between simulation and theoretical results for single mode waveguide, and some fabrication overview.

In this chapter, we will introduce the design process for our grating couplers, including the setting of various parameters, as well as the experimental results of designed samples. This chapter is based on our published paper [151]. Based on the early red laser source and GaN sample, we chosen to study the coupling efficiency on a thickness of 1.5 μm GaN on sapphire platform with a wavelength range of 630-640 nm.

We used FDTD simulation to find the optimal transmittance at a 15 ° incident angle and a 400 nm grating period by varying the filling factor and etch depth. Then the chips are fabricated according to the parameters obtained by simulation. Two chips are introduced in this chapter. The first chip has a number of gratings with different spacing, and no waveguide is fabricated between the gratings. We used the narrow-band red

laser with an output wavelength of 635nm to test the in-out coupling between two gratings, and obtained the graph of insertion loss, which verified the feasibility of the GaN-on-sapphire waveguide grating. The second chip was fabricated according to the simulated optimisation parameters, but the actual sample parameters were slightly different from the optimised simulation parameters due to the fabrication differences. We carried out the simulation according to the actual sample parameters and compared the experimental measurement results. A good consistency was obtained between the modelling and measurement. Moreover, the insertion loss graph shows that the waveguide loss can be reduced by adding the fabrication of waveguides between gratings.

4.2 Simulation methods and modelling results: Finite difference time domain

We used the two-dimensional FDTD technique from Lumerical FDTD Solutions [170] to optimise the maximum out coupled power for a 1.5 μm layer of GaN-on-sapphire. Figure 4.1 (a) shows the 2D schematic cross-section for the input grating structure and Figure 4.1 (b) shows the in-out grating coupler structure.

In the model, a fundamental TE mode source comes from a fibre which is single mode around the wavelength of interest which is 630-640 nm. This was initially based on the fact that a 635 nm wavelength red laser would be used to show simple light coupling, this was eventually replaced with a supercontinuum laser source. Thus the fibre is a SMF600 with 125 μm cladding diameter and 4.3 μm core diameter. Based on the theory in the section 2.2.1, light from the fibre will be diffracted into the reflected and transmitted orders. Some of the transmitted orders which satisfy the guided mode

conditions can propagate in the 120 μm long waveguide and be coupled out into free space, then collected by an identical single mode fibre at the output. The simulation uses a wavelength range of 450-900 nm and is mainly focused on optimising across the 630-640 nm wavelength range. The gratings and waveguide are in the GaN layer with a refractive index n_{GaN}= 2.38 [148]. The substrate is sapphire with a refractive index $n_{Sapphire}$= 1.77 [149], and the cover region is air.

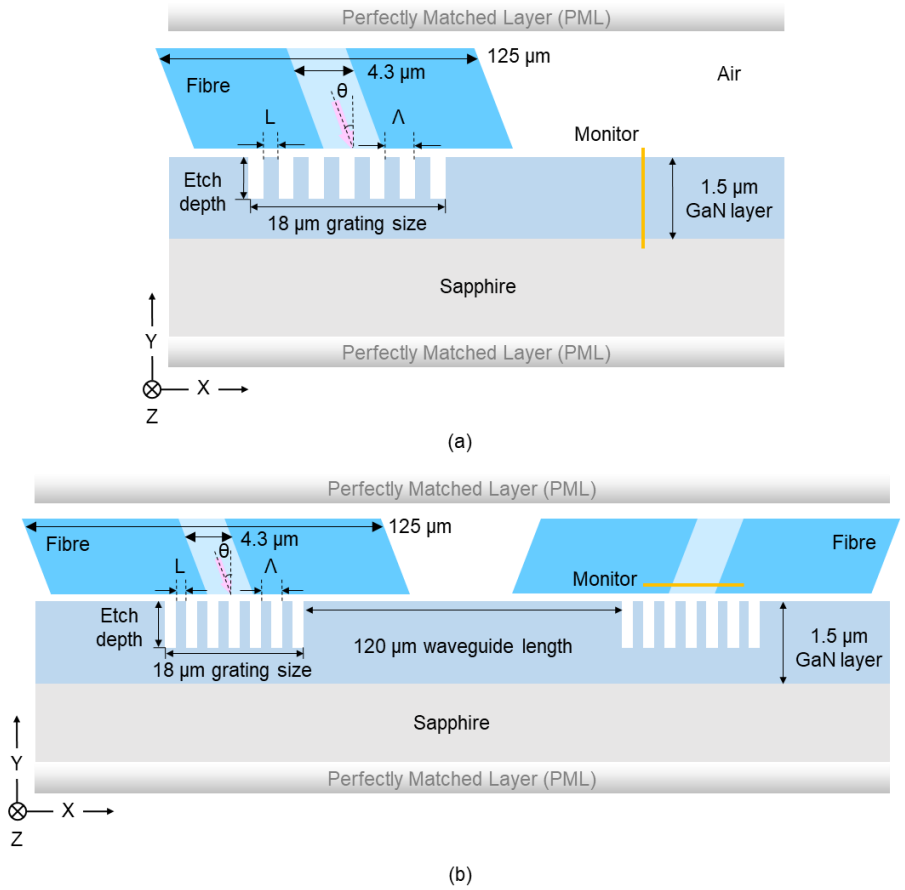

Figure 4.1 Geometry of 1.5 μm GaN on sapphire structure. Device parameters: n_{GaN} = 2.38, $n_{sapphire}$ = 1.77, grating period = Λ = 400 nm, filling factor = a = L/Λ, grating length = 18 μm, number of periods = 45, waveguide length = 120 μm, angle of fibre = 15 °. (a) input grating; (b) in-out grating couplers.

There are four main design parameters for the grating couplers: grating period, filling factor, etch depth and number of periods, where grating period *Λ* and filling factor *a* =

L/Λ. In addition, the fibre angle of incidence plays an important role. In our case, this was fixed at 15 ° based on the available optical measurement set up. The main design choice to be made is the grating period and diffraction theory can be used to determine the optimum value and this is simplest when the waveguide is single mode [172]. However, in our case the GaN slab waveguide is highly multimode, supporting 8 TE modes around 630-640 nm wavelength, which is shown in Figure 4.2.

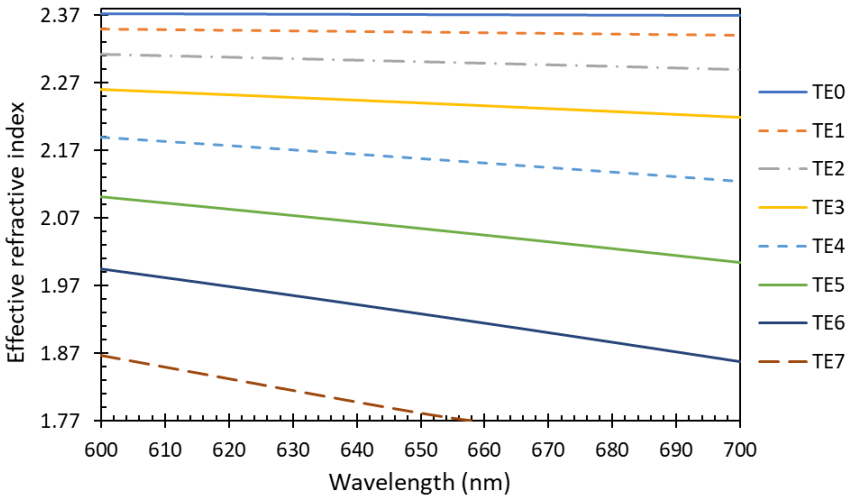

Figure 4.2 1D mode solver-effective index vs. thickness of waveguide.

Thus in our case, we based our choice on available DTL masks. The grating period could be 400 nm or 500 nm. According to equation 3.10, the ratio of wavelength to period needs to be satisfied

$$1.77 \leq n_{air} \sin 15\,^{\circ} + q\frac{\lambda}{\Lambda} \leq 2.38 \qquad 4.1$$

The period of 500 nm does not satisfy the above equation, so we decided on a 400 nm period grating.

FDTD modelling was then used to determine the impact of etch depth and filling factor in order to guide the fabrication process. The number of periods was chosen as 45 giving

a grating length of 18 µm which was felt to be sufficiently large with respect to the fibre core diameter of 4.3 µm. Figure 4.3 shows some input grating modelling results with varying etch depth and filling factor.

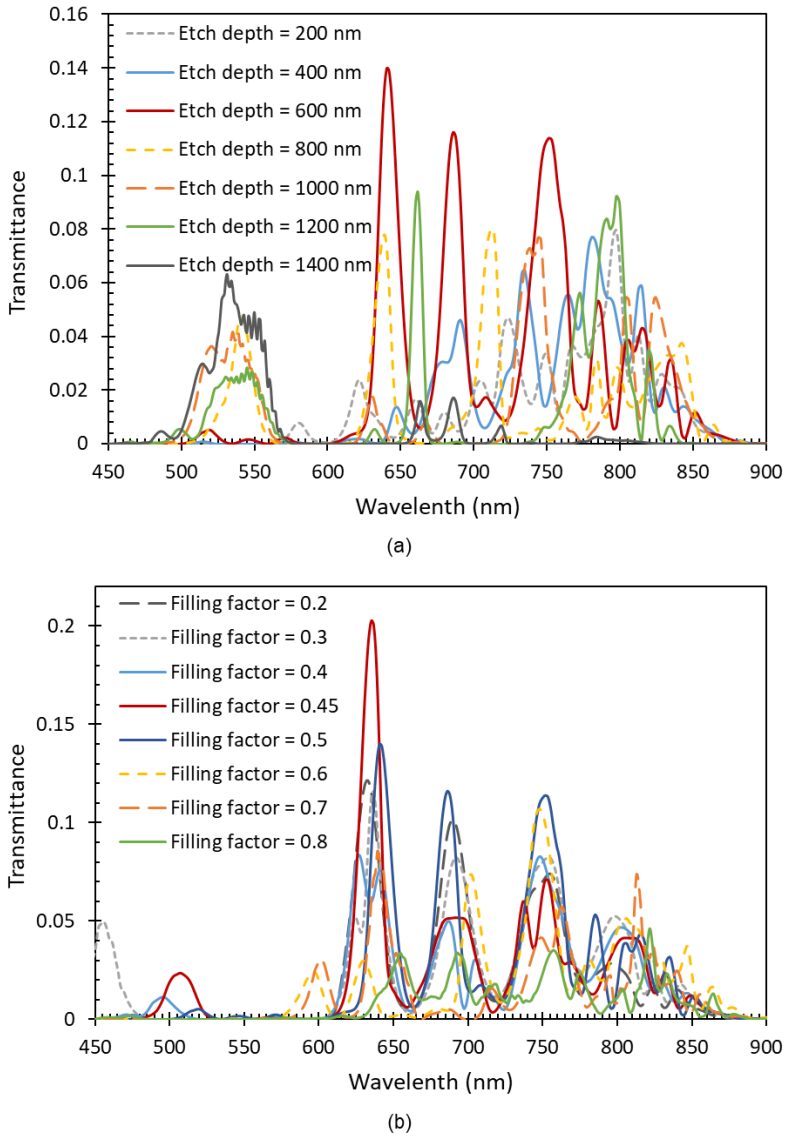

Figure 4.3 2D FDTD modelling transmittance result for input coupling with varying filling factor and etch depth: (a) angle of fibre = 15 °, grating period = 400 nm, filling factor = 0.5; (b) angle of fibre = 15 °, grating period = 400 nm, etch depth = 600 nm.

In the FDTD modelling, by varying the etch depth ranging from 0 to 1500 nm and filling factor from 0.2 to 0.8, it was found that the TE_0 mode input source has an

optimum transmittance around 630-640 nm wavelength when the filling factor is 0.45 and the etch depth is 600 nm. According to the reciprocity of input coupling and output coupling mentioned in the section 3.3.1, the in-out transmittance around 630-640 nm wavelength is also the best by using these parameters. Here, a waveguide length of 120 µm was chosen as a balance between simulation memory requirements and obtaining realistic results for waveguides that would be much longer in practice. Figure 4.4 shows the in-out transmittance spectra for the TE_0 mode, TM_0 mode and TE_0+ TM_0 modes sources with these parameters. It can be seen that the TE_0 mode has high transmission and the TM_0 mode has very low transmission. This would allow us to use unpolarised light at the input and restrict the waveguide and cavity design to TE modes only. In the TE_0 case, a number of peaks in transmittance are obtained in four distinct wavelength regions: 610-660, 660-720, 720-780 and 780-850 nm. Here, the best transmittance is 0.109 or -9.65 dB at 634.5 nm wavelength. The linewidth for this peak is about 10.5 nm. The transmittance of TM_0 mode is almost zero, especially near the wavelength of 630-640 nm. In order to model the transmission of unpolarised light we can sum the TE_0 and TM_0 results as shown in the Figure 4.4.

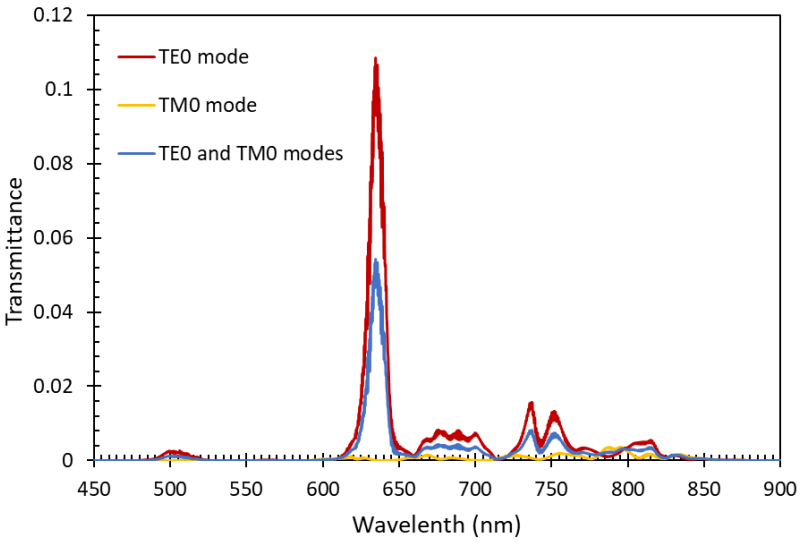

Figure 4.4 2D FDTD modelling transmittance result for in-out coupling at 15 ° angle of incidence. Device parameters: n_{GaN} = 2.38, $n_{sapphire}$ = 1.77, waveguide length = 120 μm, grating length = 18 μm, grating period = 400 nm, filling factor = 0.45, etch depth = 600 nm.

In the input coupling modelling, the transmittance of each mode at the monitor location can be obtained through the FDTD's mode profiles functionality, which is shown in Figure 4.5. Here, the total transmittance is the sum of the transmittance of all modes. Corresponding to the wavelength ranges of the four peaks of in-out coupling transmittance obtained above, Figure 4.5 can be zoom-in to these four ranges to obtain Figure 4.6.

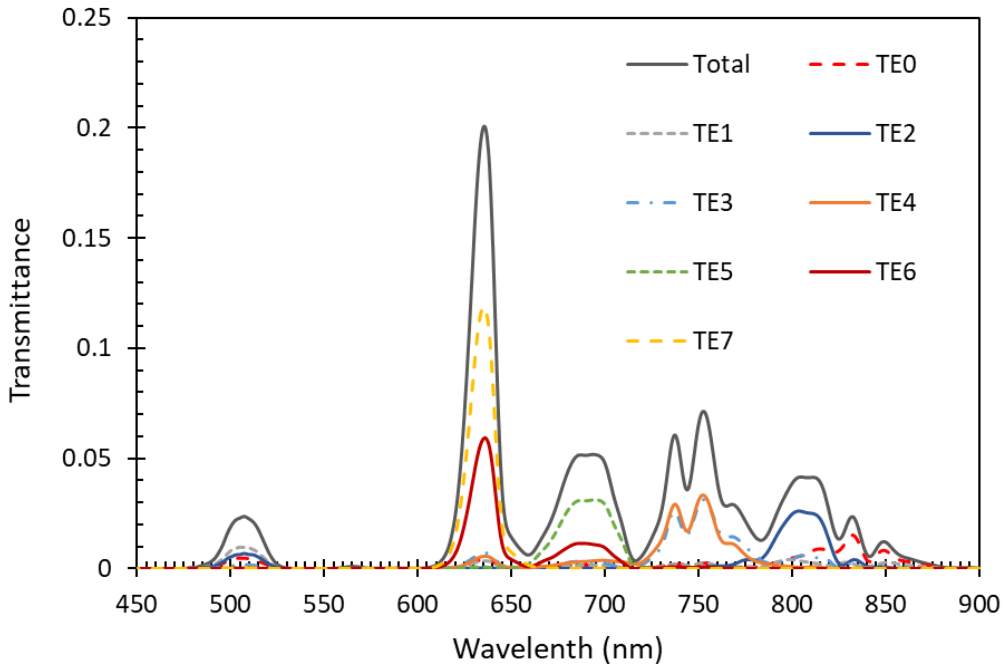

Figure 4.5 2D FDTD modelling mode profiles result for input coupling at 15 ° angle of incidence. Device parameters: n_{GaN} = 2.38, $n_{sapphire}$ = 1.77, grating length = 18 μm, grating period = 400 nm, filling factor = 0.45, etch depth = 600 nm.

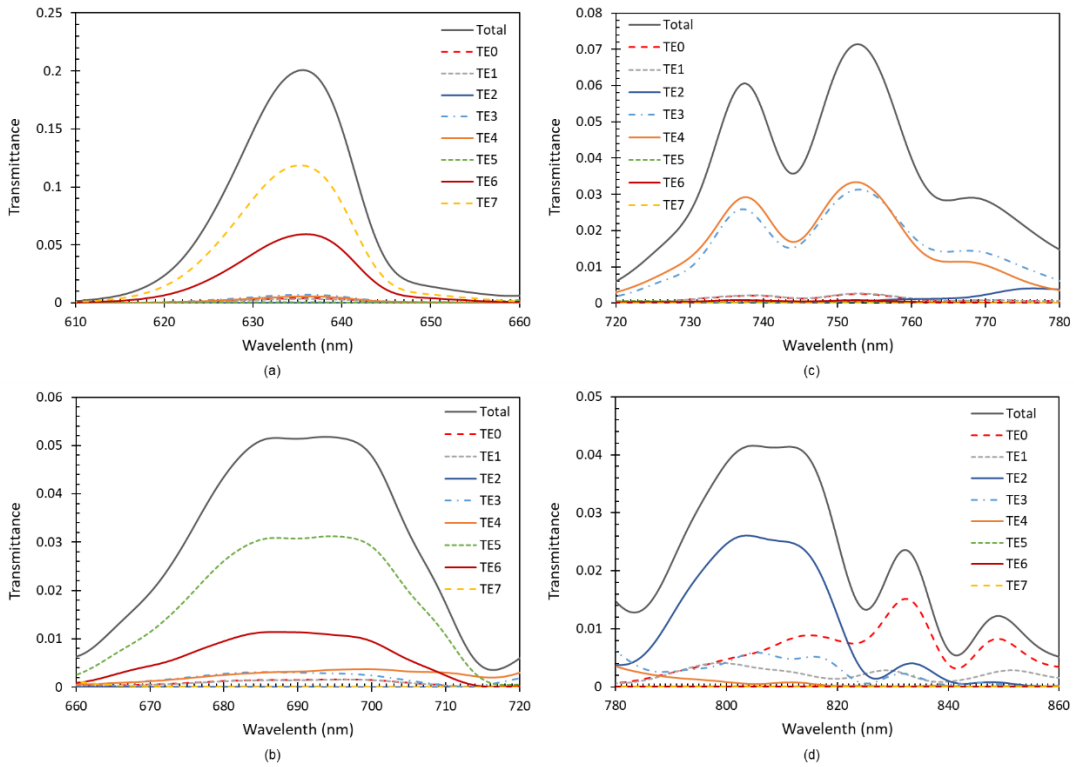

Figure 4.6 Zoom-in of input coupling mode profiles result for each peak wavelength region: (a) 610-660 nm wavelength range; (b) 660-720 nm wavelength range; (c) 720-780 nm wavelength range; (d) 780-860 nm wavelength range.

As can be seen from Figure 4.6, the transmission peak near the 640 nm wavelength is mainly composed of TE_6 and TE_7; The transmission peak near the 690 nm wavelength is mainly composed of TE_5 and TE_6; The transmission peak near the 750 nm wavelength is mainly composed of TE_3 and TE_4; The transmission peak near the wavelength of 800 nm is mainly TE_2; The transmission peak near the wavelength of 830 nm is mainly composed of TE_0 and TE_1. According to equation 3.10, effective refractive index of guided wave corresponding to different wavelength can be calculated under the condition of incident angle of 15 ° and grating period of 400 nm. By comparing the effective refractive index of the different modes at these wavelengths calculated by 1D mode solver [172], the mode component of each peak can be theoretically analysed. The table below shows the specific data, which is similar to the simulation results.

Wavelength	Incident angle	Grating period	n_{eff}-equation	n_{eff}-mode solver
640 nm	15 °	400 nm	1.8588	1.9422 (TE_6) 1.7983 (TE_7)
690 nm	15 °	400 nm	1.9838	2.0149 (TE_5) 1.8725 (TE_6)
750nm	15 °	400 nm	2.1338	2.1965 (TE_3) 2.0881 (TE_4)
800 nm	15 °	400 nm	2.2588	2.2652 (TE_2)
830 nm	15 °	400 nm	2.3338	2.3666 (TE_0) 2.3260 (TE_1)

Table 4.1 Theory calculation for mode component of each peak wavelength.

4.3 Measurement results

This section presents measurement results of the samples which have been fabricated at University of Bath for a series of couplers in the GaN-on-sapphire platform. A two-stage lithography process combining DTL and DLW has been used to define the 400 nm period grating couplers. This novel lithography technique allows nanoscale patterning on a wafer scale. The grating patterns were transferred into SiNx which was used as a hard mask for subsequent etching into the GaN.

4.3.1 Coupling between two gratings

The first sample from University of Bath is a series of gratings. The sample's picture and layout are shown in Figure 4.7. On this chip, there is no waveguide between the grating and the grating, and the distance between the two gratings is from 1 mm to 7 mm (in step of 1 mm). Figure 4.8 shows scanning electron microscopy (SEM) pictures of one grating on the chip. The grating period is about 390 nm and the filling factor is seen to be close to 0.53. The etching depth was estimated at 750 nm.

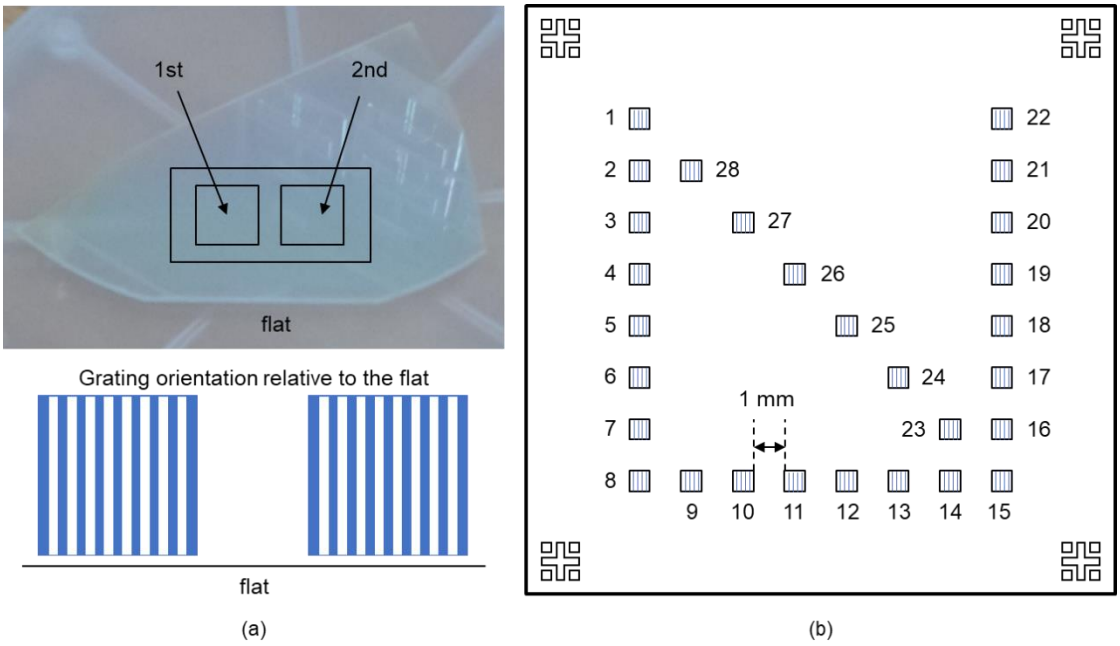

Figure 4.7 Chip of 1.5 μm thick GaN-on-sapphire grating couplers (no waveguide) with 400 nm period: (a) Chip photo and schematic diagram of grating direction; (b) The mask layout of one area.

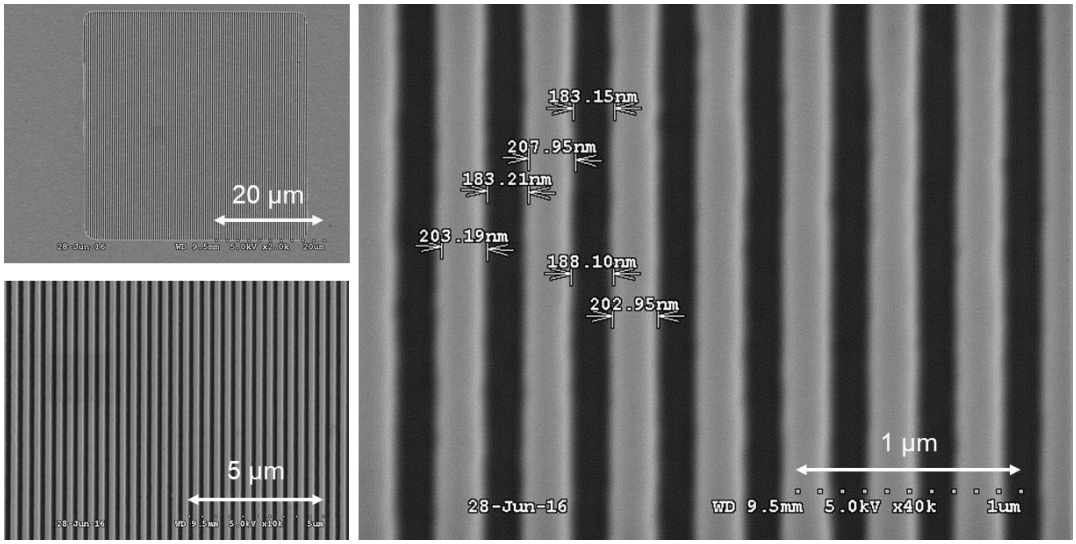

Figure 4.8 SEM pictures of one of grating on the chip.

The measurement set up used the initial set up described in Figure 3.12 and Figure 3.13. Flat cleaved single mode fibres (SMF600) are used along with a 635 nm laser source and a spectrometer. We use a silver mirror to measure its reflection intensity as the original input intensity. The mirror reflection picture and optical micrograph of in-out coupling are depicted in Figure 4.9. Figure 4.10 (a) plot the in-out coupling measurement results with varying distances between two gratings and Figure 4.10 (b) shows the insertion loss measured relative to a silver mirror for a series of grating couplers where the distance between the couplers is increased in steps of 1 mm. The trend line reveals the propagation loss to be 4.2 dB/mm and, from its intercept, a total coupling loss of 5.6 dB or 2.8 dB per coupler. These results proved the feasibility of coupled grating for GaN on sapphire platform. These couplers and the GaN waveguide layer structure have yet to be optimised for integrated photonics applications. The next section will introduce the GaN grating couplers chip based on the optimisation simulation results in section 4.2.

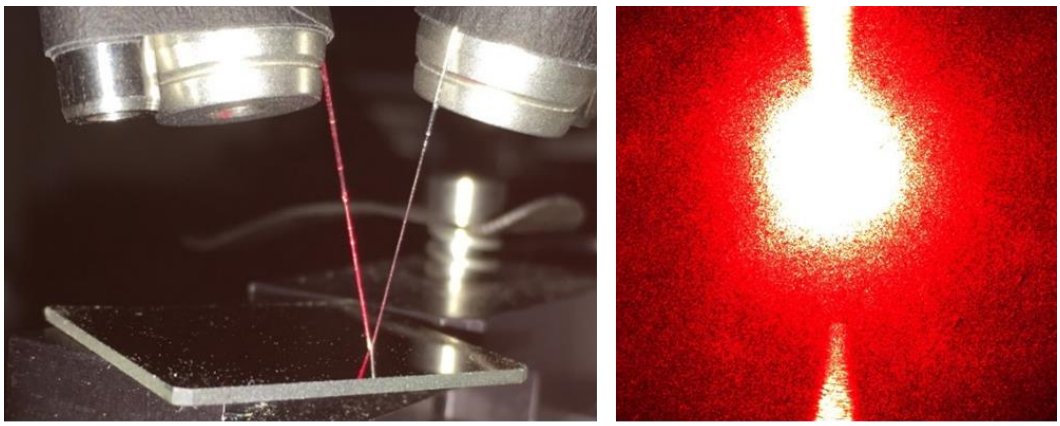

(a) (b)

Figure 4.9 Fibre based measurement set up picture: (a) measured the mirror reflection; (b) in-out coupling image from camera 1.

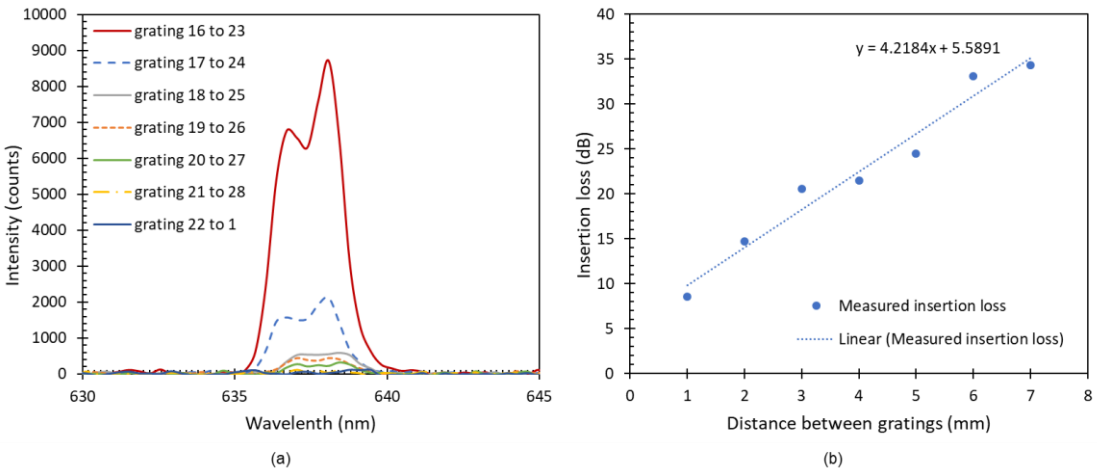

Figure 4.10 Measured in-out coupling results: (a) Measured in-out coupling in two grating with varying distance; (b) Insertion loss for a series of grating couplers.

4.3.2 Grating couplers with waveguide

The second chip from University of Bath contains regions of grating couplers and regions of grating couplers with DBR cavities. The cavity region is described in the experimental section of the next chapter.

The specific fabrication process is based on a paragraph contributed by University of Bath in our published paper [135]. The fabrication process employed only a single GaN etch step using a 450 nm-thick plasma-enhanced chemical vapor deposition with a SiNx hard etch mask. This meant that multiple lithography steps were required to pattern the SiNx mask beforehand. This is due to the different capabilities of the two lithography techniques: DTL can pattern periodic nanoscale features but only with large areas, whereas DLW can pattern arbitrary features > ~1 μm. Three different regions on the mask are required: large areas of SiNx to protect the waveguides, grating patterns for the couplers and the DBRs, and large unprotected areas in order to surround the waveguide.

The first step of the fabrication process was to define the large waveguide features in the mask. A S1813 positive photoresist mask was patterned via DLW (μPG 101, Heidelberg Instruments) and then transferred into the SiNx via ICP etching using CHF3 chemistry. This resist was then removed before applying a second, 350 nm thick, high-resolution, AZ15NXT negative photoresist layer (on top of a Wide 8C bottom anti-reflective coating to improve resolution). This was exposed via DTL (PhableR 100C, EULITHA) to create a 400 nm pitch grating in the resist across the whole sample area. A second exposure via DLW then fully exposed the negative resist in all areas where gratings were not required before CHF3 plasma was used to transfer the resist pattern into the SiNx. In this way, small grating regions could be created in the SiNx whilst the negative resist protected the surrounding sample. The resist was subsequently removed.

The resulting SiNx was used as a mask to etch ~780 nm of GaN using Cl2/Ar plasma. A high etch temperature of 150 °C was used to ensure vertical sidewall etch profiles [180]. Finally, the SiNx mask was stripped in HF-based solution.

The layout of grating couplers part of the second chip is shown in Figure 4.11. A series of 100 μm*100 μm area grating couplers with varying waveguide lengths are located in this area. All waveguides have the same width, which is 20 μm.

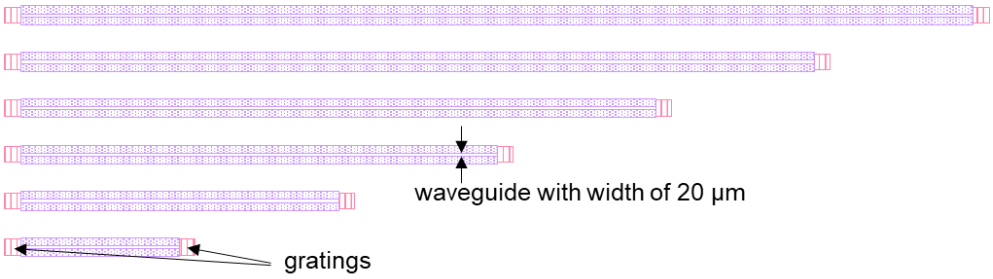

*Figure 4.11 Layout of part of the chip: grating couplers with straight waveguides. Device parameters:100 μm*100 μm grating couplers, grating period = 400 nm, waveguide width = 20 μm, waveguide length from 1 mm to 6 mm (in steps of 1 mm).*

Figure 4.12 shows scanning electron microscopy (SEM) pictures of typical grating couplers. The filling factor is shown for one grating coupler and is seen to be close to 0.5. The etch depth has been estimated to be 780 nm. Figure 4.13 shows the input coupling transmittance maps at a wavelength of 640 nm. It shows the dependence of TE_0 and TM_0 modes on etching depth and filling factor respectively. Here, the position of the red box is the best optimisation parameters mentioned in Figure 4.4, and the position of the white box is the parameters obtained with the DTL fabrication. Figure 4.14 shows the simulated in-out transmittance for TE_0 mode, TM_0 mode and TE_0+TM_0 modes sources with these parameters. The figure shows that both TE_0 mode and TM_0 mode have good transmittance around 630-640 nm wavelength with these structural parameters. This will complicate the operation of the device; in future work we will use

polarisation controllers to restrict measurement to a single polarisation, but here we will continue to use unpolarised light.

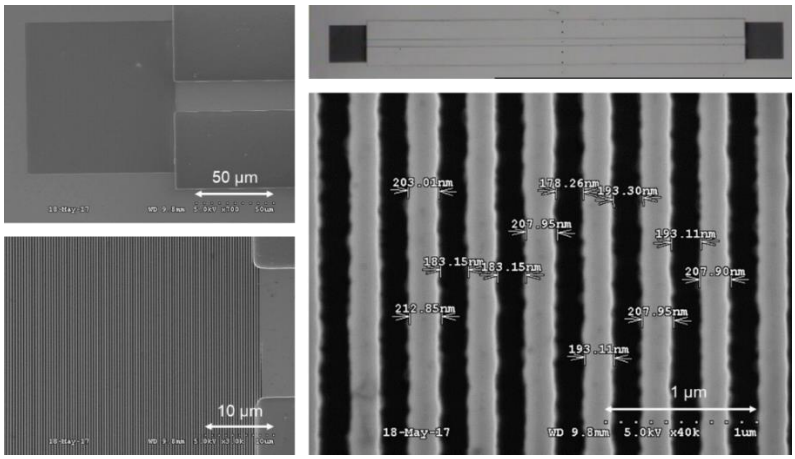

Figure 4.12 SEM images of typical grating couplers and waveguides after DTL and DLW processing.

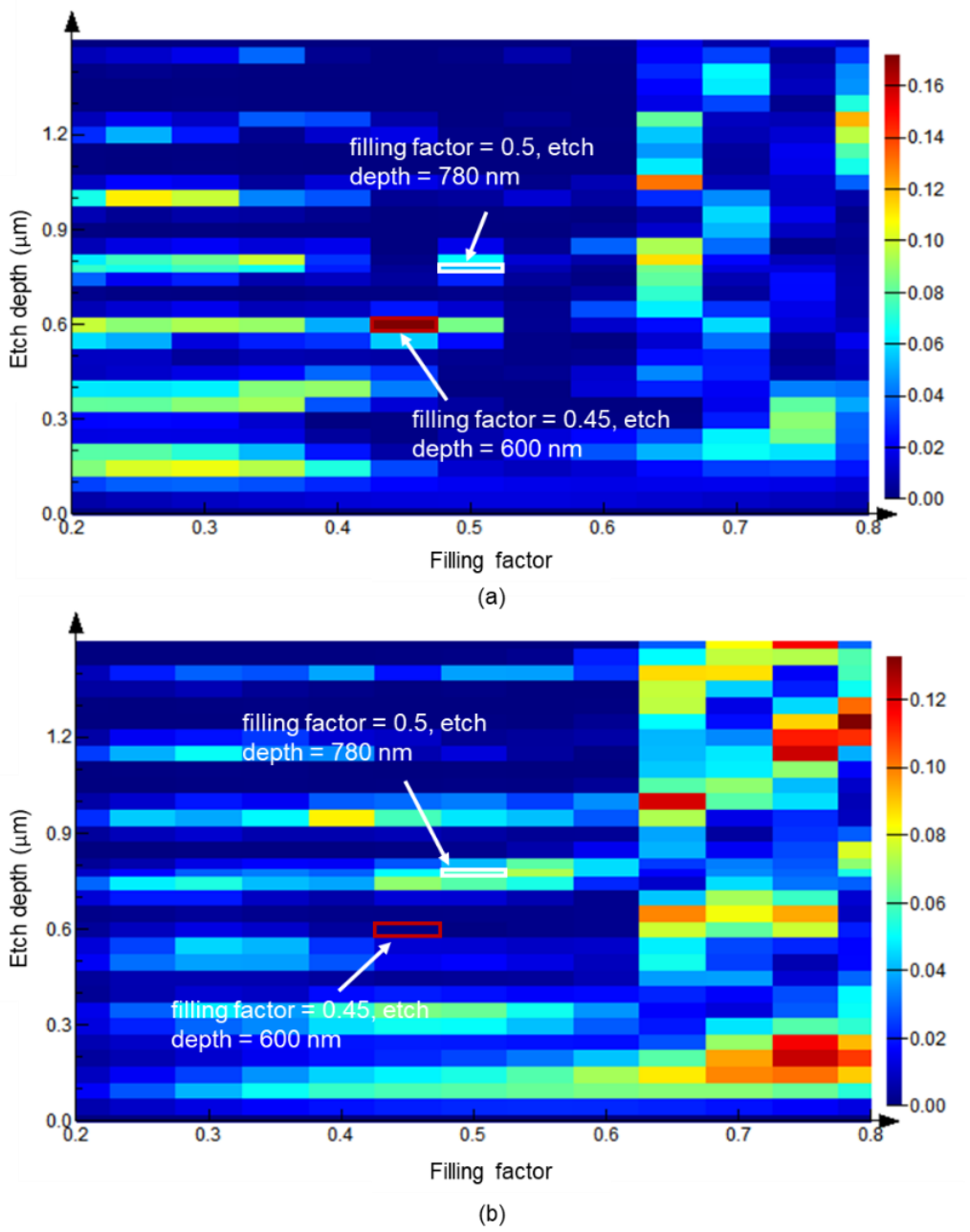

Figure 4.13 2D FDTD modelling transmittance map for input coupling at 15 ° angle of incidence with varying the filling factor (x-axis) and etch depth (y-axis). Device parameters: n_{GaN} = 2.38, $n_{sapphire}$ = 1.77, grating length = 18 µm, grating period = 400 nm. (a) TE_0 at a wavelength of 640 nm; (b) TM_0 at a wavelength of 640 nm.

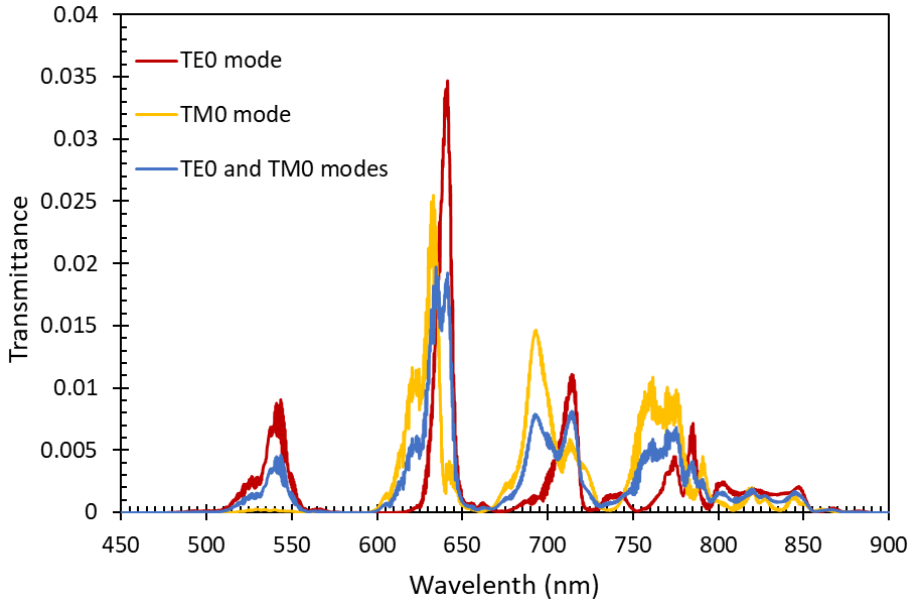

Figure 4.14 2D FDTD modelling transmittance result for in-out coupling at 15 ° angle of incidence. Device parameters: n_{GaN} = 2.38, $n_{sapphire}$ = 1.77, waveguide length = 120 µm, grating length = 18 µm, grating period = 400 nm, filling factor = 0.5, etch depth = 780 nm.

According to the above simulation results, we measured sample 2. The measurement set up used the improved set up described in Figure 3.17 and Figure 3.18. A SuperK COMPACT supercontinuum laser is used as the light source. The plan view image of GaN grating couplers and waveguide is shown in Figure 4.15 (a). The output grating can be seen to be bright in Figure 4.15 (b) when the output fibre is removed, showing that reasonable coupling has been obtained.

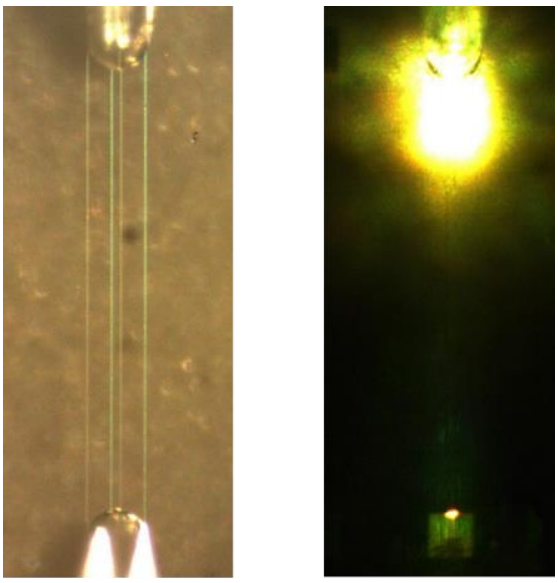

Figure 4.15 Image of grating couplers with 1 mm waveguide plan-view: (a) In-out coupling setup plan-view; (b) Output grating is bright when the output fibre is removed.

The in-out coupling measurement results with varying waveguide length are shown in Figure 4.16 (a). It can be seen that there are two regions of high transmittance around 640 and 700 nm and this matches up well with the TE_0+TM_0 mode result shown in Figure 4.14. There is some variation in the peak wavelength between the 6 waveguide lengths, but this is expected due to the fabrication differences between gratings in the different waveguides. In the case of the 1 mm waveguide there is a strong ripple with a peak spacing of 4.1 nm. It is believed that this ripple is related to mode beating [181] between the multiple modes that can propagate in the waveguide and the mode spacing is of the order that would be expected for this length of waveguide. The longer waveguides do not have such a prominent ripple, but these will have higher loss, and this will tend to suppress the mode beating effect.

The coupling loss and waveguide attenuation are estimated by the cutback method. In order to accurately calculate the coupling loss, the input fibre should be connected directly to the output to act as a reference, however in our current set up this was not

possible. Thus, in order to make an approximate estimate for coupling loss, a silver mirror placed in the position of the chip was used as a reference. This will significantly underestimate the coupling loss and in future work we will improve this coupling loss estimate. Figure 4.16 (b) shows the transmittance at 639 nm normalised to the mirror transmittance for each waveguide length. In the case of the 1 mm length, due to the strong ripple an estimate was required which removed the effect of these ripples. The slope of the linear fit gives the waveguide loss to be 3.9 dB/mm. The coupling loss, compared to the mirror transmittance, is obtained as the intercept with the vertical axis and is found to be 2 dB in total or 1 dB per coupler. Comparing with sample 1 in section 4.3.1, the coupling loss and waveguide attenuation can be reduced by optimising grating and adding waveguide structure.

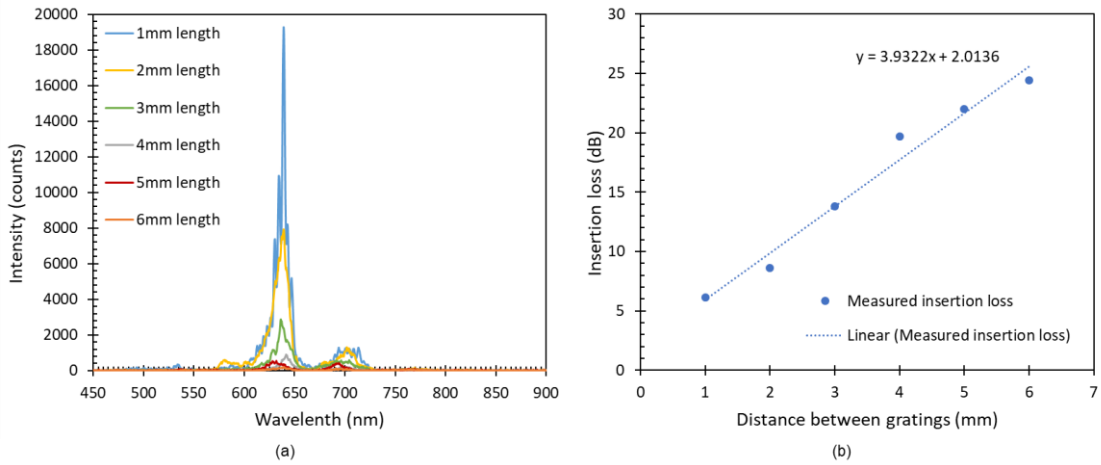

Figure 4.16 Measured in-out coupling results: (a) Measured output intensity for 20 μm width waveguide in-out coupling with varying waveguide lengths; (b) Coupling loss and waveguide attenuation estimation using the cut-back method.

4.4 Summary

This chapter introduces the design of grating coupling and the measurement results of some samples. Comparing the results of simulation and measurement, they have high similarity. However, the thick GaN waveguide layer supports multi-mode propagation, which makes the design more difficult. In addition, the limitation of DTL mask and incident angle of optical fibre also limit the selection of design parameters. These kinds of couplers and the GaN waveguide layer structure need to be further optimised for integrated photonics applications, something readily achievable with the design and fabrication technology being developed.

In the next chapter we will study how to design a Fabry-Perot cavity in the waveguide as a sensor detect different material by the changing the effective refractive index.

5 Cavities design and results

5.1 Introduction

Based on the simulation and measurement results of the grating coupler of the second chip in the previous chapter, this chapter will discuss the feasibility of adding a DBR resonant cavity in the waveguide of this structure. This chapter is based on our published paper [151]. Due to fabrication limit, all gratings on this chip maintained the same grating period, etch depth and filling factor. This leads to the grating for the 630-640 nm wavelength being a high-order Bragg grating. In addition, the multimode nature of the waveguide also increases the complexity in the resonant cavity.

5.2 Simulation methods and modelling results: Finite difference time domain

The proposed structure mentioned in section 2.4.3 is shown in Figure 5.1, which includes two GaN gratings couplers and two GaN DBR gratings forming a cavity. The

use of DTL fabrication restricts the period of all gratings to be nominally the same across the whole wafer, with laser lithography being used to define the region where the gratings are present. In future structures it may be possible to have different etch depths for different gratings, but here we have restricted processing a single etch step. These limitations are not ideal for forming both grating couplers and DBR cavities, but compared to the very high cost of electron-beam lithography, DTL + DLW is an interesting much lower cost option and this chapter shows the potential for this approach.

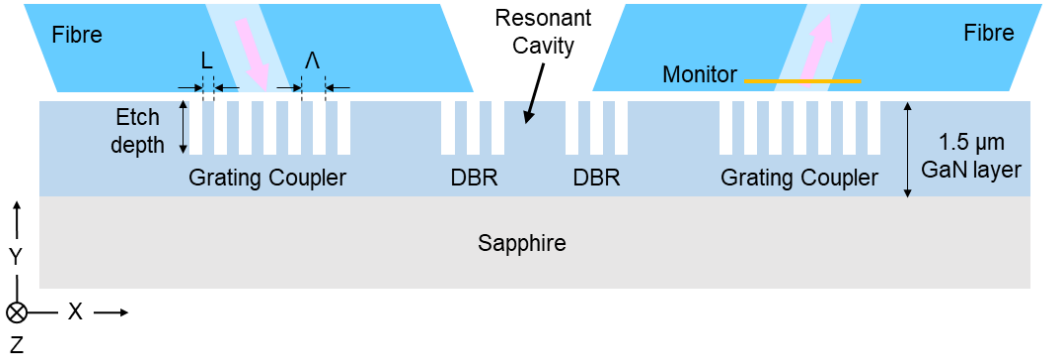

Figure 5.1 Schematic representation of proposed grating coupled DBR cavity. Device parameters: grating period = Λ = 400 nm, filling factor = L/Λ = 0.5, etch depth = 780 nm.

In this section, we focus on the DBR cavity design. As described in the previous chapter, the 1.5 µm thick GaN on sapphire platform can support higher order modes. The band structure obtained by simulating this waveguide in FDTD can also prove this. Figure 5.2 describes the TE and TM modes dispersion relation in the waveguide. Each guided mode periodically folds at the Brillouin zone edge and lie blow the sapphire light line.

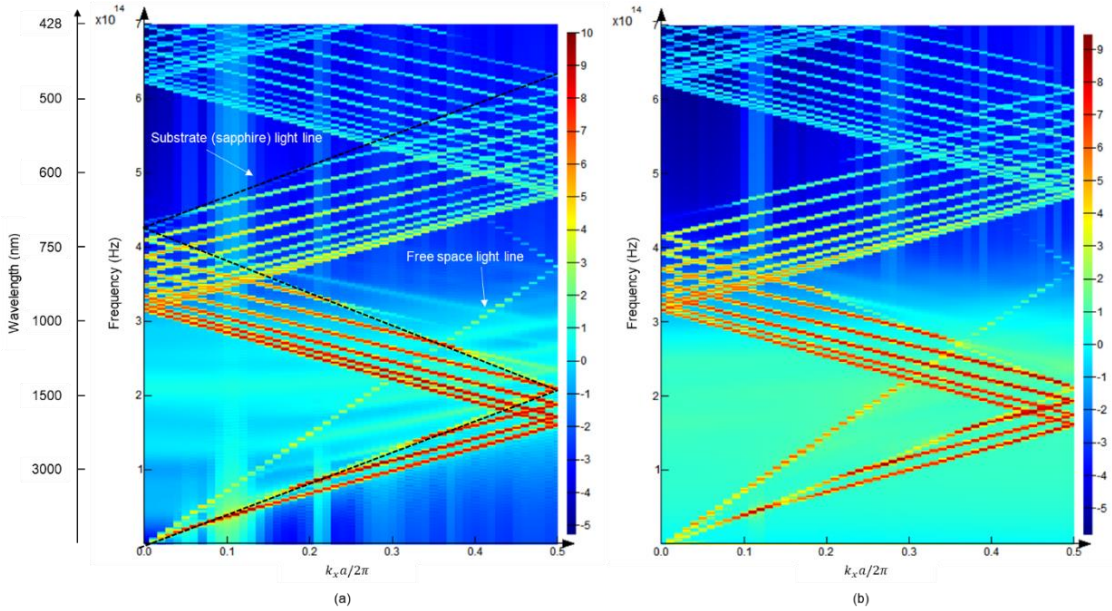

Figure 5.2 Band structure of 1.5 μm GaN on sapphire waveguide. (a) TE modes; (b) TM modes.

Due to the large number of guided modes around the wavelength of 630-640 nm, it is difficult to analyse with the basic theory introduced in section 2.4.1. Therefore, only the incident light of TE_0 and TM_0 modes are simulated. The 2D simulation scheme of a single Bragg grating is presented in Figure 5.3. The light propagates from left to right and is recorded by a monitor after 10 μm long grating. Figure 5.4 shows the modelling transmittance and reflectance with the same parameters as the coupled grating. In the stopbands, n_{eff}^{tooth} and n_{eff}^{groove} for TE_0 mode are approximately 2.3715 and 2.3479 respectively; n_{eff}^{tooth} and n_{eff}^{groove} for TM_0 mode are approximately 2.3707 and 2.3418 respectively [172]. According to the equation 2.66 of Bragg wavelength and equation 3.12 of effective refractive index, $n_{eff}^{grating}$ of TE_0 and TM_0 are very close. This leads to the stopbands for TE_0 and TM_0 described in Figure 5.4 are almost identical. Here, structure is the higher order Bragg grating for 630-640 nm wavelength.

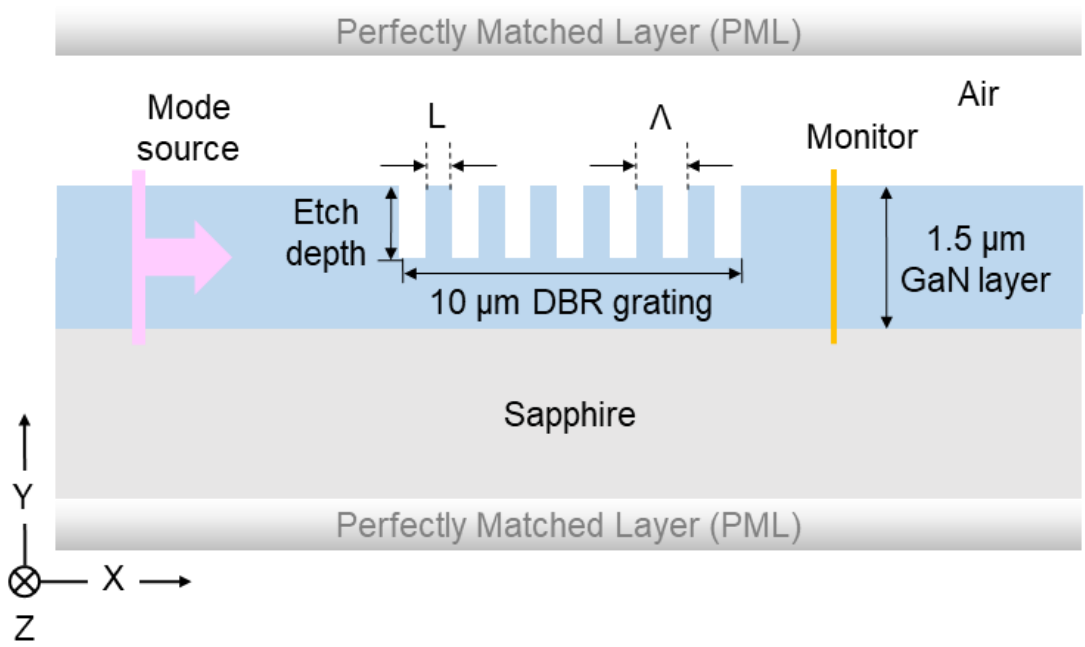

Figure 5.3 Geometry of DBR grating. Device parameters: grating period = Λ = 400 nm, filling factor = L/Λ = 0.5, etch depth = 780 nm.

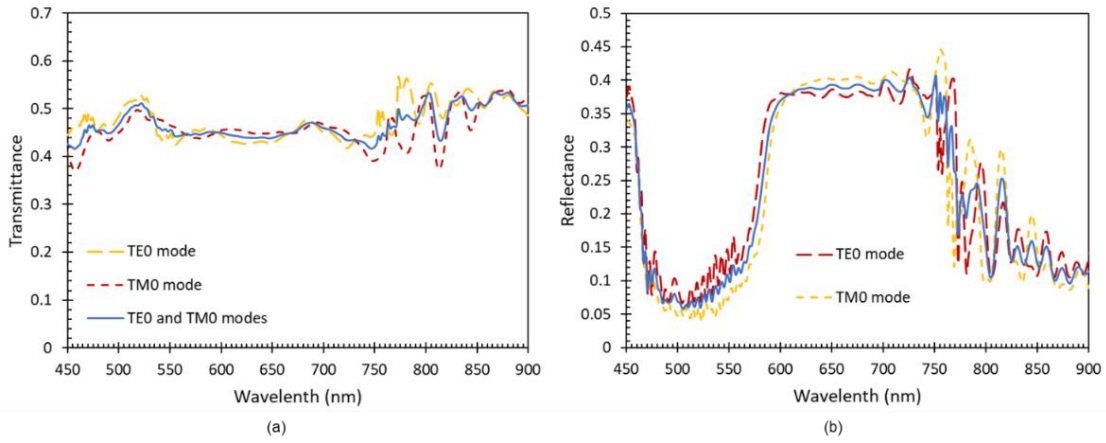

Figure 5.4 Simulated TE_0 (E_z polarised), TM_0 (H_z polarised), TE_0+TM_0 mode sources in a DBR grating with grating periods = 400 nm, etch depth = 780 nm, filling factor = 0.5. (a) transmittance spectra; (b) reflectance spectra.

We will analyse the Bragg grating with different etching depths for TE_0 mode. The transmittance of TE_0 mode source with varying the etch depth is shown in the Figure 5.5. As the etching depth increases, the n_{eff}^{groove} becomes smaller. This leads to fewer

modes can pass through the grating. This phenomenon can also be seen from the band diagram of TE_0 mode. Figure 5.6 (a) is TE_0 mode in the Bragg grating with 780 nm etch depth. Due to the moderate etch depth, there are still many modes under the sapphire light line that can propagate through the grating. When the etch depth increases and the grating structure becomes fully etched, the band diagram for this case is shown in Figure 5.6 (b). In this structure, any modes above the sapphire light line are lossy. The obvious band gaps can be seen in the band diagram. The corresponding wavelength range of the band gaps are the same as the stopbands in Figure 5.5.

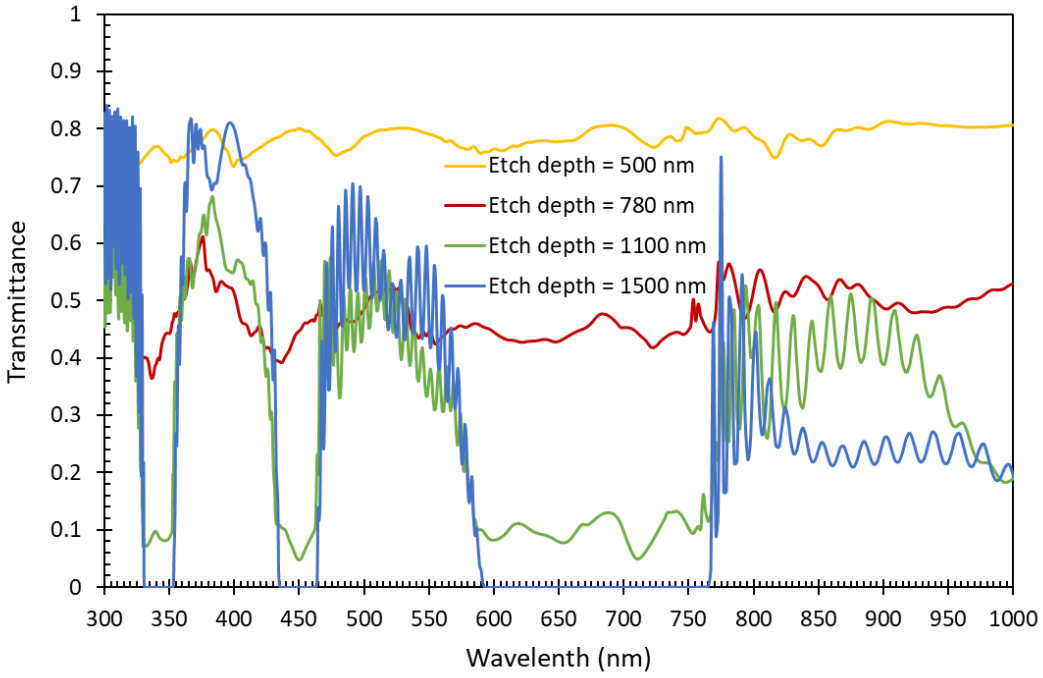

Figure 5.5 Simulated TE_0 mode source in a DBR grating with varying the etch depth, filling factor = 0.5, grating period = 400 nm.

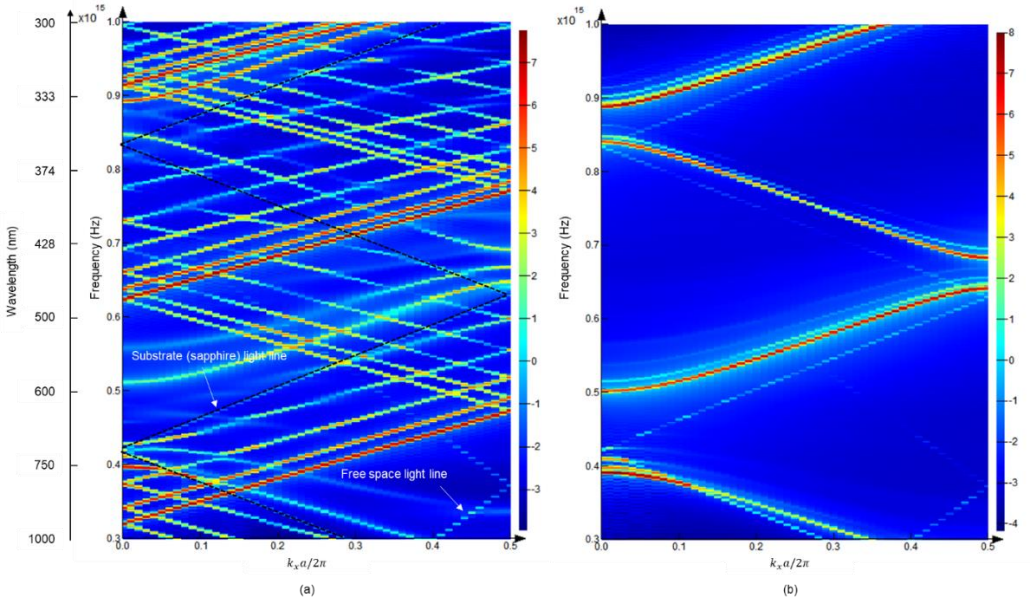

Figure 5.6 TE_0 mode Band structure of 1.5 μm GaN on sapphire based Bragg grating. Device parameters: grating period = Λ = 400 nm, filling factor = L/Λ = 0.5. (a) etch depth = 780 nm; (b) etch depth = 1500 nm.

Next, we move to the DBRs cavity design. The schematic representation of an isolated cavity is shown in Figure 5.7. It consists of two 400 nm period DBR gratings forming a cavity. As described above we represent unpolarised light with a TE_0+TM_0 mode source. The length of the cavity was chosen to be 8 μm, ensuring that there is sufficient length to observe resonant peaks, and the filling factor and etch depth remain unchanged at 0.5 and 780 nm, respectively.

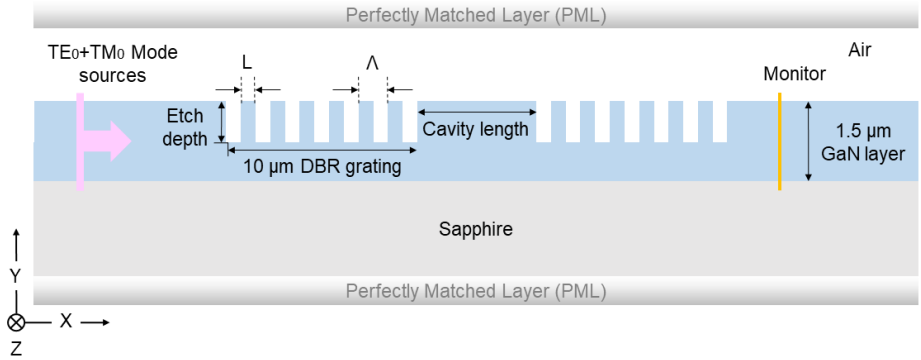

Figure 5.7 Geometry of two DBR gratings with 8 μm cavity. Device parameters: grating period = Λ = 400 nm, filling factor = L/Λ = 0.5, etch depth = 780 nm, DBR grating size = 10 μm.

The modal transmittance of Figure 5.8 is for 25 period DBR gratings with an 8 μm cavity. A mode spacing of ~10 nm can be seen at an etch depth of 780 nm around 640 nm wavelength which will allow approximately two resonant peaks to be observed in the bandwidth of the grating coupler, shown in Figure 4.16 (a). It can be seen that 780 nm etch depth is an optimum for resonant cavity behaviour. Due to the complexity of multimode waveguides, it is difficult to use simple theory to calculate mode spacing. In order to understand these effects further we can use FDTD to look at the fields at one of the resonant peaks, shown in Figure 5.9.

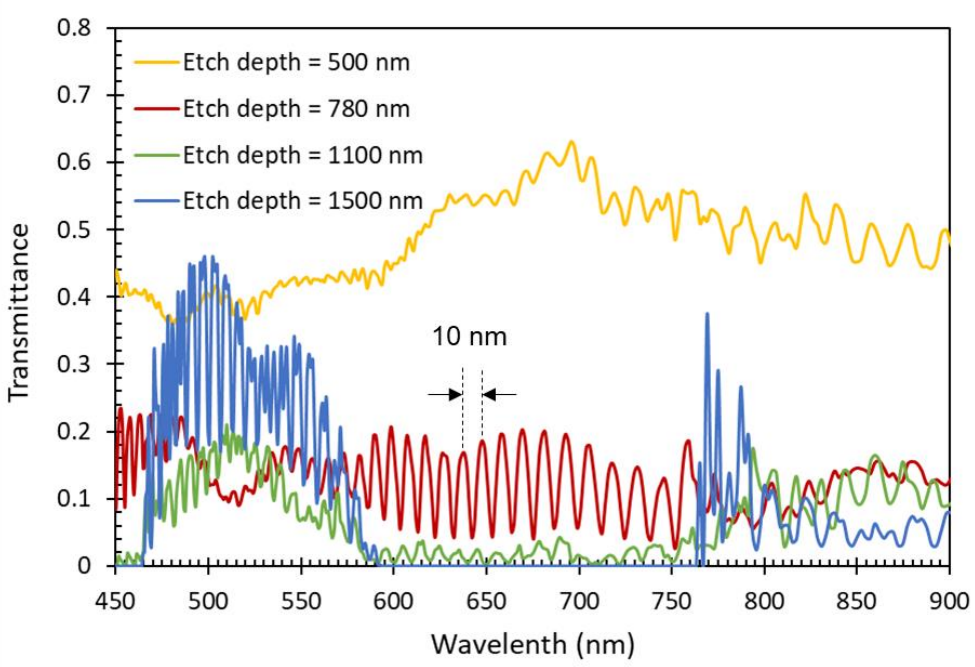

Figure 5.8 Simulated TE_0+TM_0 mode sources transmittance spectra of DBRs cavity with varying etch depth, filling factor = 0.5, cavity length = 8 μm.

Figure 5.9 show the magnitudes of the E_z field for TE_0+TM_0 modes with different etch depths at wavelength of 637 nm which is one of the resonance peaks. At 500 nm etch depth, because the structure is not fully etched, most of the light propagates in the region beneath the Bragg grating and does not couple into the cavity, so as shown in Figure 5.8, no obvious resonance peaks are observed. As the etching becomes deeper, more

light couples into the cavity and at a depth of 780 nm a significant amount of light is coupled into the cavity and this results in the resonances observed in Figure 5.8. As the etch becomes deeper, the amount of light propagating through the first DBR decreases significantly and this reduces the resonant behaviour and in the case of full etching, removes any resonances completely. It can be seen that since the waveguide is multimoded, very non-ideal operation is observed for this structure. In future work, thinner GaN layers and ridge waveguide structures will be used to ensure single mode operation which will simplify device operation significantly.

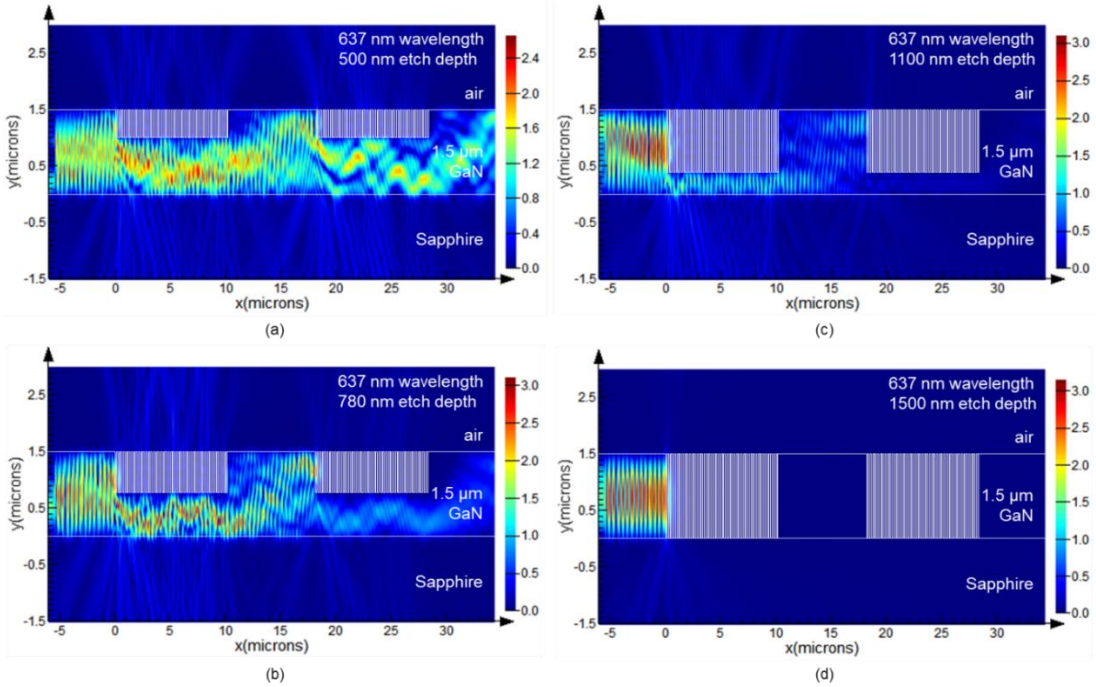

Figure 5.9 E_z field distribution in cross-section for the peak wavelength (637 nm), TE_0+TM_0 modes propagating from left to right. Grating parameters: filling factor = 0.5, grating period = 400 nm, cavity length = 8 µm. (Vertical and horizontal axes not to scale). (a) Etch depth = 500 nm; (b) Etch depth = 780 nm; (c) Etch depth = 1100 nm; (d) Etch depth = 1500 nm.

In order to observe how this cavity could operate as a refractive index sensor, the refractive index of the air area can be changed and the shift of the resonance peak wavelength can be observed. Figure 5.10 shows the transmittance curves for background refractive indices of 1, 1.05, 1.1 and 1.15. The peak wavelength near 640

nm goes from 637.72 nm to 638.298 nm to 638.978 nm to 639.659 nm. It can be seen that for every 0.05 change in the refractive index of the background, the wavelength moves by about 0.68 nm.

According to the definition of sensitivity shown in equation 2.79, the sensitivity s = 13.6 nm/RIU. The result here also depends on the number of simulated wavelength points.

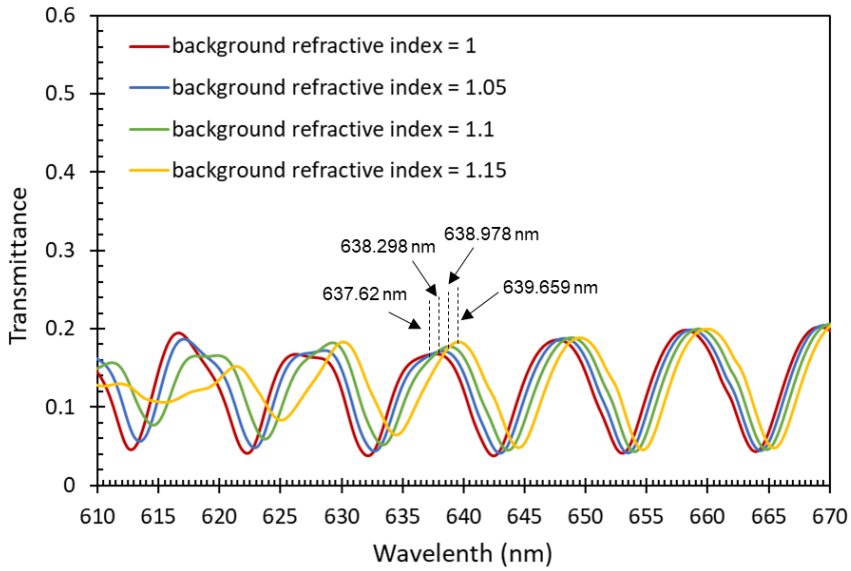

Figure 5.10 Simulated TE_0 mode sources transmittance spectra of DBRs cavity with varying background refractive index, etch depth = 780 nm, filling factor = 0.5, cavity length = 8 μm.

5.3 Measurement results

The experimental results of the grating couplers area in second chip from University of Bath have been shown in section 4.3.2. This section will show the experimental results of the grating coupler with DBRs cavity. Figure 5.11 shows the layout for one DBR cavity on the chip and Figure 5.12 shows an SEM picture of a typical 10 μm long cavity.

There are some unetched portions of the DBRs which will cause some differences between measured and modelled results.

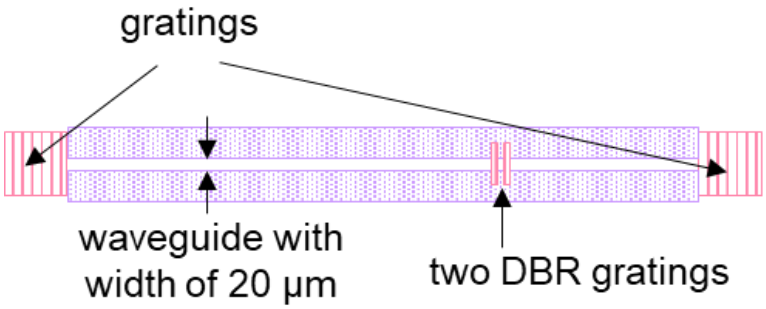

*Figure 5.11 Layout of part of the chip: grating couplers with DBR cavity. Device parameters:100 μm*100 μm coupling grating size, DBR grating length = 10 μm, DBR grating width = 60 μm, grating period = 400 nm, cavity length = 8 μm, waveguide width = 20 μm, waveguide length = 1 mm.*

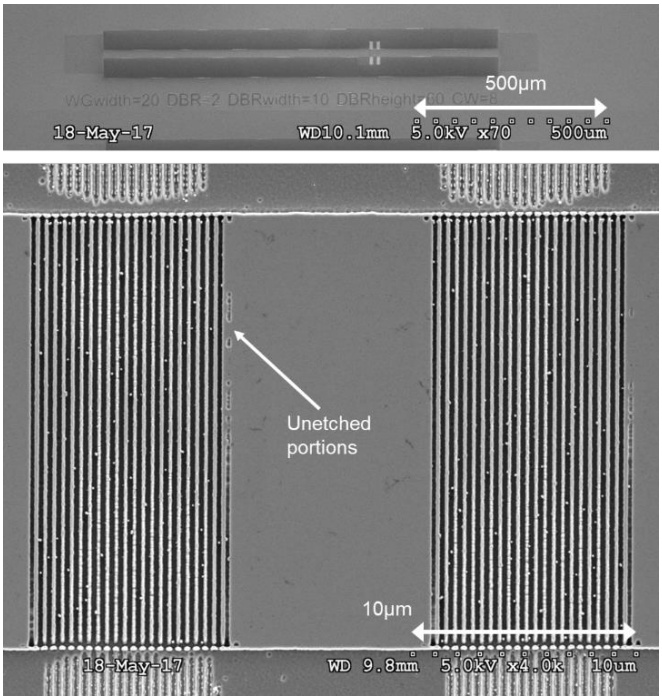

Figure 5.12 SEM images of a DBR resonant cavity.

The in-out coupling with DBR cavity measurement results are shown in Figure 5.13 for two different devices on the same chip and it can be seen that similar performance is obtained. The zoomed graphs are shown in Figure 5.14. It can be seen that similar performance is obtained. However, a mode spacing of 10 nm is observed in one case, but not for the second device. Since the waveguide is highly multimoded, the mode spacing will depend on which modes are resonating in the cavity and the defects shown in Figure 5.12 will also produce non-ideal results. Insets show visible light camera images of both cavities which shows significant scattering from the first DBR and evidence of the high intensity peaks within the cavity.

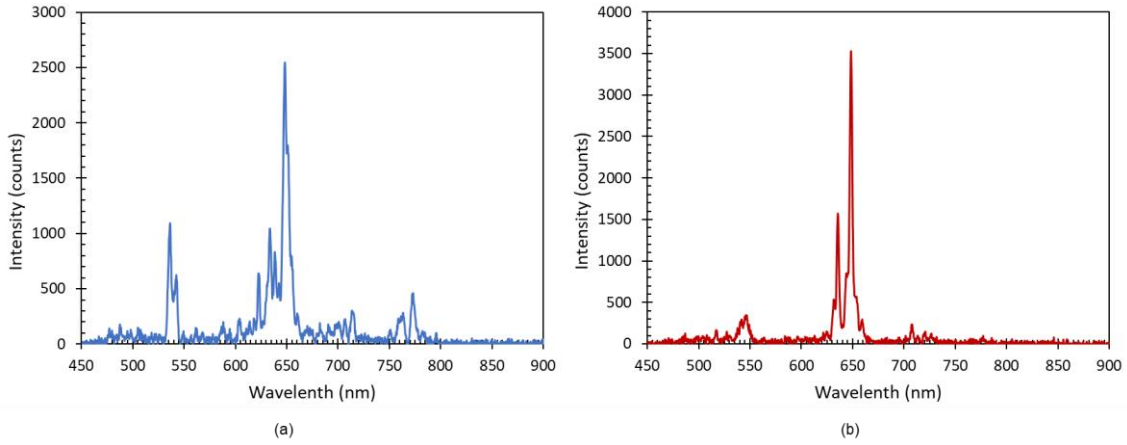

Figure 5.13 Measured in-out coupling with DBR cavities for two cavities on the same chip: (a) device 1; (b) device 2.

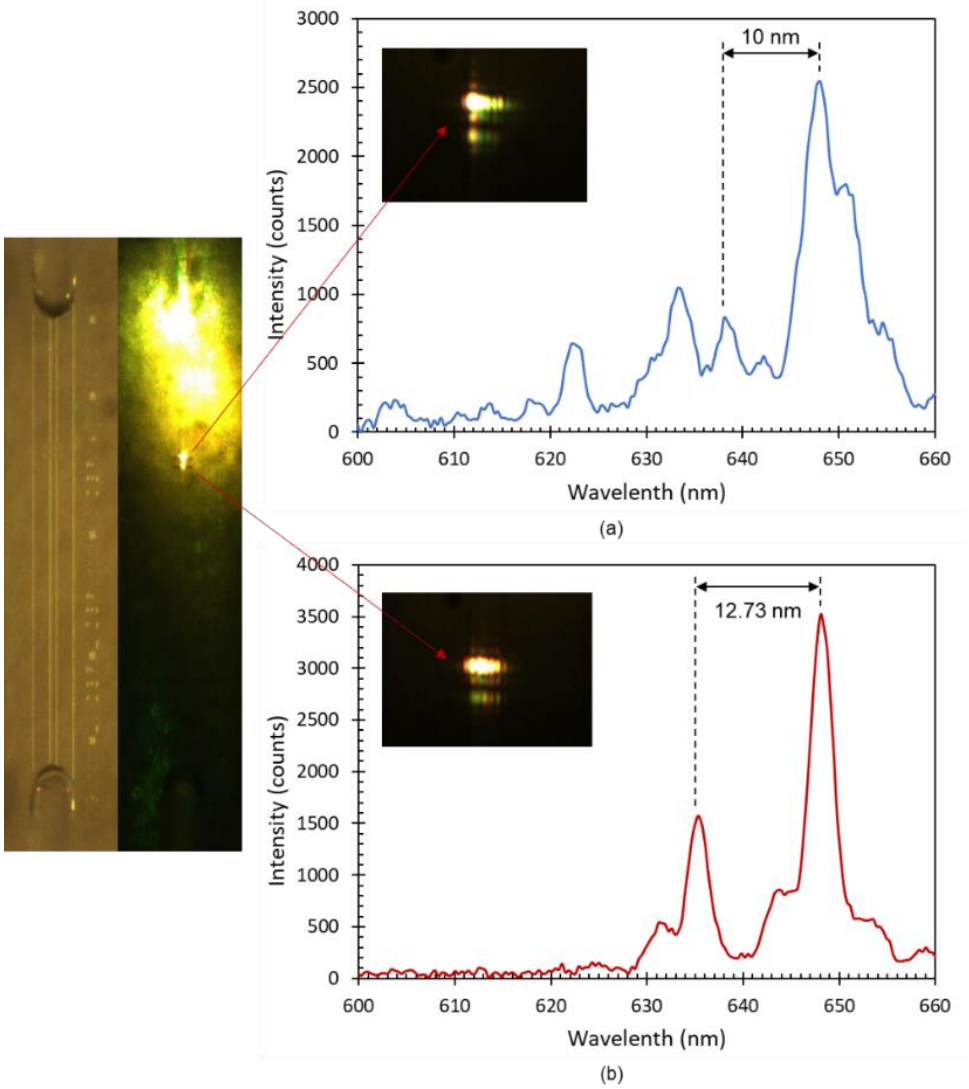

Figure 5.14 Zoom-in of measured in-out coupling for two different cavities and visible light images of light scattered from the cavities: (a) device 1; (b) device 2.

5.4 Summary

Combining with the results of the grating coupler part of the second sample in the previous chapter, this chapter discusses the simulation and experimental results of the target sensor. Limited by the requirements of simulation memory, this chapter does not

simulate the whole structure of the grating coupler with DBRs cavity sensor, only analyses and simulates the single Bragg grating and two Bragg grating with resonant cavity structures.

In the simulation, an approximately 10 nm FSR can be obtained. The same mode spacing was found in the experimental results of one of the sensor devices. The measured mode spacing is slightly different from the simulated value on another sensor with the same parameter structure. This may be caused by fabrication defects.

By changing the background refractive index, a rough simulation sensitivity value was obtained. Although the measurement of the analyte was not performed, cavities with Q factors of >200 have been measured which show the potential for this route to low-cost commercial sensor applications.

6 New grating coupler structure design

6.1 Instruction

Chapters 4 and 5 introduce the simulation and measurement results of chips fabricated by DTL technology, and their results maintain good consistency. However, due to the waveguide thickness of the GaN on sapphire platform and the period size limitation of the DTL mask, ideal grating couplers and sensors cannot be fabricated. In this chapter, we try to design a new GaN platform based grating coupler structure and fabricate the chips using electron beam lithography. Compared with DTL technology, electron beam lithography can flexibly fabricate high-precision linear gratings with any period to meet the needs of single-mode transmission.

6.2 Modelling results

We propose a new thinner GaN platform. There is a buffer layer between GaN and sapphire. It consists of a 500 nm thick GaN layer and a 100 nm thick Aluminium Nitride

(AlN) layer with sapphire substrate. Figure 6.1 is a schematic diagram of the input grating structure. The structure is fully etched, which was a fabrication decision that makes fabrication much simpler than a specific depth. We use Lumerical FDTD to optimise the maximum coupling efficiency. There are two models. One is to optimise the incident light of fundamental TE mode at 650 nm with 15 ° angle of fibre. This is based on the current measurement set up described in section 3.4. The modelling structure is shown in Figure 6.1 (a). The other model is to optimise the incident light of fundamental TE mode at 1550 nm with 9 ° angle of fibre, which is based on a different fibre and fibre angle for use on an alternative measurement setup in the future. The modelling structure is shown in Figure 6.1 (b). The diameter of the input fibre in the simulation depends on the wavelength. 650 nm wavelength use a SMF600 fibre with 125 μm cladding diameter and 4.3 μm core diameter and 1550 nm wavelength use a SM980 with 125 μm cladding diameter and 9.5 μm core diameter.

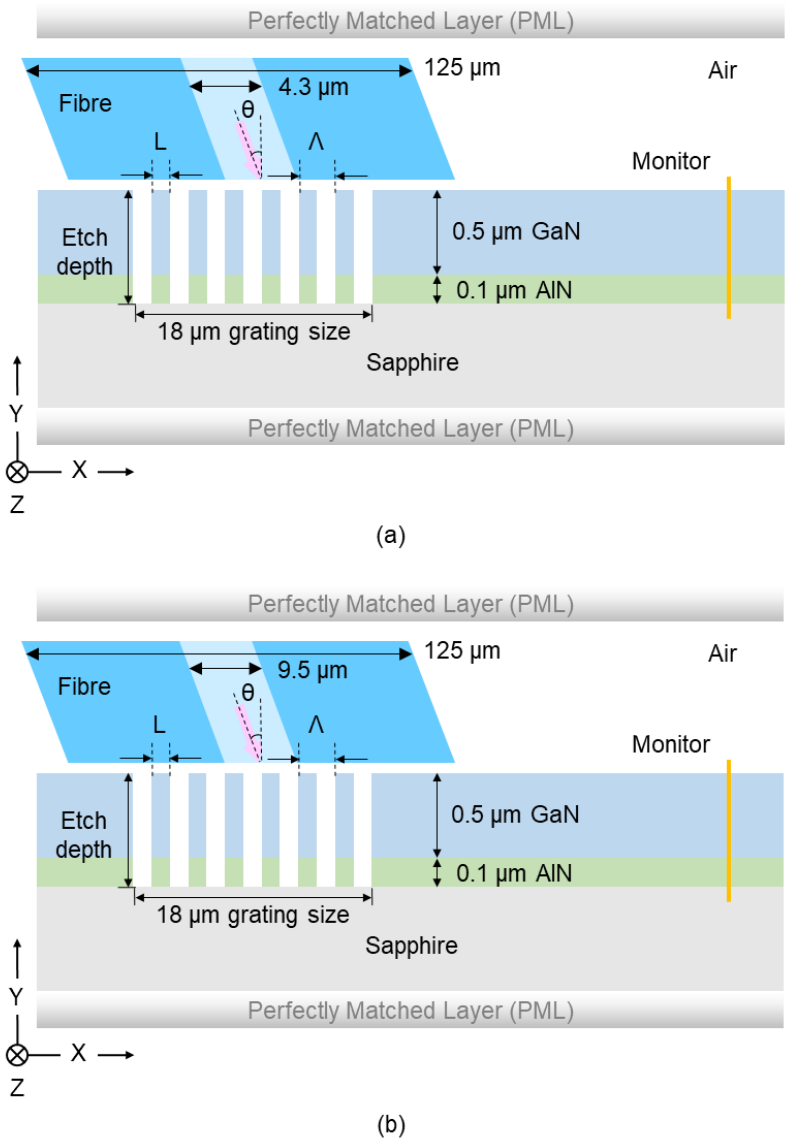

Figure 6.1 Geometry of 0.5 µm GaN-0.1 µm AlN on sapphire structure. Device parameters: grating period = Λ, filling factor = a = L/Λ, grating length = 18 µm, etch depth = 600 nm. (a) incident wavelength = 650 nm, angle of fibre = 15 °, n_{GaN} = 2.38 [148], n_{AlN} = 2.15[182], $n_{sapphire}$ = 1.77 [149]; (b) incident wavelength = 1550 nm, angle of fibre = 9 °, n_{GaN} = 2.32 [148], n_{AlN} = 2.12 [182], $n_{sapphire}$ = 1.75 [149].

We did the FDTD simulations by varying the grating period ranging from 100 to 2000 nm and filling factor from 0.2 to 0.8, the optimise coupling was found when the filling factor is 0.64 and the grating period is 830 nm for the 650 nm TE_0 mode input source at 15 ° incidence angle, and when the filling factor is 0.75 and the grating period is 954

nm for the 1550 nm TE_0 mode input source at 9 ° incidence angle. Using the FDTD's mode profiles functionality, the optimise transmittance of each mode at the monitor location can be obtained in Figure 6.2. Here, the total transmittance is the sum of the transmittance of all modes. It can be seen from the figure that almost transmittances are in TE_0 mode. This will allow the waveguide in the grating coupler to propagate only the fundamental TE mode. This will provide a good single mode transmission for the future design of adding resonant cavity in the waveguide. The magnitudes of the E_z field for the peak wavelength is shown in Figure 6.3. It can be seen that although a large amount of light is diffracted into the substrate in these two fully etched structures, almost complete single-mode transmission in the waveguide is guaranteed under these structural parameters.

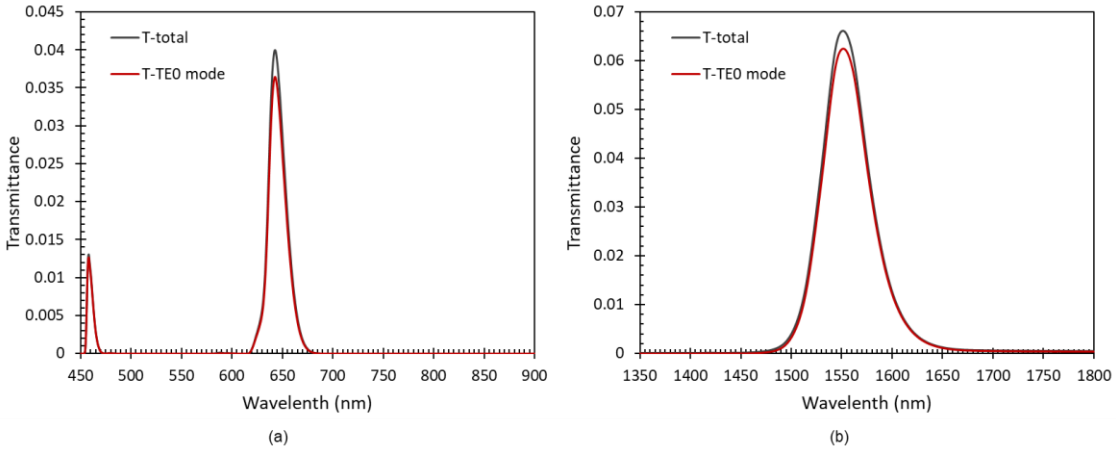

Figure 6.2 2D FDTD modelling mode profiles result for input coupling with grating length = 18 μm, etch depth = 600 nm. (a) angle of fibre = 15 °, n_{GaN} = 2.38, n_{AlN} = 2.15, $n_{sapphire}$ = 1.77, grating period = 830 nm, filling factor = 0.64; (b) angle of fibre = 9 °, n_{GaN} = 2.32, n_{AlN} = 2.12, $n_{sapphire}$ = 1.75, grating period = 954 nm, filling factor = 0.75.

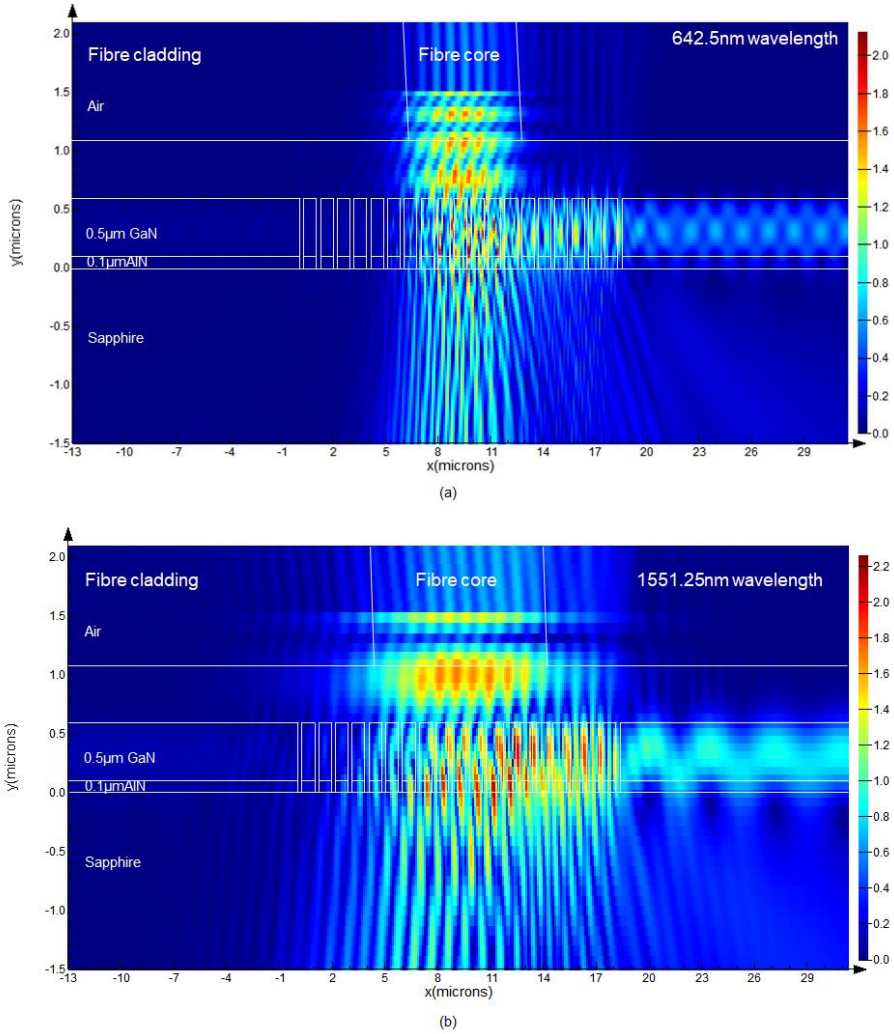

Figure 6.3 E_z field distribution in cross-section for the peak wavelength, TE_0 incidence light. Grating parameters: etch depth = 600 nm, grating length = 18 μm. (Vertical and horizontal axes not to scale). (a) angle of fibre = 15 °, n_{GaN} = 2.38, n_{AlN} = 2.15, $n_{sapphire}$ = 1.77, grating period = 830 nm, filling factor = 0.64, wavelength = 642.5 nm; (b) angle of fibre = 9 °, n_{GaN} = 2.32, n_{AlN} = 2.12, $n_{sapphire}$ = 1.75, grating period = 954 nm, filling factor = 0.75, wavelength = 1551.25 nm.

6.3 Chips by electron beam lithography

The two chips were fabricated at the Cardiff University, using electron beam lithography. The picture and layout of the chips are shown in Figure 6.4. A series of gratings with U-shaped waveguides on the two chips. There is a taper between etch

grating and waveguide. The waveguide width = 300 nm. The different electron beam exposures are used in order to work out the optimum dose. Different colour grating couplers groups represent different dose factors which is marked in the layout. The red layout area is the chip for 1550 nm wavelength. The gratings on this chip for 1550 nm wavelength have 954 nm grating period and 0.75 filling factor. The blue layout area is the chip for 650 nm wavelength. The gratings on this chip have 830 nm grating period and 0.64 filling factor. All gratings in two chips have 600 nm etch depth and all waveguide width is 300 nm.

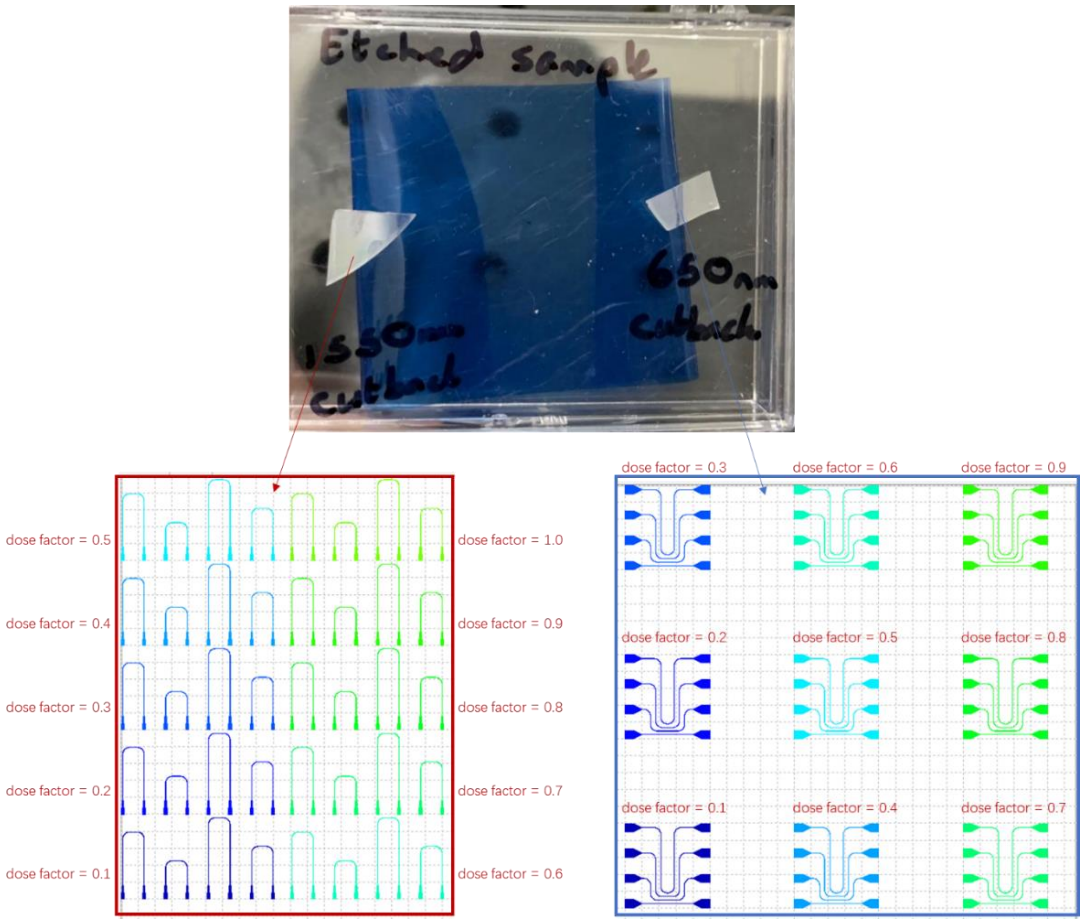

Figure 6.4 The layout of chips. The red area is the chip for 1550 nm wavelength with etch depth = 600 nm, grating period = 954 nm, filling factor = 0.75; The red area is the chip for 650 nm wavelength with etch depth = 600 nm, grating period = 830 nm, filling factor = 0.64.

Based on the grating structure on the chip, the effect of waveguide width can be observed in 3D modelling. Figure 6.5 depicted this modelling structure. It is an input grating with taper waveguide structure. Grating length = 18 μm, taper length = 6 μm balance the simulation memory requirements. Grating and rib are fully etched. For 650 nm wavelength modelling, we set grating period = 830 nm, filling factor = 0.64, grating width = 6 μm, waveguide width = 200 nm and 300 nm, angle of fibre = 15 °, n_{GaN} = 2.38, n_{AlN} = 2.15, $n_{sapphire}$ = 1.77, fibre core diameter = 4.3 μm. For 1550 nm wavelength modelling, we set grating period = 954 nm, filling factor = 0.75, grating width = 16 μm, waveguide width = 300 nm and 1μm, angle of fibre = 9 °, n_{GaN} = 2.32, n_{AlN} = 2.12, $n_{sapphire}$ = 1.75, fibre core diameter = 9.5 μm.

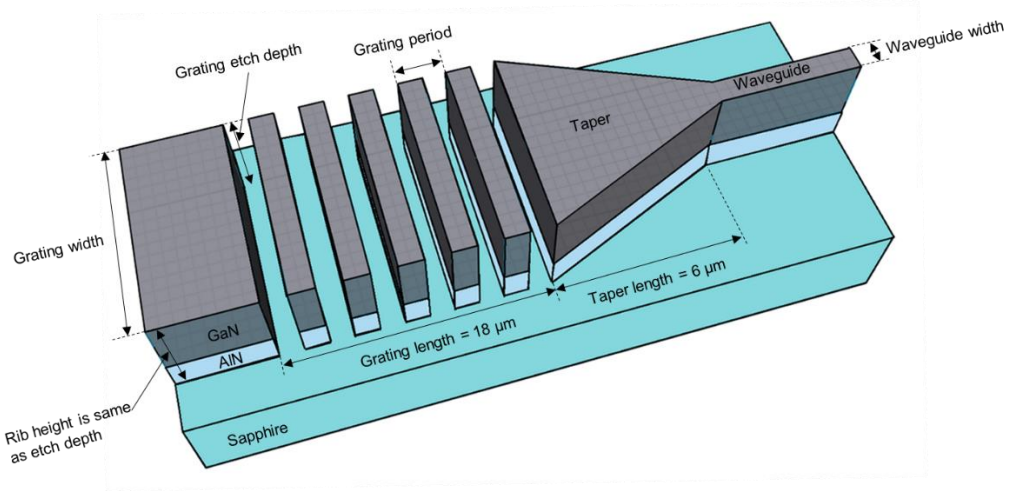

Figure 6.5 Schematic representation of 3D 500 nm GaN-100 nm AlN on sapphire input grating with taper waveguide. Device parameters: grating length = 18 μm, taper length = 6 μm, etch depth = rib height = 600 nm. 650 nm wavelength modelling with grating period = 830 nm, filling factor = 0.64, grating width = 6 μm, waveguide width = 200 nm and 300 nm; 1550 nm wavelength modelling with grating period = 954 nm, filling factor = 0.75, grating width = 16 μm, waveguide width = 300 nm and 1 μm.

Figure 6.6 shows the total transmittance and TE_{00} mode transmittance with parameters of 650 nm wavelength chip. According to the two-dimensional mode solver [168], 300 nm waveguide width will support two TE mode at 650 nm wavelength. When the

waveguide width is reduced to 200 nm, only the fundamental mode of TE mode exists. It can be seen the TE_{00} mode transmittance of the 200 nm wide waveguide is closer to the total transmittance than the 300 nm width. Figure 6.7 shows the total transmittance and TE_{00} mode transmittance with parameters of 1550 nm wavelength chip. According to the two-dimensional mode solver [168], 300 nm waveguide width does not support any mode at 1550 nm wavelength. As the waveguide widths increase to a range of 595 nm to 1230 nm, only the fundamental mode of TE mode exists. Therefore, in the case of the 300 nm waveguide width in Figure 6.7 (a), both the total transmittance and the TE_{00} mode transmittance are very low. When the waveguide width becomes 1 μm in Figure 6.7 (b), the total transmittance is improved, and almost all of them is TE_{00} mode component.

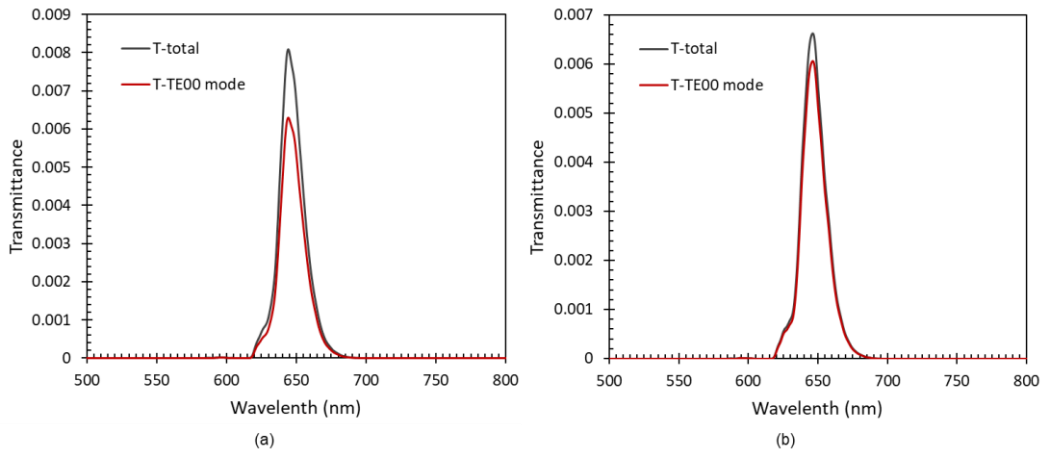

Figure 6.6 3D FDTD modelling mode profiles result for input coupling. Device parameters: grating length = 18 μm, taper length = 6 μm, etch depth = rib height = 600 nm, grating period = 830 nm, filling factor = 0.64, grating width = 6 μm, angle of fibre = 15 °, n_{GaN} = 2.38, n_{AlN} = 2.15, $n_{sapphire}$ = 1.77, fibre core diameter = 4.3 μm. (a) waveguide width = 300 nm; (b) waveguide width = 200 nm

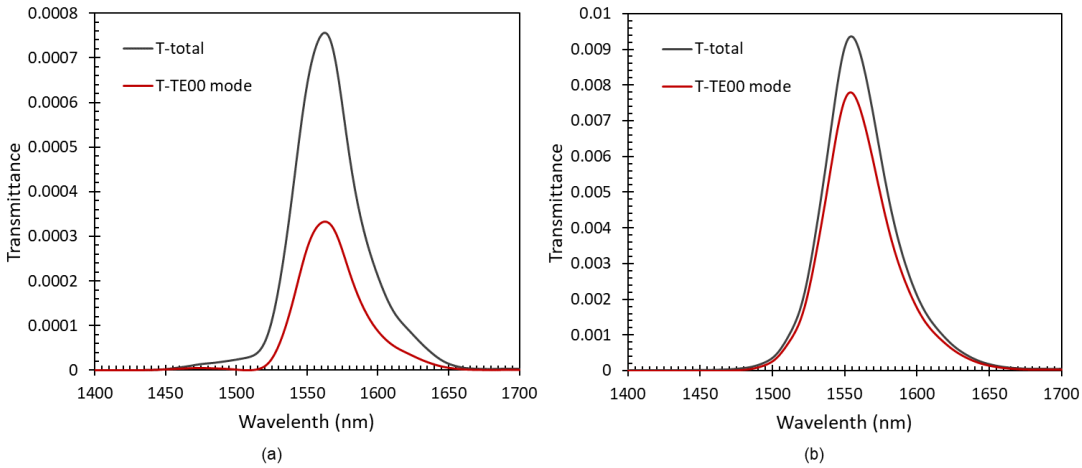

Figure 6.7 3D FDTD modelling mode profiles result for input coupling. Device parameters: grating length = 18 μm, taper length = 6 μm, etch depth = rib height = 600 nm, grating period = 954 nm, filling factor = 0.75, grating width = 16 μm, angle of fibre = 9 °, n_{GaN} = 2.32, n_{AlN} = 2.12, $n_{sapphire}$ = 1.75, fibre core diameter = 9.5 μm. (a) waveguide width = 300 nm; (b) waveguide width = 1 μm

Figure 6.8 shows Microscope and SEM pictures of the two chips. It can be seen from the SEM picture of the grating that there are still some fabrication defects. In the 650 nm wavelength grating, there is only partial lift off of the Ni mask which is shown in Figure 6.8 (a). In the 1550 nm wavelength grating, the issue is similar to the 650 nm case except additional problem proximity effects causing merging of gratings. We will measure these sample in the future and try to solve these fabrication problems.

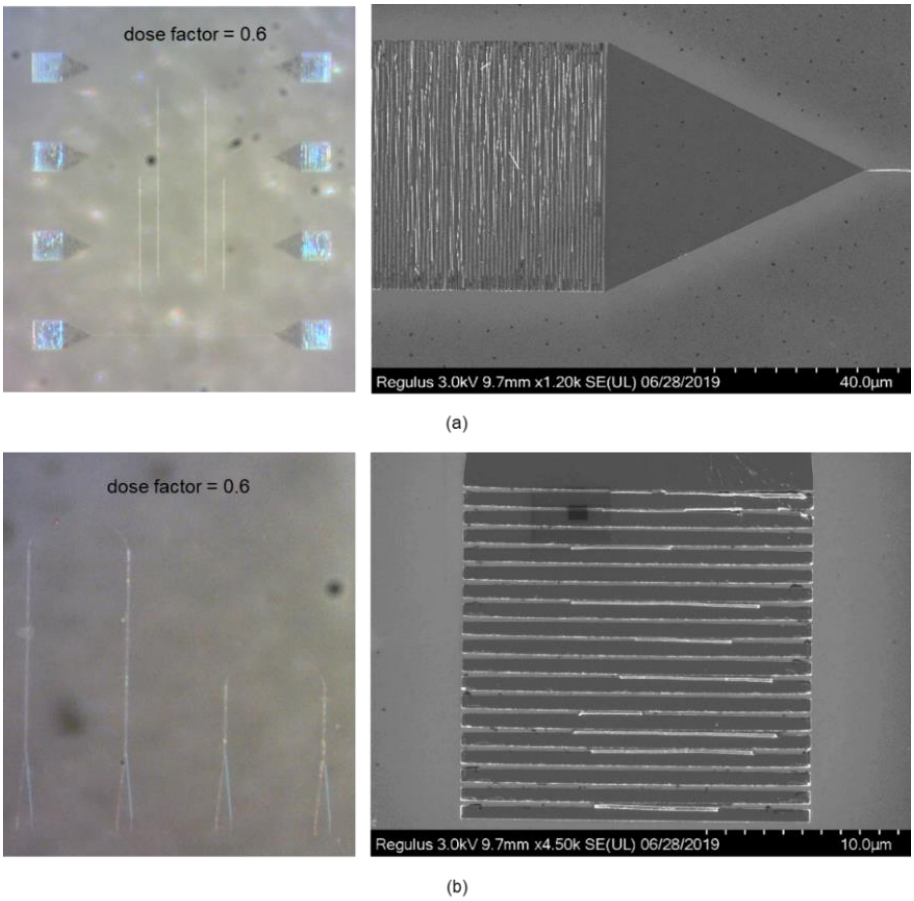

Figure 6.8 Microscope and SEM pictures of gratings: (a) 650 nm wavelength chip with does factor = 0.6; (b) 1550 nm wavelength chip with does factor = 0.6.

6.4 Summary

This chapter introduces a new GaN-based platform structure, which is GaN-AlN-sapphire. The GaN layer is 500 nm thick and AlN layer is 100 nm thick. Based on this structure, we have optimised the parameters of a fully etched input grating at 650 nm wavelength with 15 ° angle of incidence and 1550 nm wavelength with 9 ° angle of incidence. Simulation results show better transmittances in single mode guided which will result in much more idealised cavity behaviour in the future.

The samples have been fabricated by electron beam lithography. In the future, we will consider adding a linear polariser to the measurement set up to constrain the polarisation of the incident light in TE or TM mode.

7 Conclusions and further work

7.1 Conclusions

This project investigated the feasibility of a GaN-based 1D PhC platform as a biosensor.

Chapter 1 introduces integrated optics and PhCs, which are a combination of nanotechnology and photonics. With their structural characteristics, they can create devices that limit and manipulate nanoscale light. These devices have important research value in chemical and biosensor applications. An overview of biosensors is then provided. The advantages and disadvantages of labelled and label-free sensors are compared, and some examples of optical-based biosensors are listed. The last part introduces the characteristics of the GaN material system and reviews its development. Its outstanding research results in LEDs, waveguides and cavity structures that make it a promising platform material for PhC biosensors.

Chapter 2 elaborates the basic theory of waveguide structures and 1D PhC structures represented by linear gratings in detail, which provides a theoretical basis for the simulation and experimental results of subsequent chapters. Based on the design of the

target sensor structure, the working principles of grating coupler, Bragg grating and Fabry-Perot cavity are introduced. Next, the current research results of the coupling efficiency of GaN-based platform coupler and the Q factor performance of GaN-based cavity structures are listed. These research results lay a good foundation for the realization of GaN-based sensors in subsequent chapters. In addition, the dispersion diagram of the slab waveguide and one-dimensional PhC band diagram also provide a theoretical basis for subsequent simulation results.

Chapter 3 describes the numerical electromagnetic methods used in this paper, which is FDTD. In addition to an overview of the core algorithm principles, the selection of sources, boundary conditions and mesh sizes for different modelling situations in the Lumerical FDTD solution software is also discussed. After that, some simple examples of grating couplers and resonators are constructed to verify the theory and simulation results. Band diagrams are also used to help verify these results. The measurement set up section details the initial in-out coupling test set up used to obtain the grating coupling performance at a single wavelength. Then according to the measurement needs, the set up was improved to adjust the location of the fibres more accurately. This updated set up is used to measure the coupling intensity from the supercontinuum laser light source. Finally, an overview of the two fabrication methods for the chips is given at the end of this chapter.

Chapter 4 discussed in detail the design of grating coupler for the 1.5 μm thick GaN on sapphire Platform based on our published paper. A wavelength range of 630-640 nm was selected as the based on early red laser sources and GaN samples. The angle of incidence was fixed at 15 ° and the grating period was determined by the available mask size of the DTL process from University of Bath. FDTD simulation is used to adjust the filling factor and etch depth to optimise the coupling efficiency. The two chips we measured are fabricated by the University of Bath. The coupling efficiency and loss

between two gratings without waveguides were measured by the initial experimental set up. The coupling efficiency and waveguide loss of samples with varying the waveguide length were measured with an improved experimental set up. Good agreement was obtained between modelling and measurement, and it could be seen from the insertion loss plots that integrating the waveguide between the gratings improves the loss.

Chapter 5 focused on the modelling and analysis of resonant cavities. The integrated Fabry-Perot isolated cavity is modelling based on measurement results of grating coupler. However, due to DTL fabrication limitations, all the gratings on the chip maintain the same parameters. This leads to the structure to be considered as a higher-order Bragg grating for the target wavelength. In addition, there is problems with multimode guiding in the waveguide caused by the thickness of waveguide. These problems lead to non-ideal behaviour. When a cavity is introduced, we can observe two resonant peaks with Q factor > 200. A mode spacing of ~10 nm in the measurement which is close to the modelled results.

Chapter 6 discussed a new GaN-AlN-sapphire platform structure. Due to DTL fabrication limitations, this chip was fabricated using electron beam lithography technology which can easily adjust the grating period and filling factor. Under the condition of the fully etched, we have achieved good simulated transmittance at the target wavelengths of 650 nm and 1550 nm and meet the needs of single mode guided in the waveguide. However, the electron beam process of the currently obtained chips still needs to be improved to reduce defects.

7.2 Further work and improvements

Although the simulation results and experimental results of grating couplers and grating coupler integrated resonators show that GaN-based linear grating platforms can be used for low-cost commercial sensor applications. However, there is still much room for improvement in future work.

1. Single-mode waveguides will be fabricated which will result in much more idealised grating coupler and cavity behaviour which will lead to increased device performance.
2. The main restriction for the DTL approach is that all gratings must have the same period, but with correct processing, different etch depths and filling factors could be obtained which would further improve the device performance.
3. Improve the linear grating of input and output to curved gratings. The in-out coupling efficiency can be further improved by optimising the curved grating with tapered waveguides.
4. The measurement set up needs to update. In the current set up, it is difficult to maintain the optimal in and out fibre position and height between fibre and sample every time. The adjustment on the X, Y and Z micrometre drivers on the fibre holder are not fine-tuned enough to easily position the fibre to find the best results.
5. Because the grating coupler is dependent on the polarisation direction of the input light, polarisation control is needed to obtain coupling results in TE or TM mode. For example, adding a linear polariser in a free space part, or replacing fibres with a polarization maintaining fibres.

8 References

[1] G. Lifante, *Integrated photonics: fundamentals*. Wiley Online Library, 2003.

[2] A. K. Datta and S. Munshi, *Information photonics: fundamentals, technologies, and applications*. CRC Press, 2016.

[3] S. E. Miller, "INTEGRATED OPTICS - AN INTRODUCTION," *Bell System Technical Journal*, vol. 48, no. 7, pp. 2059-+, 1969 1969, doi: 10.1002/j.1538-7305.1969.tb01165.x.

[4] S. Somekh and A. Yariv, "FIBRE OPTICS COMMUNICATIONS," *International Telemetering Conference Proceedings*, 1972.

[5] R. V. Nair and R. Vijaya, "Photonic crystal sensors: An overview," *Progress in Quantum Electronics*, vol. 34, no. 3, pp. 89-134, 2010/05/01/ 2010, doi: https://doi.org/10.1016/j.pquantelec.2010.01.001.

[6] J. Singh, *Physics of Semiconductors and their Heterostructures*. McGraw-Hill New York, 1993.

[7] G. A. Sai-Halasz, R. Tsu, and L. Esaki, "A new semiconductor superlattice," *Applied Physics Letters,* vol. 30, no. 12, pp. 651-653, 1977.

[8] L. Esaki and R. Tsu, "Superlattice and negative differential conductivity in semiconductors," *IBM Journal of Research and Development,* vol. 14, no. 1, pp. 61-65, 1970.

[9] E. Yablonovitch, "INHIBITED SPONTANEOUS EMISSION IN SOLID-STATE PHYSICS AND ELECTRONICS," *Physical Review Letters,* vol. 58, no. 20, pp. 2059-2062, May 1987, doi: 10.1103/PhysRevLett.58.2059.

[10] S. John, "STRONG LOCALIZATION OF PHOTONS IN CERTAIN DISORDERED DIELECTRIC SUPERLATTICES," *Physical Review Letters,* vol. 58, no. 23, pp. 2486-2489, Jun 1987, doi: 10.1103/PhysRevLett.58.2486.

[11] J. D. Joannopoulos, S. G. Johnson, J. N. Winn, and R. D. Meade, "Molding the flow of light," *Princeton Univ. Press, Princeton, NJ [ua],* 2008.

[12] K. Sakoda, *Optical properties of photonic crystals*. Springer Science & Business Media, 2004.

[13] H. Hojo and A. Mase, "Dispersion relation of electromagnetic waves in one-dimensional plasma photonic crystals," *Journal of Plasma and Fusion Research,* vol. 80, no. 2, pp. 89-90, 2004.

[14] M. Centini *et al.*, "Dispersive properties of finite, one-dimensional photonic band gap structures: applications to nonlinear quadratic interactions," *Physical Review E,* vol. 60, no. 4, p. 4891, 1999.

[15] R. Moussa, L. Salomon, J. P. Dufour, and H. Aourag, "Large photonic band gap's in one-dimensional multilayer structures," *Journal of Physics and Chemistry of Solids*, vol. 63, no. 5, pp. 725-732, 2002.

[16] J. N. Winn, Y. Fink, S. Fan, and J. D. Joannopoulos, "Omnidirectional reflection from a one-dimensional photonic crystal," *Optics letters*, vol. 23, no. 20, pp. 1573-1575, 1998.

[17] H. Inouye, M. Arakawa, J. Y. Ye, T. Hattori, H. Nakatsuka, and K. Hirao, "Optical properties of a total-reflection-type one-dimensional photonic crystal," *IEEE Journal of quantum electronics*, vol. 38, no. 7, pp. 867-871, 2002.

[18] H. Jiang, H. Chen, H. Li, Y. Zhang, J. Zi, and S. Zhu, "Properties of one-dimensional photonic crystals containing single-negative materials," *Physical Review E*, vol. 69, no. 6, p. 066607, 2004.

[19] N.-h. Liu, S.-Y. Zhu, H. Chen, and X. Wu, "Superluminal pulse propagation through one-dimensional photonic crystals with a dispersive defect," *Physical Review E*, vol. 65, no. 4, p. 046607, 2002.

[20] J. Cos, J. Ferré-Borrull, J. Pallarès, and L. F. Marsal, "Double-cavity Fabry–Pérot tunable equaliser based on 1D photonic crystals," *International Journal of Numerical Modelling: Electronic Networks, Devices and Fields*, vol. 23, no. 4-5, pp. 400-410, 2010.

[21] O. El Gawhary, M. C. Dheur, S. F. Pereira, and J. J. M. Braat, "Extension of the classical Fabry–Perot formula to 1D multilayered structures," *Applied Physics B*, vol. 111, no. 4, pp. 637-645, 2013.

[22] S. V. Zhukovsky and A. G. Smirnov, "All-optical diode action in asymmetric nonlinear photonic multilayers with perfect transmission resonances," *Physical Review A*, vol. 83, no. 2, p. 023818, 2011.

[23] E. Cubukcu, K. Aydin, E. Ozbay, S. Foteinopoulou, and C. M. Soukoulis, "Subwavelength resolution in a two-dimensional photonic-crystal-based superlens," *Physical review letters*, vol. 91, no. 20, p. 207401, 2003.

[24] R. Moukhtari, A. Hocini, and D. Khedrouche, "Study of Two-Dimensional Photonic Crystal Microcavities as a Function of Refractive Index," *Acta Physica Polonica A*, vol. 129, no. 4, pp. 556-558, 2016.

[25] Y. Wang, D. Zhang, B. Xu, Z. Dong, J. Pei, and S. Xu, "T-typed photonic crystal circulator with square lattice Al2O3 rods array and NiZn-ferrite posts," *Materials & Design*, vol. 181, p. 107978, 2019.

[26] S. Assefa *et al.*, "Guiding 1.5 μm light in photonic crystals based on dielectric rods," *Applied physics letters*, vol. 85, no. 25, pp. 6110-6112, 2004.

[27] D. Cassagne, C. Jouanin, and D. Bertho, "Hexagonal photonic-band-gap structures," *Physical review B*, vol. 53, no. 11, p. 7134, 1996.

[28] Y. Akahane, T. Asano, B.-S. Song, and S. Noda, "High-Q photonic nanocavity in a two-dimensional photonic crystal," *nature*, vol. 425, no. 6961, p. 944, 2003.

[29] O. Painter *et al.*, "Two-dimensional photonic band-gap defect mode laser," *Science*, vol. 284, no. 5421, pp. 1819-1821, 1999.

[30] M. Meier *et al.*, "Laser action from two-dimensional distributed feedback in photonic crystals," *Applied Physics Letters*, vol. 74, no. 1, pp. 7-9, 1999.

[31] S. W. Leonard *et al.*, "Tunable two-dimensional photonic crystals using liquid crystal infiltration," *Physical Review B,* vol. 61, no. 4, pp. R2389-R2392, 01/15/ 2000, doi: 10.1103/PhysRevB.61.R2389.

[32] E. Özbay *et al.*, "Measurement of a three-dimensional photonic band gap in a crystal structure made of dielectric rods," *Physical Review B,* vol. 50, no. 3, p. 1945, 1994.

[33] K. M. Ho, C. T. Chan, C. M. Soukoulis, R. Biswas, and M. Sigalas, "Photonic band gaps in three dimensions: new layer-by-layer periodic structures," *Solid State Communications,* vol. 89, no. 5, pp. 413-416, 1994.

[34] S. Noda, K. Tomoda, N. Yamamoto, and A. Chutinan, "Full three-dimensional photonic bandgap crystals at near-infrared wavelengths," *Science,* vol. 289, no. 5479, pp. 604-606, 2000.

[35] M. Deubel, G. Von Freymann, M. Wegener, S. Pereira, K. Busch, and C. M. Soukoulis, "Direct laser writing of three-dimensional photonic-crystal templates for telecommunications," *Nature materials,* vol. 3, no. 7, p. 444, 2004.

[36] P. Vukusic and J. R. Sambles, "Photonic structures in biology," *Nature,* vol. 424, no. 6950, p. 852, 2003.

[37] E. Armstrong and C. O'Dwyer, "Artificial opal photonic crystals and inverse opal structures–fundamentals and applications from optics to energy storage," *Journal of Materials Chemistry C,* vol. 3, no. 24, pp. 6109-6143, 2015.

[38] S. Yoshioka and S. Kinoshita, "Wavelength–selective and anisotropic light–diffusing scale on the wing of the morpho butterfly," *Proceedings of the Royal Society of London. Series B: Biological Sciences,* vol. 271, no. 1539, pp. 581-587, 2004.

[39] F. Mika, J. Matějková-Plšková, S. Jiwajinda, P. Dechkrong, and M. Shiojiri, "Photonic crystal structure and colouration of wing scales of butterflies exhibiting selective wavelength iridescence," *Materials,* vol. 5, no. 5, pp. 754-771, 2012.

[40] E. Yablonovitch, T. J. Gmitter, and K.-M. Leung, "Photonic band structure: The face-centred-cubic case employing nonspherical atoms," *Physical review letters,* vol. 67, no. 17, p. 2295, 1991.

[41] S.-Y. Lin, E. Chow, V. Hietala, P. R. Villeneuve, and J. D. Joannopoulos, "Experimental Demonstration of Guiding and Bending of Electromagnetic Waves in a Photonic Crystal," *Science,* vol. 282, no. 5387, pp. 274-276, 1998.

[42] "ALPhANOV." https://www.alphanov.com/en/products-services/photonic-crystal-fibre-interfacing (accessed.

[43] "Photonics Bretagne." https://www.photonics-bretagne.com/en/perfos-rto/products/specialty-optical-fibres/ (accessed.

[44] "NKT PHOTONICS." https://www.nktphotonics.com/lasers-fibres/technology/photonic-crystal-fibres/ (accessed.

[45] T. A. Birks, J. C. Knight, and P. S. J. Russell, "Endlessly single-mode photonic crystal fibre," *Optics letters,* vol. 22, no. 13, pp. 961-963, 1997.

[46] T. Schreiber *et al.*, "Stress-induced single-polarization single-transverse mode photonic crystal fibre with low nonlinearity," *Optics Express,* vol. 13, no. 19, pp. 7621-7630, 2005.

[47] T. D. Happ, M. Kamp, A. Forchel, J.-L. Gentner, and L. Goldstein, "Two-dimensional photonic crystal coupled-defect laser diode," *Applied physics letters,* vol. 82, no. 1, pp. 4-6, 2003.

[48] M. Lončar, T. Yoshie, A. Scherer, P. Gogna, and Y. Qiu, "Low-threshold photonic crystal laser," *Applied Physics Letters,* vol. 81, no. 15, pp. 2680-2682, 2002.

[49] J. Li, J. He, and Z. Hong, "Terahertz wave switch based on silicon photonic crystals," *Applied optics,* vol. 46, no. 22, pp. 5034-5037, 2007.

[50] H. Nakamura *et al.*, "Ultra-fast photonic crystal/quantum dot all-optical switch for future photonic networks," *Optics express,* vol. 12, no. 26, pp. 6606-6614, 2004.

[51] S. Jena, R. B. Tokas, S. Thakur, and D. V. Udupa, "Tunable mirrors and filters in 1D photonic crystals containing polymers," *Physica E: Low-dimensional Systems and Nanostructures,* vol. 114, p. 113627, 2019.

[52] H. Inan *et al.*, "Photonic crystals: emerging biosensors and their promise for point-of-care applications," *Chemical Society Reviews,* vol. 46, no. 2, pp. 366-388, 2017.

[53] A. Turner, I. Karube, and G. S. Wilson, *Biosensors: fundamentals and applications*. Oxford university press, 1987.

[54] F.-G. Banica, *Chemical sensors and biosensors: fundamentals and applications*. John Wiley & Sons, 2012.

[55] P. M. O'Neill, J. E. Fletcher, C. G. Stafford, P. B. Daniels, and T. Bacarese-Hamilton, "Use of an optical biosensor to measure prostate-specific antigen in whole blood," *Sensors and Actuators B: Chemical,* vol. 29, no. 1-3, pp. 79-83, 1995.

[56] E.-H. Yoo and S.-Y. Lee, "Glucose biosensors: an overview of use in clinical practice," *Sensors,* vol. 10, no. 5, pp. 4558-4576, 2010.

[57] M. Bartoszcze, "Methods of biological weapon threats detection," *Przeglad epidemiologiczny,* vol. 57, no. 2, pp. 369-376, 2003.

[58] E. C. Alocilja and S. M. Radke, "Market analysis of biosensors for food safety," *Biosensors and Bioelectronics,* vol. 18, no. 5-6, pp. 841-846, 2003.

[59] D. Yu, B. Blankert, J. C. Viré, and J. M. Kauffmann, "Biosensors in drug discovery and drug analysis," *Analytical letters,* vol. 38, no. 11, pp. 1687-1701, 2005.

[60] S. Rodriguez-Mozaz, M. J. L. de Alda, M.-P. Marco, and D. Barceló, "Biosensors for environmental monitoring: A global perspective," *Talanta,* vol. 65, no. 2, pp. 291-297, 2005.

[61] J. E. Pearson, A. Gill, and P. Vadgama, "Analytical aspects of biosensors," *Annals of clinical biochemistry,* vol. 37, no. 2, pp. 119-145, 2000.

[62] P. Damborský, J. Švitel, and J. Katrlík, "Optical biosensors," *Essays in biochemistry,* vol. 60, no. 1, pp. 91-100, 2016.

[63] W. E. Moerner, "New directions in single-molecule imaging and analysis," *Proceedings of the National Academy of Sciences,* vol. 104, no. 31, pp. 12596-12602, 2007.

[64] A. Syahir, K. Usui, K.-y. Tomizaki, K. Kajikawa, and H. Mihara, "Label and label-free detection techniques for protein microarrays," *Microarrays,* vol. 4, no. 2, pp. 228-244, 2015.

[65] M.-J. Bañuls, R. Puchades, and Á. Maquieira, "Chemical surface modifications for the development of silicon-based label-free integrated optical (IO) biosensors: A review," *Analytica chimica acta*, vol. 777, pp. 1-16, 2013.

[66] Y. Al-Qazwini, A. S. M. Noor, M. H. Yaacob, S. W. Harun, and M. A. Mahdi, "Experimental realization and performance evaluation of refractive index SPR sensor based on unmasked short tapered multimode-fibre operating in aqueous environments," *Sensors and Actuators A: Physical*, vol. 236, pp. 38-43, 2015.

[67] L. Duan, X. Yang, Y. Lu, and J. Yao, "Hollow-fibre-based surface plasmon resonance sensor with large refractive index detection range and high linearity," *Applied Optics*, vol. 56, no. 36, pp. 9907-9912, 2017.

[68] Z. Tian *et al.*, "Refractive index sensing with Mach–Zehnder interferometer based on concatenating two single-mode fibre tapers," *IEEE Photonics Technology Letters*, vol. 20, no. 8, pp. 626-628, 2008.

[69] D. Wu *et al.*, "Refractive index sensing based on Mach–Zehnder interferometer formed by three cascaded single-mode fibre tapers," *Applied optics*, vol. 50, no. 11, pp. 1548-1553, 2011.

[70] T. Claes, J. G. Molera, K. De Vos, E. Schacht, R. Baets, and P. Bienstman, "Label-free biosensing with a slot-waveguide-based ring resonator in silicon on insulator," *IEEE Photonics journal*, vol. 1, no. 3, pp. 197-204, 2009.

[71] C. A. Barrios *et al.*, "Label-free optical biosensing with slot-waveguides," *Optics letters*, vol. 33, no. 7, pp. 708-710, 2008.

[72] P. Xu, J. Zheng, J. Zhou, Y. Chen, C. Zou, and A. Majumdar, "Multi-slot photonic crystal cavities for high-sensitivity refractive index sensing," *Optics express*, vol. 27, no. 3, pp. 3609-3616, 2019.

[73] Y. Gao, P. Dong, and Y. Shi, "Suspended slotted photonic crystal cavities for high-sensitivity refractive index sensing," *Optics Express*, vol. 28, no. 8, pp. 12272-12278, 2020.

[74] B. Wang, M. A. Dündar, R. Nötzel, F. Karouta, S. He, and R. W. van der Heijden, "Photonic crystal slot nanobeam slow light waveguides for refractive index sensing," *Applied Physics Letters*, vol. 97, no. 15, p. 151105, 2010.

[75] X. Fan, I. M. White, S. I. Shopova, H. Zhu, J. D. Suter, and Y. Sun, "Sensitive optical biosensors for unlabeled targets: A review," *analytica chimica acta*, vol. 620, no. 1-2, pp. 8-26, 2008.

[76] T. M. Chinowsky *et al.*, "Compact, high performance surface plasmon resonance imaging system," *Biosensors and Bioelectronics*, vol. 22, no. 9-10, pp. 2208-2215, 2007.

[77] W.-C. Law *et al.*, "Wide dynamic range phase-sensitive surface plasmon resonance biosensor based on measuring the modulation harmonics," *Biosensors and Bioelectronics*, vol. 23, no. 5, pp. 627-632, 2007.

[78] B. J. Nelson, "Assimilating disparate sensory feedback within virtual environments for telerobotic systems," *Robotics and autonomous systems*, vol. 36, no. 1, pp. 1-10, 2001.

[79] Y. Teramura and H. Iwata, "Label-free immunosensing for α-fetoprotein in human plasma using surface plasmon resonance," *Analytical biochemistry*, vol. 365, no. 2, pp. 201-207, 2007.

[80] D. Dorfner *et al.*, "Photonic crystal nanostructures for optical biosensing applications," *Biosensors and Bioelectronics*, vol. 24, no. 12, pp. 3688-3692, 2009.

[81] Q. Liu *et al.*, "Mach–Zehnder interferometer (MZI) point-of-care system for rapid multiplexed detection of microRNAs in human urine specimens," *Biosensors and Bioelectronics*, vol. 71, pp. 365-372, 2015.

[82] Y. Chen, J. Liu, Z. Yang, J. S. Wilkinson, and X. Zhou, "Optical biosensors based on refractometric sensing schemes: A review," *Biosensors and Bioelectronics*, p. 111693, 2019.

[83] Y. Chen *et al.*, "Label-free biosensing using cascaded double-microring resonators integrated with microfluidic channels," *Optics Communications*, vol. 344, pp. 129-133, 2015.

[84] S. Chakravarty, J. Topol'ančik, P. Bhattacharya, S. Chakrabarti, Y. Kang, and M. E. Meyerhoff, "Ion detection with photonic crystal microcavities," *Optics letters*, vol. 30, no. 19, pp. 2578-2580, 2005.

[85] M. Lee and P. M. Fauchet, "Two-dimensional silicon photonic crystal based biosensing platform for protein detection," *Optics express*, vol. 15, no. 8, pp. 4530-4535, 2007.

[86] M. S. Shur, "GaN based transistors for high power applications," *Solid-State Electronics*, vol. 42, no. 12, pp. 2131-2138, 1998.

[87] L. Shen *et al.*, "AlGaN/AlN/GaN high-power microwave HEMT," *IEEE Electron Device Letters,* vol. 22, no. 10, pp. 457-459, 2001.

[88] M. Rodriguez, Y. Zhang, and D. Maksimović, "High-frequency PWM buck converters using GaN-on-SiC HEMTs," *IEEE Transactions on Power Electronics,* vol. 29, no. 5, pp. 2462-2473, 2013.

[89] J. Delaine, P.-O. Jeannin, D. Frey, and K. Guepratte, "High frequency DC-DC converter using GaN device," 2012: IEEE, pp. 1754-1761.

[90] A. Lidow, M. De Rooij, J. Strydom, D. Reusch, and J. Glaser, *GaN transistors for efficient power conversion*. John Wiley & Sons, 2019.

[91] "What is GaN?" https://epc-co.com/epc/GalliumNitride/WhatisGaN.aspx (accessed.

[92] T. J. Flack, B. N. Pushpakaran, and S. B. Bayne, "GaN technology for power electronic applications: a review," *Journal of Electronic Materials,* vol. 45, no. 6, pp. 2673-2682, 2016.

[93] "Anker PowerPort Atom." https://www.anker.com/deals/powerport_atom (accessed.

[94] TDK-Lambda. "How GaN technology is transforming power supply design." https://blog.uk.tdk-lambda.com/uk/2019/08/28/how-gan-technology-is-transforming-power-supply-design/ (accessed.

[95] "Communications & Power Industries LLC." https://www.cpii.com/product.cfm/8/61 (accessed.

[96] C. P. I. LLC. "Innovative Solid State Amplifier Technology in the 21st century." https://www.cpii.com/docs/library/4/GaN%20vs%20GaAs%20rev%201.pdf (accessed.

[97] E. Alekseev and D. Pavlidis, "Large-signal microwave performance of GaN-based NDR diode oscillators," *Solid-State Electronics*, vol. 44, no. 6, pp. 941-947, 2000.

[98] K. Ahi, "Review of GaN-based devices for terahertz operation," *Optical Engineering*, vol. 56, no. 9, p. 090901, 2017.

[99] F. A. Ponce and D. P. Bour, "Nitride-based semiconductors for blue and green light-emitting devices," *Nature*, vol. 386, no. 6623, p. 351, 1997.

[100] S. Nakamura and G. Fasol, *The blue laser diode: GaN based light emitters and lasers*. Springer Science & Business Media, 2013.

[101] H. Teisseyre *et al.*, "GaN doped with beryllium—An effective light converter for white light emitting diodes," *Applied Physics Letters*, vol. 103, no. 1, p. 011107, 2013.

[102] S. Nakamura, T. Mukai, and M. Senoh, "High-power GaN pn junction blue-light-emitting diodes," *Japanese Journal of Applied Physics*, vol. 30, no. 12A, p. L1998, 1991.

[103] S. Nakamura, T. Mukai, and M. Senoh, "Candela-class high-brightness InGaN/AlGaN double-heterostructure blue-light-emitting diodes," *Applied Physics Letters*, vol. 64, no. 13, pp. 1687-1689, 1994.

[104] S. Nakamura, M. Senoh, N. Iwasa, S.-i. Nagahama, T. Yamada, and T. Mukai, "Superbright green InGaN single-quantum-well-structure light-emitting diodes," *Japanese Journal of Applied Physics*, vol. 34, no. 10B, p. L1332, 1995.

[105] "Nichia Corporation." https://www.nichia.co.jp/en/about_nichia/history.html (accessed.

[106] S. Nakamura *et al.*, "InGaN-based multi-quantum-well-structure laser diodes," *Japanese Journal of Applied Physics,* vol. 35, no. 1B, p. L74, 1996.

[107] E. Feltin *et al.*, "Broadband blue superluminescent light-emitting diodes based on GaN," *Applied Physics Letters,* vol. 95, no. 8, p. 081107, 2009.

[108] T.-C. Lu, C.-C. Kao, H.-C. Kuo, G.-S. Huang, and S.-C. Wang, "CW lasing of current injection blue GaN-based vertical cavity surface emitting laser," *Applied Physics Letters,* vol. 92, no. 14, p. 141102, 2008.

[109] T. Someya, R. Werner, A. Forchel, M. Catalano, R. Cingolani, and Y. Arakawa, "Room temperature lasing at blue wavelengths in gallium nitride microcavities," *Science,* vol. 285, no. 5435, pp. 1905-1906, 1999.

[110] G. R. Goldberg *et al.*, "Gallium nitride light sources for optical coherence tomography," 2017, vol. 10104: International Society for Optics and Photonics, p. 101041X.

[111] D. Taillaert *et al.*, "Grating couplers for coupling between optical fibres and nanophotonic waveguides," *Japanese Journal of Applied Physics,* vol. 45, no. 8R, p. 6071, 2006.

[112] J. S. Penadés *et al.*, "Suspended SOI waveguide with sub-wavelength grating cladding for mid-infrared," *Optics letters,* vol. 39, no. 19, pp. 5661-5664, 2014.

[113] F. Van Laere *et al.*, "Compact and highly efficient grating couplers between optical fibre and nanophotonic waveguides," *Journal of lightwave technology,* vol. 25, no. 1, pp. 151-156, 2007.

[114] M. Tchernycheva *et al.*, "Integrated photonic platform based on InGaN/GaN nanowire emitters and detectors," *Nano letters,* vol. 14, no. 6, pp. 3515-3520, 2014.

[115] Y. Zhang *et al.*, "GaN directional couplers for integrated quantum photonics," *Applied Physics Letters,* vol. 99, no. 16, p. 161119, 2011.

[116] D. Bai *et al.*, "Suspended GaN-based nanostructure for integrated optics," *Applied Physics B,* vol. 122, no. 1, p. 9, 2016.

[117] Q. Liu, H. Wang, S. He, T. Sa, X. Cheng, and R. Xu, "Design of micro-nano grooves incorporated into suspended GaN membrane for active integrated optics," *AIP Advances,* vol. 8, no. 11, p. 115118, 2018.

[118] H. P. D. Schenk, E. Feltin, M. Laügt, O. Tottereau, P. Vennéguès, and E. Doghèche, "Realization of waveguiding epitaxial GaN layers on Si by low-pressure metalorganic vapor phase epitaxy," *Applied physics letters,* vol. 83, no. 25, pp. 5139-5141, 2003.

[119] H. Chen *et al.*, "Low loss GaN waveguides at the visible spectral wavelengths for integrated photonics applications," *Optics Express,* vol. 25, no. 25, pp. 31758-31773, 2017/12/11 2017, doi: 10.1364/OE.25.031758.

[120] R. Hui, Y. Wan, J. Li, S. Jin, J. Lin, and H. Jiang, "III-nitride-based planar lightwave circuits for long wavelength optical communications," *IEEE journal of quantum electronics,* vol. 41, no. 1, pp. 100-110, 2005.

[121] R. Hui *et al.*, "GaN-based waveguide devices for long-wavelength optical communications," *Applied physics letters*, vol. 82, no. 9, pp. 1326-1328, 2003.

[122] T. Sekiya, T. Sasaki, and K. Hane, "Design, fabrication, and optical characteristics of freestanding GaN waveguides on silicon substrate," *Journal of Vacuum Science & Technology B, Nanotechnology and Microelectronics: Materials, Processing, Measurement, and Phenomena*, vol. 33, no. 3, p. 031207, 2015.

[123] N. A. Hueting and M. J. Cryan, "Doubly resonant photonic crystal cavities in gallium nitride for fluorescence sensing," *Journal of the Optical Society of America B*, vol. 31, no. 12, pp. 3008-3017, 2014/12/01 2014, doi: 10.1364/JOSAB.31.003008.

[124] N. Vico Triviño *et al.*, "Gallium nitride L3 photonic crystal cavities with an average quality factor of 16 900 in the near infrared," *Applied Physics Letters*, vol. 105, no. 23, p. 231119, 2014.

[125] M. S. Mohamed *et al.*, "Efficient continuous-wave nonlinear frequency conversion in high-Q gallium nitride photonic crystal cavities on silicon," *APL Photonics*, vol. 2, no. 3, p. 031301, 2017.

[126] H. Zhao *et al.*, "Visible-to-near-infrared octave spanning supercontinuum generation in a silicon nitride waveguide," *Optics letters*, vol. 40, no. 10, pp. 2177-2180, 2015.

[127] S. Romero-García, F. Merget, F. Zhong, H. Finkelstein, and J. Witzens, "Silicon nitride CMOS-compatible platform for integrated photonics applications at visible wavelengths," *Optics express*, vol. 21, no. 12, pp. 14036-14046, 2013.

[128] D. Zecca *et al.*, "Label-Free $\hbox {Si} _ {3}\hbox {N} _ {4} $ Photonic Crystal Based Immunosensors for Diagnostic Applications," *IEEE Photonics Journal*, vol. 6, no. 6, pp. 1-7, 2014.

[129] K. Deasy *et al.*, "A chemical sensor based on a photonic-crystal L3 nanocavity defined in a silicon-nitride membrane," *Journal of Materials Chemistry C*, vol. 2, no. 41, pp. 8700-8706, 2014.

[130] C. Shen *et al.*, "Semipolar III–nitride quantum well waveguide photodetector integrated with laser diode for on-chip photonic system," *Applied Physics Express*, vol. 10, no. 4, p. 042201, 2017.

[131] M. Feng *et al.*, "On-chip integration of GaN-based laser, modulator, and photodetector grown on Si," *IEEE Journal of Selected Topics in Quantum Electronics*, vol. 24, no. 6, pp. 1-5, 2018.

[132] M. J. Deen and P. K. Basu, *Silicon photonics: fundamentals and devices*. John Wiley & Sons, 2012.

[133] G. T. Reed and A. P. Knights, *Silicon photonics: an introduction*. John Wiley & Sons, 2004.

[134] R. G. Hunsperger, *Integrated optics*. Springer, 1995.

[135] R. G. Hunsperger, A. Yariv, and A. Lee, "Parallel end-butt coupling for optical integrated circuits," *Applied optics*, vol. 16, no. 4, pp. 1026-1032, 1977.

[136] Z. Lu and D. W. Prather, "Total internal reflection–evanescent coupler for fibre-to-waveguide integration of planar optoelectric devices," *Optics letters*, vol. 29, no. 15, pp. 1748-1750, 2004.

[137] D. Taillaert, P. Bienstman, and R. Baets, "Compact efficient broadband grating coupler for silicon-on-insulator waveguides," *Optics letters*, vol. 29, no. 23, pp. 2749-2751, 2004.

[138] R. Marchetti *et al.*, "High-efficiency grating-couplers: demonstration of a new design strategy," *Scientific reports*, vol. 7, no. 1, pp. 1-8, 2017.

[139] P. S. J. Russell, "Optics of Floquet-Bloch waves in dielectric gratings," *Applied Physics B*, vol. 39, no. 4, pp. 231-246, 1986.

[140] K. R. Harper, "Theory, design, and fabrication of diffractive grating coupler for slab waveguide," 2003.

[141] J. H. Harris, R. K. Winn, and D. G. Dalgoutte, "Theory and design of periodic couplers," *Applied Optics*, vol. 11, no. 10, pp. 2234-2241, 1972.

[142] N. Bonod and J. Neauport, "Diffraction gratings: from principles to applications in high-intensity lasers," *Advances in Optics and Photonics*, vol. 8, no. 1, pp. 156-199, 2016.

[143] R. Larrea, A. M. Gutierrez, and P. Sanchis, "Design method for high performance grating couplers in photonic integrated circuits," *Optical and Quantum Electronics*, vol. 50, no. 9, p. 341, 2018.

[144] D. L. Lee, *Electromagnetic principles of integrated optics*. Wiley, 1986.

[145] J. M. Senior and M. Y. Jamro, *Optical fibre communications: principles and practice*. Pearson Education, 2009.

[146] B. S. Guru and H. R. Hiziroglu, *Electromagnetic field theory fundamentals*. Cambridge university press, 2009.

[147] J. D. Joannopoulos, S. G. Johnson, J. N. Winn, and R. D. Meade, *Photonic Crystals: Molding the Flow of Light - Second Edition*. Princeton University Press, 2011.

[148] A. S. Barker Jr and M. Ilegems, "Infrared lattice vibrations and free-electron dispersion in GaN," *Physical Review B,* vol. 7, no. 2, p. 743, 1973.

[149] I. H. Malitson, "Refraction and dispersion of synthetic sapphire," *JOSA,* vol. 52, no. 12, pp. 1377-1379, 1962.

[150] M. Gromovyi, F. Semond, J.-Y. Duboz, G. Feullet, and M. De Micheli, "Low loss GaN waveguides for visible light on Si substrates," 2014.

[151] S. Jia *et al.,* "Waveguide integrated GaN distributed Bragg reflector cavity using low-cost nanolithography," *Micro & Nano Letters,* vol. 14, no. 13, pp. 1322-1327, 2019.

[152] Q. Liu and W. Wang, "Free-standing GaN grating couplers and rib waveguide for planar photonics at telecommunication wavelength," *Optics & Laser Technology,* vol. 98, pp. 257-263, 2018.

[153] A. Stolz *et al.,* "Optical waveguide loss minimised into gallium nitride based structures grown by metal organic vapor phase epitaxy," *Applied Physics Letters,* vol. 98, no. 16, p. 161903, 2011.

[154] O. Westreich, M. Katz, Y. Paltiel, O. Ternyak, and N. Sicron, "Low propagation loss in GaN/AlGaN-based ridge waveguides," *physica status solidi (a),* vol. 212, no. 5, pp. 1043-1048, 2015.

[155] A. Othonos and K. Kalli, *Fibre Bragg Gratings: Fundamentals and Applications in Telecommunications and Sensing* (Artech House optoelectronics library). Artech House, 1999.

[156] D. G. Rabus, *Integrated ring resonators*. Springer, 2007.

[157] Z. Bor, K. Osvay, B. Racz, and G. Szabó, "Group refractive index measurement by Michelson interferometer," *Optics communications*, vol. 78, no. 2, pp. 109-112, 1990.

[158] Y. O. Barmenkov, D. Zalvidea, S. Torres-Peiró, J. L. Cruz, and M. V. Andrés, "Effective length of short Fabry-Perot cavity formed by uniform fibre Bragg gratings," *Optics Express*, vol. 14, no. 14, pp. 6394-6399, 2006.

[159] L. A. Coldren, S. W. Corzine, and M. L. Mashanovitch, *Diode lasers and photonic integrated circuits*. John Wiley & Sons, 2012.

[160] J. H. Harlow, *Electric power transformer engineering*. CRC press, 2003.

[161] M. H. Tooley, *Electronic Circuits: Fundamentals and Applications*. Elsevier, 2006.

[162] N. D. M. Zamani, M. N. Nawi, S. Shaari, B. Y. Majlis, and A. R. M. Zain, "Design and simulation of two-dimensional (2D) Gallium Nitride (GaN) photonic crystal on sapphire," in *2018 IEEE 7th International Conference on Photonics (ICP)*, 9-11 April 2018, pp. 1-3, doi: 10.1109/ICP.2018.8533165.

[163] F. Kehl, D. Bischof, M. Michler, M. Keka, and R. Stanley, "Design of a label-free, distributed Bragg grating resonator based dielectric waveguide biosensor," 2015, vol. 2: Multidisciplinary Digital Publishing Institute, 1 ed., pp. 124-138.

[164] N. A. Hueting *et al.*, "A Gallium Nitride Distributed Bragg Reflector cavity for integrated photonics applications," in *2012 14th International Conference on Transparent Optical Networks (ICTON)*, 2-5 July 2012, pp. 1-4, doi: 10.1109/ICTON.2012.6253827.

[165] T. T. Wu, H. W. Chen, Y. P. Lan, T. C. Lu, and S. C. Wang, "Suspended GaN-based band-edge type photonic crystal nanobeam cavities," *Optics express*, vol. 22, no. 3, pp. 2317-2323, 2014.

[166] N. D. M. Zamani, A. R. M. Zain, and B. Y. Majlis, "Modelling of 2-D Gallium Nitride (GaN) photonic crystal," in *2016 IEEE International Conference on Semiconductor Electronics (ICSE)*, 17-19 Aug 2016, pp. 54-56, doi: 10.1109/SMELEC.2016.7573589.

[167] N. Vico Triviño *et al.*, "High quality factor two dimensional GaN photonic crystal cavity membranes grown on silicon substrate," *Applied Physics Letters*, vol. 100, no. 7, p. 071103, 2012.

[168] K. Yee, "Numerical solution of initial boundary value problems involving Maxwell's equations in isotropic media," *IEEE Transactions on antennas and propagation*, vol. 14, no. 3, pp. 302-307, 1966.

[169] A. Taflove and S. C. Hagness, *Computational electrodynamics: the finite-difference time-domain method*. Artech house, 2005.

[170] *Lumerical FDTD Solutions*. (2017a).

[171] "FDTD solver - Simulation Object." https://support.lumerical.com/hc/en-us/articles/360034382534-FDTD-solver-Simulation-Object (accessed.

[172] "1-D mode solver for dielectric multilayer slab waveguides." https://www.computational-photonics.eu/oms.html (accessed.

[173] P. Dong and A. G. Kirk, "Second-order Bragg waveguide grating as a 1D photonic bandgap structure in SOI waveguide," 2004, vol. 5577: International Society for Optics and Photonics, pp. 589-597.

[174] A. J. Danner, "An introduction to the plane wave expansion method for calculating photonic crystal band diagrams," *University of Illinois,* 2002.

[175] J. Hu and C. R. Menyuk, "Understanding leaky modes: slab waveguide revisited," *Advances in Optics and Photonics,* vol. 1, no. 1, pp. 58-106, 2009.

[176] J. Čtyroký *et al.*, "Bragg waveguide grating as a 1D photonic band gap structure: COST 268 modelling task," *Optical and Quantum Electronics,* vol. 34, no. 5-6, pp. 455-470, 2002.

[177] H. H. Solak, C. Dais, and F. Clube, "Displacement Talbot lithography: a new method for high-resolution patterning of large areas," *Optics express,* vol. 19, no. 11, pp. 10686-10691, 2011.

[178] P. J. P. Chausse, E. D. Le Boulbar, S. D. Lis, and P. A. Shields, "Understanding resolution limit of displacement Talbot lithography," *Optics express,* vol. 27, no. 5, pp. 5918-5930, 2019.

[179] E. D. Le Boulbar, P. J. P. Chausse, S. Lis, and P. A. Shields, "Displacement Talbot lithography: an alternative technique to fabricate nanostructured metamaterials," in *Conference on Nanotechnology VIII*, Barcelona, SPAIN, May 08-09 2017, vol. 10248,

BELLINGHAM: Spie-Int Soc Optical Engineering, in Proceedings of SPIE, 2017, doi: 10.1117/12.2211588. [Online]. Available: <Go to ISI>://WOS:000406961800014

[180] P. Shields *et al.*, "Fabrication and properties of etched GaN nanorods," *physica status solidi c*, vol. 9, no. 3-4, pp. 631-634, 2012.

[181] D. Dai, Y. Tang, and J. E. Bowers, "Mode conversion in tapered submicron silicon ridge optical waveguides," *Optics express*, vol. 20, no. 12, pp. 13425-13439, 2012.

[182] J. Pastrňák and L. Roskovcová, "Refraction index measurements on AlN single crystals," *physica status solidi (b)*, vol. 14, no. 1, pp. K5-K8, 1966.